

Novel Rheology-Based Therapies for the Potential Treatment of Sickle Cell Disease

by

Daniel Joseph Crompton

B.S. Bioengineering, Pennsylvania State University, 2014

Submitted to the Graduate Faculty of the
Swanson School of Engineering in partial fulfillment
of the requirements for the degree of
Doctor of Philosophy

University of Pittsburgh

2020

UNIVERSITY OF PITTSBURGH

SWANSON SCHOOL OF ENGINEERING

This dissertation was presented

by

Daniel Joseph Crompton

It was defended on

October 14, 2020

and approved by

Prithu Sundd, PhD

Assistant Professor, Departments of Medicine and Bioengineering

Jonathan P. Vande Geest, PhD

Professor, Department of Bioengineering

Jonathan H. Waters, MD

Professor, Anesthesiology and Perioperative Medicine and Bioengineering

Chief of Anesthesiology, UPMC Magee-Women's Hospital

Dissertation Director: Marina V. Kameneva, PhD

Research Professor, Departments of Surgery and Bioengineering

Copyright © by Daniel Joseph Crompton

2020

Novel Rheology-Based Therapies for the Potential Treatment for Sickle Cell Disease

Daniel Joseph Crompton, PhD

University of Pittsburgh, 2020

Sickle Cell Disease (SCD) is a group of inherited hemoglobinopathies affecting over 100,000 individuals in the United States and millions more worldwide. Sickle cell anemia, the most common and severe type of SCD, is the result of a point mutation which allows intraerythrocytic hemoglobin to polymerize with itself under oxygen-poor conditions, forming long crystalline or polymeric chains within red blood cells (RBCs) and causing these cells to become sickle-shaped and prone to hemolysis. Due to their decreased deformability and higher affinity to adhere to the endothelium and other blood cells, sickled RBCs occlude the microvasculature, resulting in flow obstruction, tissue hypoxia and ischemia, and an inflammatory response. These effects lead to sudden, severe pain due to systemic vaso-occlusive episodes (VOE) which requires acute care and extended hospitalization.

Although multiple pharmacologic therapies are currently approved by the FDA for the treatment of SCD, there exists a lack of adequate treatment options for the prevention of vaso-occlusion and related SCD comorbidities. The overarching purpose of this work is to develop and test two novel rheological-based approaches as potential options for the treatment of SCD. First, the use of blood soluble additives known as drag-reducing polymers (DRPs) were examined for their potential to improve blood flow within microvessels and reduce vaso-occlusion. Our in vitro findings suggest that DRPs may improve the circulation of less-deformable RBCs such as sickle

RBCs by reducing their near wall margination and altering their traffic patterns through microchannel bifurcations. Transgenic SCD mice administered DRPs were also found to have significantly reduced hepatic vaso-occlusion during intravital imaging following an inflammatory stimulus. The second rheological-based approach for the treatment of SCD explored a method of intracellular hemoglobin replacement, where we show proof-of-concept feasibility of a technique to remove sickle hemoglobin from sickle RBCs and subsequently replace their intracellular contents with healthy donor hemoglobin. ‘Refilled’ SCD RBCs showed an inability to sickle and improved rheological characteristics, demonstrating this process as a potential novel transfusion therapy in order to eliminate the risk of alloimmunization in SCD patients.

Table of Contents

Preface.....	xix
Nomenclature	xxi
1.0 Introduction.....	1
1.1 Hemorheology	1
1.1.1 Blood Components	1
1.1.2 Blood Flow in the Microcirculation.....	2
1.1.3 Quantifying the Hemorheological Parameters of Blood	5
1.2 Sickle Cell Disease	8
1.2.1 Background.....	8
1.2.2 SCD Pathophysiology and Altered Hemorheology	11
1.2.3 Current Treatment Paradigms	13
1.3 Drag-Reducing Polymers.....	14
1.3.1 Background.....	14
1.3.2 Effects of DRPs <i>in vitro</i> and <i>in vivo</i>	15
1.3.3 Degradation of DRPs and Considerations for Clinical Use	20
1.4 Objectives	21
1.4.1 Study the Effects of DRP on Cellular Traffic <i>in vitro</i> Within Bifurcating Microchannel Models	22
1.4.2 Determine the Influence of DRP <i>in vivo</i> on Vaso-Occlusion and Neutrophil Aggregation in Transgenic SCD Mice.....	23

1.4.3 Perform Feasibility Testing for Intracellular Hemoglobin Replacement as a Novel Form of SCD Transfusion Therapy.....	24
2.0 The Effects of DRP on Cellular Traffic <i>in vitro</i> Within Bifurcating Microchannels	
.....	25
2.1 Introduction	26
2.2 Materials and Methods	28
2.2.1 Sample Preparation	28
2.2.2 Experimental Setup.....	29
2.2.3 Determination of RBC Deformability Via Ellipsometry	32
2.2.4 Image Processing.....	34
2.2.5 Data Analysis	37
2.2.6 Statistical Analysis	38
2.3 Results.....	38
2.3.1 Microchannel Parameter Calculation.....	38
2.3.2 Microchannel Validation / Verification of the Plasma Skimming Effect	39
2.3.3 Hemorheological Characterization of the Less-Deformable Blood Mixture	42
2.3.4 Distribution of Less-Deformable RBC Traffic Through Daughter Branch Outlets	44
2.4 Discussion	45
2.4.1 Study Limitations	48
2.5 Conclusions	48
3.0 The Influence of DRP <i>in vivo</i> on Vaso-Occlusion and Neutrophil Aggregation in Transgenic SCD Mice.....	49

3.1 Introduction	49
3.2 Materials and Methods	50
3.2.1 Reagents and DRP Preparation.....	50
3.2.2 Mice	51
3.2.3 Surgical Preparation and qLIM Imaging.....	51
3.2.4 Image Analysis.....	53
3.2.5 Statistical Analysis	54
3.3 Results.....	54
3.3.1 Experiments Performed on Mice Homozygous for SCD.....	54
3.3.2 Experiments Performed on SCD Trait (SA) Mice	62
3.4 Discussion	65
3.5 Conclusions	66
4.0 Development of an Intracellular Hemoglobin Replacement Therapy for the Potential Treatment of SCD and Rheological Characterization of Modified RBCs	67
4.1 Introduction	67
4.2 Materials and Methods	68
4.2.1 Hb Solution Preparation	68
4.2.2 Intracellular Hb Exchange Protocol	69
4.2.3 Rheological Analysis of Modified RBCs	70
4.2.4 Statistical Analysis	72
4.3 Results.....	72
4.3.1 Modified RBC Hemoglobin Content and Morphology	72
4.3.2 Cell Deformability.....	76

4.3.3 Viscoelasticity	77
4.4 Discussion	84
4.5 Conclusions	88
5.0 Summary.....	90
5.1 Conclusions	90
5.2 Future Studies.....	92
5.2.1 Determine the Effects of DRP on Changes in Rigid Particle Traffic Through Branched Microchannels.....	92
5.2.2 Attenuation of Neutrophil-Platelet Interactions with DRP.....	93
5.2.3 Expanded Intravital Imaging Work in Transgenic SCD Mice.....	93
5.2.4 Intracellular Hb Replacement Future Studies	94
Appendix A Drag-reducing Polymers Improve Oxygen Transfer Rate in Miniature Hollow Fiber Membrane Oxygenators	96
Appendix A.1 Introduction.....	96
Appendix A.2 Materials and Methods.....	98
Appendix A.2.1 Miniature HFMO Experiments with DRP.....	98
Appendix A.3 Results	101
Appendix A.3.1 Miniature HFMO Experiments with DRP.....	101
Appendix A.4 Discussion.....	103
Appendix A.5 Conclusions.....	105
Appendix B Supplementary Methods	106
Appendix B.1 Logistic Regression Algorithm.....	106
Appendix B.2 Viscoelastometry Methods.....	109

Appendix C Programming Code and Scripts.....	112
Appendix C.1 ImageJ Macro for Initial Image Processing and Particle Identification	112
Appendix C.2 Automation of ImageJ Macro Within MATLAB	113
Appendix C.3 Logistic Regression Algorithm.....	116
Appendix C.4 LogisticRegression.m MATLAB Function File.....	118
Appendix C.5 costFunction.m MATLAB Function File	124
Bibliography	125

List of Tables

Table 1. Summary of Re in different areas of the circulation^{3,5,6}	3
Table 2. Summary of selected DRP studies, by year published.....	16

List of Figures

Figure 1. RBC sickling via HbS polymerization. As oxygenated RBCs (bright red) pass through the microcirculation, they deoxygenate (purple) revealing hydrophobic patches on the hemoglobin β subunit. The interaction and binding of multiple deoxygenated HbS units produces intracellular HbS fibers which may align and distort the RBC into the classic “sickle” shape. Reproduced with permission from Bunn⁴⁹, Copyright Massachusetts Medical Society.	10
Figure 2. Diagram depicting the vicious cycle of poor blood rheology leading to microcirculatory stasis during sickle cell vaso-occlusive episodes. Figure adapted from Chein el al.⁵⁷ with permission.	13
Figure 3. Schematic of recirculation zones following blood vessel bifurcations before (left), and after the administration of DRP (right). Figure reused from Kameneva⁹⁶ with permission.....	17
Figure 4. DRPs eliminate the CFL and reduce the plasma skimming effect within microvessels by increasing daughter branch outlet hematocrit (Ht).	19
Figure 5. The chemical structure of PEO.	20
Figure 6. Schematic of custom PDMS microchannels. Main channel dimensions: 200μm (width) x 50μm (height), Daughter branch dimensions: 100μm (width) x 50 μm (height). The main channel total length is 1.2 cm, and the daughter branch channel length is 0.4 cm. Note: schematic pictured is not to scale.	30
Figure 7. Experimental microchannel setup schematic.	32

Figure 8. Linkam CSS450 parallel-plate shearing stage schematic (top) and parallel disk geometry (bottom). Aperture diameter (A, 2.5 mm), Disk diameter (D, 30 mm), Radius from center to aperture (R, 7.5 mm), and gap height (variable, set at 50 μm). Figure adapted with permission from Hellmuth¹⁰⁹..... 33

Figure 9. Representative images of healthy (Top), less-deformable (Middle), and mix of healthy and less-deformable (Bottom) RBCs captured using the Linkam device at 52 Pa of shear stress (1000s⁻¹). For each image, top-left cut-outs show original images, with the bottom-right cut-out showing results after image processing and measurement. Note overlapping RBCs, cellular debris and unevenillumination areas are not falsley counted as measured RBCs (cyan outline)..... 36

Figure 10. The measured pressured drop across the microchannle experiences a significant increase with the addition of nanomolar concentrations of DRP, theorized to be due to the reduction in the near-wall CFL and increase in the near-wall viscosity. n = 5, p < 0.01. 39

Figure 11. The plasma skimming effect, showing a decreased Ht in the daughter outlet as compared to the main (n = 5, p = 0.017) (Top). Non-significant Ht changes between main and daughter outlets with the addition of DRP, indicating the elimination of both the CFL and the plasma skimming effect (n = 7, p > 0.05) (Bottom). 41

Figure 12. RBC rigidification protocol was found to be best using a 52°C water bath for 30 minutes for bovine blood. Measured plasma-free hemoglobin (ΔpfHb) was measured in mg/dL. Data points not showing ΔpfHb values were negligible. 43

Figure 13. Viscosity measurements collected with the Vilastic-3 showing elevated viscosity of bovine RBCs following heat treatment (rigid) and compared to healthy and sickle RBCs (SRBCs). All samples were measured at 30% Ht and at room temperautre. SCD blood

viscosity measurements for comparison were collected from work performed in Chapter 4. Error bars represent mean \pm SE. 44

Figure 14. The percent differences of healthy RBCs between branch and main outlets. In control groups, an average of $-8.5 \pm 2.5\%$ fewer healthy RBCs exited the branch outlet than less-deformable RBCs. In groups with 10 ppm DRP, an average of $+12.1 \pm 5.4\%$ more healthy RBCs exited the branch outlet than less-deformable RBCs ($n = 6, p = 0.02$)...... 45

Figure 15. Schematic diagram of experimental process and qLIM imaging setup. Figure adapted with permission from Pradhan-Sundd et al¹²²..... 52

Figure 16. Flowchart of the image processing performed..... 54

Figure 17. All vessels identified following the intravital qLIM imaging process. Representative still frame of SCD mouse liver receiving LPS (Top) and experimental animal still frame of SCD mouse liver receiving both LPS and DRP (Bottom). (TXR)-dextran and Ly6G green were used to stain the blood plasma and neutrophils respectively. RBCs can be discerned as dark shapes within the vessels and were not stained. Yellow outlines denote areas identified as vessels, with 20 μ m scale bars..... 56

Figure 18. Segmentation of only flowing vessels identified following the intravital qLIM imaging process. Representative still frame of SCD mouse liver receiving LPS (Left) and experimental animal still frame of SCD mouse liver receiving both LPS and DRP (Right). (TXR)-dextran and Ly6G green were used to stain the blood plasma and neutrophils respectively. RBCs can be discerned as dark shapes within the vessels and were not stained. Yellow outlines denote areas identified as flowing vessels, with 20 μ m scale bars. 58

Figure 19. Quantification of the percentage of total flowing vessel area per FOV. Data presented as mean \pm SE, where * denotes $p < 0.001$ 59**

Figure 20. Quantification of the percentage of total flowing vessels per FOV by their individual count. Data presented as mean \pm SE, where * denotes $p < 0.001$ 60**

Figure 21. Still image from a SCD mouse receiving LPS showing a large neutrophil containing vaso-occlusion region in inset. Inset depicts occluded liver sinusoid with multiple neutrophils surrounded by RBCs within the luminal space. (TXR)-dextran and Ly6G green were used to stain the blood plasma and neutrophils respectively. 61

Figure 22. Number of neutrophil-containing vaso-occlusion per FOV in SCD mice. Data presented as mean \pm SE, where * denotes $p < 0.001$ 62**

Figure 23. Representative SCD trait (SA) image, with all flowing vessels identified in yellow. Regions of vaso-occlusion are marked with *. (TXR)-Dextran and Ly6G green were used to stain the blood plasma and neutrophils, respectively. RBCs can be discerned as dark shapes within vessels and were not stained. Note region in bottom left of image still which was not analyzed due to out of focus vessels boundaries. Yellow outlines denote areas identified as vessels, with 20 scale bars. 63

Figure 24. Sickle Cell trait (SA) mice receiving the same volume of LPS did not exhibit the same degree of vaso-occlusion as mice homogeneous for SCD. Quantification of percentage of flowing vessels by total area (top), and quantification of the percentage of total flowing vessels per FOV by their individual count (bottom). Data presented as mean \pm SE, where * indicates $p < 0.001$. A total of 21 FOVs of the SA (trait) mice given LPS were collected and analyzed, with a subject count of $n = 2$ 64**

Figure 25. Schematic of the experimental protocol for intracellular Hb replacement. 70

Figure 26. Custom mini hollow fiber membrane oxygenator made with polymethylpentene fibers..... 71

Figure 27. Mean corpuscular Hb concentration (MCHC) [g/dL] of refilled and ghost sickle RBC samples alongside healthy refilled and ghost RBCs created using identical protocols for comparison. 73

Figure 28. Sicklescreen testing results. In the presence of HbS, solutions become turbid and reading rack lines will no longer be visible. Positive Sicklescreen control samples and unmodified sickle RBCs were determined to contain HbS. Both ghost and refilled RBC samples derived from SCD blood were found to no longer contain appreciable HbS following Hb replacement therapy..... 74

Figure 29. (A) Oxygenated unmodified sickle RBCs, (B) Deoxygenated unmodified sickle RBCs, (C) Oxygenated refilled sickle RBCs, (D) Deoxygenated refilled sickle RBCs, (E) Oxygenated ghost sickle RBCs. 75

Figure 30. EI of sickle RBCs undergoing intracellular Hb exchange therapy in comparison to healthy human RBCs. Healthy human RBCs (n = 3) were found to have a significantly greater EI than unmodified sickle RBCs (n = 6, p = 0.018), ghost sickle RBCs (n = 6, p = 0.004), and refilled sickle RBCs (n = 5, p < .001). Both refilled and ghost sickle RBCs were not found to have a significantly greater ability to deform than unmodified sickle RBCs following intracellular Hb exchange (p > 0.05). Data represents mean ± SD, scale bar represents 10 μm and applies to all inset images. 77

Figure 31. Viscosity (Top) and elasticity (Bottom) of purified bovine hemoglobin at various concentrations. Data presented represents mean ± SD. Middle figure legend represents both Top and Bottom graphs..... 79

Figure 32. Viscosity (Top) and elasticity (Bottom) of purified and concentrated SCD HbS solution in deoxygenated and oxygenated state. Bovine Hb viscoelasticity also included for comparison. Data presented represents mean \pm SD. 80

Figure 33. Viscosity (Top) and elasticity (Bottom) of SCD blood samples undergoing intracellular Hb exchange therapy. Middle figure legend represents both Top and Bottom graphs. Data shown as mean \pm SD. 83

Figure 34. Statistical analysis of viscosity differences at low (26s^{-1}) and high (210 s^{-1}) shear rates. * represents significant statistical difference from SCD RBC samples ($p < 0.05$), and # represents significant statistical difference from healthy human blood samples ($p < 0.05$). Data shown as mean \pm SD. 84

Figure 35. Thrombus formation found within ECMO artificial lung device requiring device exchange. Image used with permission from Parlar et al ¹⁵³. 97

Figure 36. Experimental setup used for the deoxygenation and oxygenation of both blood and Hb solutions using our custom made miniature HFMO device. 99

Figure 37. Oxygen exchange rate across the miniature HFMO with bovine blood. Results represent mean \pm SD. 101

Figure 38. Oxygen exchange rate across the miniature HFMO with bovine Hb solution. Results represent mean \pm SD. 102

Figure 39. Schematic of proposed possible mechanism for improved gas transfer performance of HFMOs with DRPs. Following the introduction of DRPS within the HFMO device, recirculation and stagnant zones are eliminated or diminished, allowing for improved blood mixing and movement of RBCs closer to fiber membranes. 104

Figure 40. Flowchart of logistic regression algorithm. Healthy and less-deformable RBC length and width measurements are collected and plotted separately, with each point representing the measurements of a single RBC. A decision boundary gate is then created using a logistic regression algorithm, classifying points above the boundary as ‘healthy’ and below the boundary as ‘less-deformable. Following validation, the percentage of healthy or less-deformable heat treated RBCs can be identified from sample mixtures containing unknown percentages of each. 108

Figure 41. Schematic of the Vilastic-3 viscoelastometer principle of measurement..... 111

Preface

First and foremost, thank you to Dr. Marina Kameneva for welcoming me into her lab, taking a chance on a new grad student, and teaching me how to become a researcher and think like a scientist. Like a carrot on the end of a stick, your frequent gifts of chocolate bites always helped to push me towards my goal. Of course, thank you to my dissertation committee Dr. Prithu Sundd, Dr. Jonathan Vande Geest, and Dr. Jonathan Waters for their invaluable input and assistance in shaping the culmination of my work into what it has become today. However, the completion of this dissertation would never have been possible without the help of many others that I have worked with along my PhD journey.

I couldn't have asked for better lab-mates than the ones I found in Pitt. Thank you to Salim Olia and Luke Ziegler for showing me the ropes in lab when I first started, and to all those I had the great opportunity to work with especially Kat Zougari, Shushma Gudla, Shiv Rajesh, and David Chan, I value both our friendships and the countless hours spent together in lab. The opportunity to work part-time at UPMC's Artificial Heart Program was also an incredible and eye-opening clinical experience. Working at the program only solidified my reasoning as to why I chose the field of bioengineering - to help others. I will forever cherish my time spent with patients and family members, and the friends and colleagues I met along the way.

I must also acknowledge the generous funding sources that made my work possible in the first place. Over the course of my work I received grants from The Berenfield Graduate Fellowship Program, University of Pittsburgh's Center for Medical Innovation (CMI), The Commonwealth of Pennsylvania, McGowan Institute for Regenerative Medicine, The Department of Defense through

a collaboration with New Mexico University, and The Swanson School of Engineering's Cardiovascular Bioengineering Training Program (CBTP).

Finally, thank you to my friends and family, especially my parents Mary and Ed for always believing in me and encouraging me to do great things even if it entailed moving across the country or going back to school. Thank you to my brothers Greg and Phil for always having my back, supporting me, and helping to take my mind off of lab. Many, many thanks to my wonderful fiancée Alison for always being there for me regardless of distance and for being the best listener anyone could ask for. I love you and cannot wait to find what our future together holds.

Nomenclature

The following abbreviations are used throughout the document:

ACS	Acute Chest Syndrome
ARF	Acute Respiratory Failure
CFL	Cell-free Layer
cP	Centipoise [mPa*s]
CPDA-1	Citrate phosphate dextrose-adenine 1 (anticoagulant)
Da	Dalton
DRP	Drag-Reducing Polymer
EI	Elongation Index [unitless]
ECMO	Extracorporeal Membrane Oxygenation
FDA	Food and Drug Administration
FOV	Field of View
Hb	Hemoglobin
HbA	Adult Hemoglobin, also referred to as Hb
HbF	Fetal Hemoglobin
HbS	Sickle Hemoglobin
HFMO	Hollow Fiber Membrane Oxygenator
Ht	Hematocrit [%]
Hz	Hertz [s^{-1}]

I/RI	Ischemia/Reperfusion Injury
ISC	Irreversibly Sickled Cell
K ₂ EDTA	K ₂ Ethylenediaminetetraacetic acid (anticoagulant)
LPS	Lipopolysaccharide
mAb	Monoclonal antibody
MCHC	Mean corpuscular Hb concentration [g/dL]
mmHg	Millimeters of mercury
MPE	Multi-photon excitation
MW	Molecular Weight [Da]
n	Sample Size (statistics)
p	p-value (statistics)
Pa	Pascal, unit [$\text{kg}\cdot\text{m}^{-1}\cdot\text{s}^{-2}$]
PAA	Polyacrylamide
PBS	Phosphate Buffer Solution (w/o Ca^{2+} or Mg^{2+})
PDMS	Polydimethylsiloxane
PEG	Poly(ethylene glycol)
PEO	Poly(ethylene oxide)
PLLA	Poly-L-lactide
PMNN	Poly(mannan)
PVP	Polyvinylpyrrolidone
qLIM	Quantitative Liver Intravital Microscopy
qMFM	Quantitative Microfluidic Fluorescence Microscopy

RBC	Red Blood Cell
Re	Reynolds Number [dimensionless]
SCD	Sickle Cell Disease
SCD (AS)	Heterozygous SCD trait
SCD (Sβ°)	Sickle-β°-Thalassemia
SCD (Sβ ⁺)	Sickle-β ⁺ -Thalassemia
SCD (SC)	Sickle-Hemoglobin C Disease
SCD (SS)	Homozygous SCD
spO ₂	Oxygen Saturation Percentage [%]
S-RBC	Sickle Red Blood Cell
tHb	Total Hemoglobin [g/dL]
TXR	Texas-Red Dextran
μm	micron
WBC	White Blood Cell
VOE	Vaso-occlusive episode, also sometimes known as Vaso-occlusive Crisis (VOC)

1.0 Introduction

1.1 Hemorheology

1.1.1 Blood Components

The preservation of blood flow is essential for the delivery of oxygen and nutrients to all tissues of the body. In addition to oxygen delivery, blood is also responsible for the clearance of carbon dioxide and other metabolic wastes from these same tissues. Human blood is a two-phase suspension of cells in an aqueous solution, comprised of approximately 45% cells by volume in males and 40% in females¹. These cellular components include the deformable red blood cells (Erythrocytes or RBCs) responsible for oxygen transport, white blood cells (Leukocytes or WBCs) responsible for the immune response, and platelets (Thrombocytes) responsible for coagulation and hemostasis. Blood cells are suspended in an aqueous protein-rich solution known as plasma which contains among many other components, dissolved proteins (albumins (4.5 g/dL), globulins (2.5 g/dL), fibrinogen (0.3 g/dL), and other proteins (< 0.5 g/dL)), electrolytes, clotting factors, hormones, and other signaling molecules².

Mature RBCs are by far the most populous cell type in blood, comprising 99% of the total cellular volume and 4 – 6 million cells per microliter of blood. RBCs take the shape of a biconcave disk in their unstressed state with an average diameter of 8 μm and height of 1 – 3 μm^2 . Non-nucleated and containing 32 – 34 g/dL of concentrated hemoglobin proteins, RBCs are chiefly responsible for gas exchange, carrying oxygen from the lungs to distal tissues and returning back to the lungs with carbon dioxide from these same tissues for removal. The fraction by volume of

RBCs in blood is measured as hematocrit (Ht), and due to RBCs' dominance among other cellular components, Ht is the main determinant of blood's mechanical properties. WBCs occupy roughly 1% of blood by volume, with 4 – 11 thousand cells per microliter of blood. These nucleated cells are generally spherical in shape, 7 – 22 microns in diameter, and broadly responsible for immune system host defense and initiators of inflammation². Platelets number 250 – 500 thousand per microliter of blood, are roughly discoid with a diameter of 3 μm , and may become activated through cellular or cytokine signaling factors to initiate the coagulation cascade².

Together, this suspension of blood cells in plasma form a unique fluid connective tissue vital for life. Hemorheology, the study of blood flow, aims to understand how blood moves within the body, focusing on both normal blood flow and how different pathologies may be prevented which cause the disruption or cessation of flow.

1.1.2 Blood Flow in the Microcirculation

The collection of blood vessels referred to as the microcirculation is comprised of vast networks of vessels roughly 300 μm or less in diameter. In the direction of blood flow moving away from the heart, these vessels include the small arteries, arterioles (10 – 100 μm), and capillaries (3 – 7 μm). Blood then moves back to the heart via the venules (10 – 250+ μm) and veins³. Within these vessels, the majority of gas exchange and mass transport occurs for the oxygenation and nourishment of every tissue. Almost 80% of the difference in pressure drop from the aorta to the vena cava is due to the microcirculation³, and as the total vessel cross-sectional area increases exponentially in progressively smaller branches of the microcirculation, blood flow velocity also drastically decreases. The result is a marked difference between the pulsatile,

inertially driven flow of the systemic arteries towards a steady, viscous driven flow regime observed within the microcirculation.

The difference in flow properties between the systemic arterial circulation and the microcirculation can be quantitatively compared using the dimensionless Reynolds (Re) number, which measures the relation of inertial driven flow to viscous driven flow. The Reynolds number is expressed as:

$$Re = \rho VR/\mu \qquad \text{Equation 1.1}$$

where R is the characteristic radius of the vessel, ρ is the fluid density, μ is the fluid viscosity, and V is the characteristic fluid velocity⁴. A summary of these values in different regions of the circulatory system may be found in Table 1.

Table 1. Summary of Re in different areas of the circulation^{3,5,6}

	Aorta	Systemic Arteries	Arterioles	Capillaries	Venules	Veins	Vena Cava	
Re	$\frac{\text{inertial flow}}{\text{viscous flow}}$	2500 – 4000	100 – 1000	0.03 – 0.2	0.001	0.001 – 0.5	100 – 1700	700

Blood flow in the systemic arteries is regularly modeled as an incompressible, homogeneous, and non-Newtonian fluid continuum, as the geometry and flow rates are often much larger than individual cellular components and flow is dominated by fluid inertial effects ($Re \gg 1$). However, when studying physiologic flow within the microcirculation, it is no longer possible to treat blood as a homogeneous fluid, and it must be treated as a true two-phase suspension of

cells in plasma^{7,8}. This difference is due in part to the significantly smaller vessel size, in which RBCs may occupy a much larger percentage of the vessel or even be required to greatly deform in order to pass through vessels. Further, the suspended cellular particles within the vessel are neither homogeneously distributed through the cross section of the vessel nor do they stream in even proportions or at even rates through the many branched vessels of the microcirculation.

A great deal of what is known about hemorheology within the microcirculatory system was pioneered by the Swedish pathologist Robin Fåhræus, who famously observed that in tubes of less than 300 μm diameter, the tube discharge Ht is lower than that of the feed Ht, a phenomenon now known as the Fåhræus Effect⁹. This effect is due to RBC clustering in the axial core of vessels, where the mean velocity is greater than the bulk velocity of the blood¹⁰. Additionally, Fåhræus demonstrated that the apparent viscosity of blood decreases with decreasing tube diameter until an inflection point is reached at approximately 10 μm diameter, wherein the viscosity begins to dramatically increase again. This is known as the Fåhræus-Lindqvist Effect and is proposed to be a result of the formation of the peripheral cell-depleted layer, also known as the ‘cell-free’ layer (CFL)^{10,11}. This layer of lower viscosity plasma near the vessel wall results in the lowering of flow resistance and therefore the apparent viscosity.

In the microcirculation, the formation of the CFL is a natural phenomenon which occurs as a result of the drift of RBCs towards the center core of vessels¹². Through a process known as radial migration, deformable RBCs in blood vessels of diameters less than 300 μm naturally move towards the center of vessels creating an RBC-rich core, leaving a plasma CFL at the vessel periphery¹³. This action is primarily due to the deformable nature of RBCs, and is mechanistically caused by the aggregation of RBCs as well as hydrodynamic lift forces produced by wall effects acting on deformed RBCs in flow¹⁴⁻¹⁶. The thickness of the CFL may vary between 1 – 10 μm and

is dependent on vessel diameter, blood Ht, flow velocity, RBC aggregation, RBC deformability, and fibrinogen concentration¹². The presence of the CFL also results in the plasma skimming effect, where a larger proportion of plasma enters the smaller vessels at bifurcations, thereby reducing the Ht of the microcirculation to 20 – 50% that of the larger supplying vessels^{17,18}. Although the name suggests this outermost plasma layer is completely devoid of cellular components, the CFL contains a disproportionately high percentage of less deformable cells that may be found in blood such as platelets^{19,20}, leukocytes²¹, and less deformable RBCs or even rigid particles (if present)^{22,23}. The margination of these cells increases their likelihood of being ‘skimmed’ into smaller vessels at bifurcations, which increases their concentration within the microvasculature and may increase their tendency to obstruct flow due to their poor deformability or size^{24,25}.

1.1.3 Quantifying the Hemorheological Parameters of Blood

The viscoelasticity of a fluid is a material property which refers to its ability to both resist flow (viscosity) as well as absorb energy during flow (elasticity). All real fluids have some degree of viscosity due to frictional energy dissipation, but only certain fluids have elastic energy storing capabilities. Viscoelasticity (η^*) may be mathematically represented as a complex number:

$$\eta^* = \eta' - i\eta'' \quad \text{Equation 1.2}$$

where η' and η'' are the viscous and elastic components, respectively. The suspension of blood is an example of a fluid possessing both viscous and elastic properties, wherein the RBC membrane both resists deformation and stretches elastically as it flows²⁶. Further adding to its complexity, blood is a shear-thinning non-Newtonian fluid such that the measured apparent viscosity decreases

as the shear rate is increased. This is due to the dispersal of naturally occurring cellular aggregates with increasing shear rate and is also attributed to RBC elasticity and deformability²⁷. Only at elevated shear rates are RBCs both fully disaggregated and deformed, and viscosity measurements converge to a single asymptotic value (shear rate $> \sim 200 \text{ s}^{-1}$)^{27,28}.

Many methods of determining the mechanical and rheological properties of RBCs have been developed both clinically and experimentally. Each technique gives valuable insight into the rheological properties of blood suspensions or even individual RBCs, but each has its own inherent limitations. Depending on the study objective, one or several of these tests may be ideally suited to determining the desired characteristics of RBCs in a given sample. Direct viscoelastic measurement of blood suspensions is the most straightforward technique to measure the rheological properties of blood. This is usually performed using specialized instruments with specific geometries and flow paths such that known solutions to flow equations such as either pure Couette (cone/plate, parallel plate) or Poiseuille (pipe) flow can be leveraged to calculate material properties. In this work the viscosity and elasticity of samples were determined using the Vilastic-3 viscoelastometer (Vilastic Inc., Austin, TX), which measures oscillatory Poiseuille flow in a straight cylindrical tube. When measured under oscillatory flow, the mean velocity gradient (\bar{G}) in a tube of circular cross-section is given by:

$$\bar{G} = 8U / 3\pi a^3 \quad \text{Equation 1.3}$$

where U is the volume velocity of flow through the tube of radius a. Measurement of the pressure phases generated by the volume velocity in phase (p') and 90° out of phase (p'') may then be used to solve for the viscous (τ') and elastic components (τ'') of shear stress respectively:

$$\tau' = p'a / 3 \quad \text{Equation 1.4}$$

$$\tau'' = (4\rho\omega/3\pi a^2 - p'')Ua/3 \quad \text{Equation 1.5}$$

where ρ is the fluid density, and ω is the angular frequency of oscillation^{27,29}. The viscosity (η') and elasticity (η'') may then be calculated from these terms using the generic formulas:

$$\eta' = \tau'/\bar{G} \quad , \quad \eta'' = \tau''/\bar{G} \quad \text{Equation 1.6}$$

Further description of the measurement techniques and protocols used with the Vilastic-3 viscoelastometer may be found in Appendix A.3.

Direct measurement of blood viscoelasticity is useful in the determination of bulk properties, but is limited in its ability to determine how individual red cells behave within the microcirculation. Because these tests require relatively larger amounts of sample volume compared to other methods, they may not be feasible in areas with reduced sample availability, such as in small animal or pediatric testing.

Techniques used to quantify RBC deformability may be used in conjunction with viscoelastic tests to better characterize the specific mechanical properties of the cell membrane. The deformability of cells may be measured by their dimensions while subject to shear stress, which in the case of this work, were imaged using a Linkam Scientific Instruments rotating shearing microscope stage. Using this methodology, deformity is quantified using a dimensionless index called the Elongation Index (EI):

$$EI = |(length - width)/(length + width)| \quad \text{Equation 1.7}$$

There is no consensus for a single method of determining cell or RBC deformability. Other experimental models such as micropipette aspiration are useful in collecting information regarding the membrane shear modulus³⁰, while techniques such as laser diffraction ektacytometry (a form of ellipsometry) can be used to determine cellular osmotic fragility simultaneously with cellular deformability under rotational shear stress^{31,32}. Many other techniques for the quantification of RBC rheology and deformability have been described previously in other works³³. The filterability of blood through porous membranes^{34,35}, atomic force microscopy³⁶, and the passage of blood through microfluidic devices^{37,38} have also been used to quantify the deformability of the red cell membrane and its ability to pass through small channels. Now seldom-used clinical methods such as plasma viscosity³⁹, and RBC aggregation and sedimentation rate⁴⁰ have been replaced with modern technologies such as automated optical aggregometers.

1.2 Sickle Cell Disease

1.2.1 Background

Hemoglobinopathies are some of the most widely inherited diseases worldwide, with Sickle Cell Disease (SCD) being among the most common⁴¹. An estimated 7% of the world population is a carrier of a form of SCD⁴². SCD is a group of inherited hemoglobinopathies affecting over 100,000 individuals in the United States and an estimated > 4 million more worldwide^{43,44}. This group of disorders includes sickle cell anemia (SS), sickle- β^0 -thalassemia ($S\beta^0$), sickle-hemoglobin C disease (SC), and sickle- β^+ -thalassemia ($S\beta^+$)⁴⁵. The most common and severe type of SCD, sickle cell anemia (herein simply referred to as SCD) accounts for over

90% of the sickle-cell disorders worldwide⁴⁴. SCD and SCD trait (heterozygous carriers) are most prevalent in peoples of tropical and sub-Saharan African descent, where the tropical disease malaria is also widespread. It is generally accepted that the prevalence of SCD in these regions is due to genetic selection, where sickle cell trait helps to confer a protective effect against malaria^{46,47}. Although some protection against malaria is a benefit in sickle cell trait carriers, the deleterious effects of homozygous SCD including chronic pain, anemia, and shortened life expectancy pose serious challenges for those afflicted with this disease.

SCD is a recessive inherited autosomal blood disorder that is the result of a single point mutation substituting hydrophilic glutamic acid for hydrophobic valine on the β -globin chain, which mutates hemoglobin (Hb or HbA) into sickle hemoglobin (HbS)⁴⁸. Homozygous inheritance of this mutation causes hydrophobic patches displayed on the HbS β subunit to permit the binding of HbS tetramers to each other in deoxygenated conditions, forming long crystalline or polymeric chains within RBCs and causing these cells to become sickle shaped, rigid, and prone to hemolysis (Figure 1)⁴⁹. Due to their decreased deformability and higher affinity to adhere to the endothelium and other blood cells, sickled RBCs cause blockages in smaller vessels and occlude the microvasculature, resulting in flow obstruction, tissue hypoxia and ischemia, and an inflammatory response^{50,51}. These effects lead to sudden, severe pain due to acute systemic vaso-occlusive episodes (VOE) and acute chest syndrome (ACS), both of which often require acute care and extended hospitalization⁴⁸.

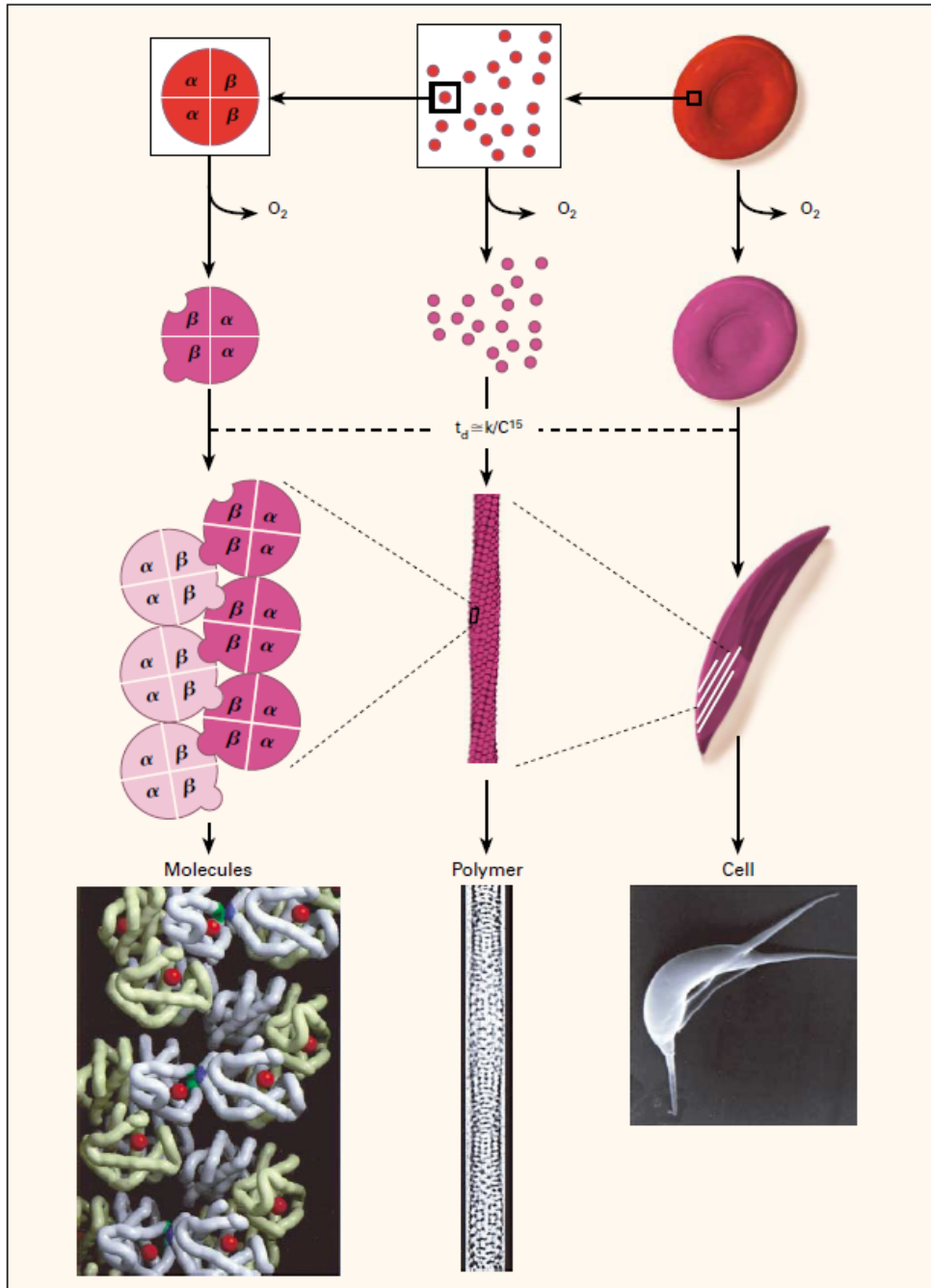


Figure 1. RBC sickling via HbS polymerization. As oxygenated RBCs (bright red) pass through the microcirculation, they deoxygenate (purple) revealing hydrophobic patches on the hemoglobin β subunit. The interaction and binding of multiple deoxygenated HbS units produces intracellular HbS fibers which may align and distort the RBC into the classic “sickle” shape.

Reproduced with permission from Bunn⁴⁹, Copyright Massachusetts Medical Society.

1.2.2 SCD Pathophysiology and Altered Hemorheology

The repetitive cyclic formation of HbS fibers within sickle RBCs is the root of all SCD pathology. As rigid HbS fibers grow and force the cell membrane to distort, the sickle RBC membrane is damaged, eventually causing the cell to prematurely hemolyze. This process results in decreased deformability of sickle RBCs under all oxygen tensions, accelerated cellular dehydration due to impaired ion channel homeostasis, and increased expression of adhesion motifs towards the endothelium and other blood cells⁵². These factors significantly shorten the average lifespan of RBCs from 120 days to approximately 10 – 30 days⁵³. As a result of the chronic anemia seen in SCD patients, sickle RBC blood contains elevated subpopulations of both less-dense reticulocytes (immature RBCs) and abnormally dense dehydrated cells which also include irreversibly sickled cells (ISCs) that can no longer return to their normal biconcave shape following oxygenation⁵⁴. At an equivalent Ht, the viscosity of SCD blood samples is significantly greater than healthy blood under oxygenated conditions and the viscosity difference between SCD blood and healthy blood samples even greater when measured under deoxygenated conditions⁵⁵. Ultimately, these characteristics of poor blood rheology play a fundamental role in the pathophysiology of SCD.

The formation of HbS fibers within sickle RBCs reduces cellular deformability and impairs the passage of RBCs through the microcirculation, increasing their transit time while exposed to deoxygenated conditions⁵⁵. This creates a self-perpetuating positive feedback loop that accelerates the sickling of RBCs towards eventual vaso-occlusion^{52,56,57}. Vaso-occlusion is unpredictably triggered following minimal provocation through infection, stress, dehydration, thrombosis, or of unknown etiology⁵⁰. Vaso-occlusion due to poor sickle RBC rheology may develop into the ill-defined painful vaso-occlusive episode also referred to as VOE, and is the most common reason

for a SCD patient to seek emergency care⁵⁸. An associated life-threatening complication of VOE is the development of ACS which results from pulmonary infiltrate, usually due to vaso-occlusion and inflammation in the pulmonary microcirculation^{50,59,60}.

Additionally, the premature lysis of sickle RBCs and resultant release of plasma free hemoglobin and its metabolic derivatives such as heme groups cause vascular tone dysfunction through Nitric Oxide (NO) scavenging⁵⁰. Cell-free heme groups have also been shown to activate neutrophils and promote sterile inflammation^{50,61}, where the activation of immune and endothelial cells promotes cell-cell adherence and vaso-occlusion⁶². Transient occlusion of microvessels produces ischemia-reperfusion injury (I/RI) which perpetuates sterile inflammation, immune/surveillance cell activation and endothelial dysfunction⁶³. The combination of these inflammatory pathways in addition to poor rheology and sluggish microvessel flow lead to the establishment of what is commonly referred to as a 'vicious cycle' in that each of these pathways contribute to each other, resulting in a perpetual state of poor microvascular flow (Figure 2)^{52,59,64}.

relieving medications such as nonsteroidal anti-inflammatory drugs or opioids may also be prescribed to manage sickle-cell pain crises⁵⁸. Additionally, chronic blood transfusion or exchange transfusions are primary therapies for treatment of anemia or VOE, but these therapies pose a risk for iron overload and alloimmunization complications over the course of multiple treatments⁷⁰. Although emerging treatments such as bone marrow transplantation and gene editing techniques show promise as a cure, these procedures are still experimental and have highly specific criteria, especially for tissue-matched donor marrow^{71,72}. As of the time of this writing, there is no known drug which directly modifies the underlying pathology of SCD or is a purely rheological-based treatment method for SCD.

1.3 Drag-Reducing Polymers

1.3.1 Background

Drag-reducing polymers (DRPs) are a unique class of soluble long-chain high molecular weight (MW) molecules which significantly reduce pressure losses up to 80% within turbulent pipe flow in low concentrations⁷³. This phenomenon, known as the Toms Effect, is only evident in turbulent flows ($Re \gg 4000$) and hypothesized to be due to the reduction of turbulent vortices and eddies as well as absorption of dissipative energy by DRP molecules⁷⁴⁻⁷⁶. The drag-reducing ability of these polymer additives largely depends on their molecular weight ($MW > 10^6$ Da), polymer linearity, and polymer backbone flexibility in solution, with the increase of each of these characteristics improving its drag-reducing effects. Both synthetic and naturally derived DRPs are routinely used in industrial applications to increase flow efficiency and provide cost savings in the

form of decreased pump power requirements or increasing overall output⁷⁶. DRPs are extensively used by the oil and gas industry to transport crude oil over long distances, and they have also been used to improve flow in irrigation systems, firefighting applications, and well drilling-fluid hydraulics⁷⁶. While DRPs do not have a drag-reducing effect on laminar flow systems, it has been found that some drag-reduction behavior is possible in disturbed laminar flows such as pulsating flow or Couette flow with Taylor vortices^{77,78}.

1.3.2 Effects of DRPs *in vitro* and *in vivo*

DRPs have been shown to provide diverse hemodynamic and hemorheological benefits in both *in vitro* and *in vivo* applications. A summary of notable studies on the effects of DRPs in blood flow is shown below in Table 2. These effects have been demonstrated using a variety of both natural and synthetic high MW long-chain polymers of diverse polymer backbone and end group chemistry, indicating that chemical composition is not an adequate explanation for their drag-reducing ability. The administration of a low MW molecule which is also a known DRP at high MW does not elicit similar effects on blood flow, confirming that polymer size and long-chain geometry are primarily responsible for their effects. Further, since the concentration of soluble DRPs required to produce physiologically significant effects within blood flow are in the nanomolar concentration range (2 – 10 ppm or $\mu\text{g/mL}$), the addition of DRPs do not appreciably increase the viscosity of blood suspensions. Finally, DRPs have been shown to produce significant hemorheological effects both *in vitro* and in animal models independent of vessel vasoactivity, indicating that the administration of these blood soluble molecules act in a mechanism which fundamentally alters blood rheology without specifically requiring or acting through signaling pathways.

Table 2. Summary of selected DRP studies, by year published.

Author(s)	Polymer	Experimental Model	Findings / Conclusions
Mostardi et al. (1978) ⁷⁹	PAA	Rabbit, atherosclerosis	Reduction in the development of atherosclerosis
Kameneva, et al. (1988,1990) ^{80,81}	PEO	Small branched tubes	Reduction in eddies and flow separation at bifurcations
Kameneva et al. (2004) ⁸²	PEO, Aloe vera-derived DRP	Rat, hemorrhagic shock	Increased survival following hemorrhagic shock
Pacella et al. (2006 ⁸³ ,2009 ⁸⁴)	PEO	Canine	Reduced microvascular resistance, increase in capillary volume and perfusion
Cotoia et al. (2009) ⁸⁵	hyaluronic acid, PEO	Rat, hemorrhagic shock	Improved perfusion and increased survival without fluid resuscitation.
Marascalco et al. (2009) ⁸⁶	PEO, PMNN	Mouse, PLLA implant	Reduced foreign body reaction to implants
Zhao et al. (2010) ¹⁹	PEO	PDMS microchannel	Elimination of near-wall platelet accumulation in small channels
Chen et al. (2011) ⁸⁷	PEO	Rat, myocardial infarction model	Improved survival, reduced adverse ventricle remodeling
Hu et al. (2011) ⁸⁸	PEO	Rat, acute limb ischemia	Reduced vascular resistance and improved blood perfusion
Brands et al. (2013) ⁸⁹	PEO	Rat, PDMS microchannel	Elimination of plasma skimming effect <i>in vitro</i> and <i>in vivo</i>
Tohme et al. (2016) ⁹⁰	PEO	Mouse	Reduced hepatic injury and metastases after liver ischemia-reperfusion
Bragin et al. (2017) ⁹¹	PEO	Rat, traumatic brain injury	Improvement of cerebral microcirculation following traumatic brain injury and brain ischemia
Ding et al. (2017) ⁹²	PEO	Mouse	Inhibition of experimental metastases of breast cancer cells
Bragin et al. (2020) ⁹³	PEO	Mouse, traumatic brain injury with hemorrhagic shock	Resuscitation with DRP reduces micro thrombosis and oxidative stress

Generally, turbulent flow conditions are not present in the cardiovascular system with the exception of transitional flow in the ascending aorta at peak ejection^{94,95}. Despite turbulent flow being essential for the observation of the Toms effect, DRPs still generate significant changes to blood flow in laminar regimes, indicating that there is a separate phenomenon causing the observed hemodynamic changes.

Several mechanisms have been proposed for the hemorheological changes observed following the administration of DRPs. Upon the initial discovery of their rheological effects, it was proposed that the reduction of flow separations and vortex size at bifurcations was responsible for eliminating pressure losses throughout the circulatory system^{80,81}. This hypothesis rationalizes the increase in pre-capillary pressures and capillary recruitment seen *in vivo* and it may help to explain the now well-documented ability of DRPs to drastically improve tissue perfusion⁸⁴, reduce lethality from hemorrhagic volume loss⁸², and prevent the formation of atherosclerosis⁷⁹.

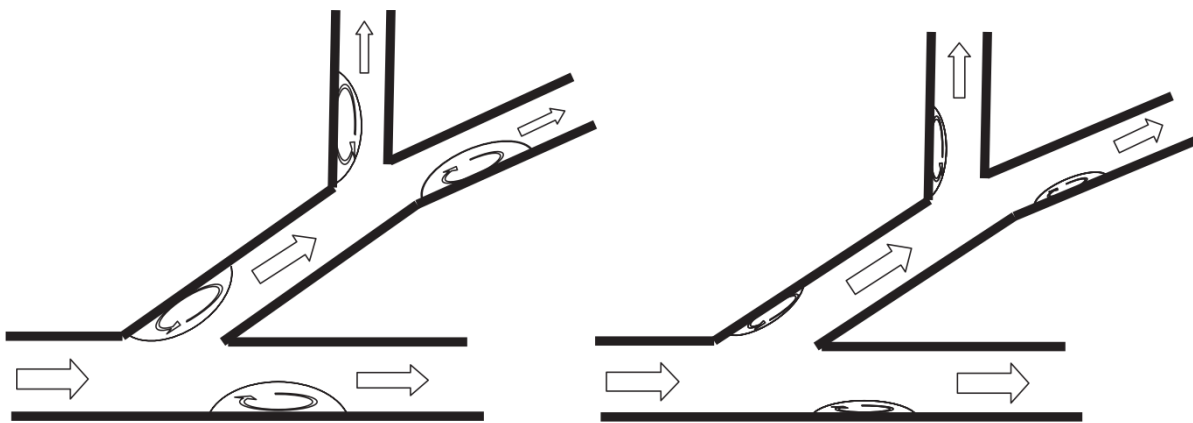


Figure 3. Schematic of recirculation zones following blood vessel bifurcations before (left), and after the administration of DRP (right). Figure reused from Kameneva⁹⁶ with permission.

Later, it was discovered that DRPs have the unique ability to reduce or eliminate the size of the near-wall plasma CFL in small vessels, creating a more homogeneous distribution of cellular

components radially across the diameter of the vessel^{82,97}. This effect produces several key hemorheological changes which may be attributed to the beneficial effects previously documented. First, increased near-wall RBC occupation reduces the plasma skimming effect (Figure 4), thus increasing the number of RBCs entering smaller vessels and allowing for more effective gas exchange and mass transfer⁸⁹. This effect increases capillary effectiveness and recruitment especially following injury or significant blood volume loss⁸². Second, the replacement of the less viscous plasma layer with increased levels of RBCs sharply increases the near-wall shear rate and shear stress⁹⁷, which may interfere with the rolling, arrest, and adhesion of leukocytes or platelets. This action is hypothesized to be the explanation as to why DRPs have been shown to reduce inflammatory responses observed in animals implanted with biodegradable scaffolds⁸⁶ and in experimental models of ischemia/reperfusion injury (I/RI)⁹⁰, as well as reduce cancer metastases⁹², which also require adhesion to extravasate into tissue.

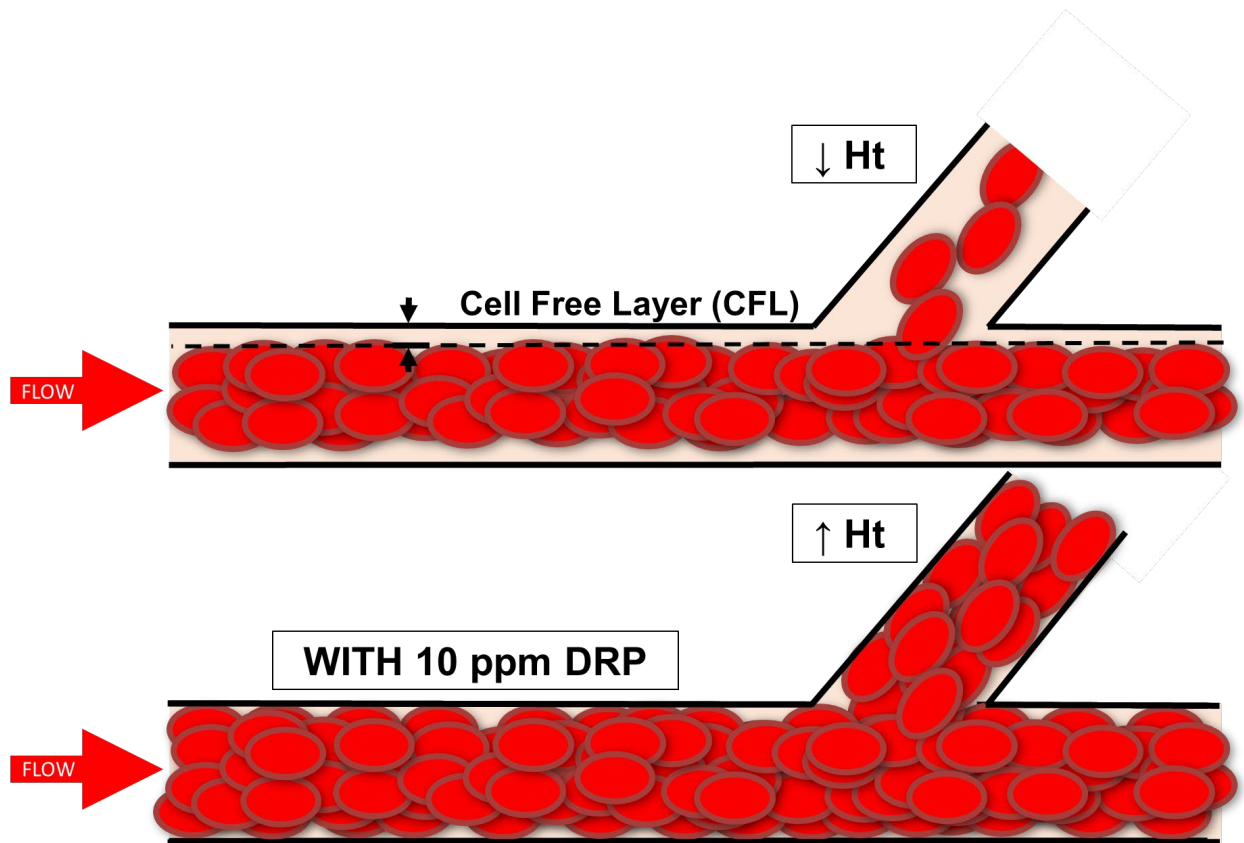


Figure 4. DRPs eliminate the CFL and reduce the plasma skimming effect within microvessels by increasing daughter branch outlet hematocrit (Ht).

Although it has been previously found that the effects of DRPs are independent of vessel vasoactivity⁹⁸, elevated wall shear rates may help improve tissue perfusion via the release of nitric oxide, a potent vasodilator. While the complete mechanisms producing these effects are still not completely understood, it is most likely not the case that there is a single mechanism responsible for the variety of documented effects. Rather, multiple interacting hemorheological changes are likely responsible for the favorable outcomes seen in such diverse applications.

1.3.3 Degradation of DRPs and Considerations for Clinical Use

The degradation of DRPs and subsequent loss of their drag-reducing qualities has been extensively studied since their inaugural use in industrial applications^{76,99}. However, with potential for future clinical use, many characteristics such as degradation, sterilization ability, and storage must be carefully examined to determine the viability of DRPs in a clinical setting. While many different synthetic and naturally derived DRP molecules have been used with great success for *in vivo* experiments, this work focuses on the water-soluble DRP poly(ethylene oxide) (PEO) (Figure 5). Although PEO and another polymer, poly(ethylene glycol) (PEG), have identical chemical structures, they derive their names from differences in MW, where higher MW polymers are referred to as PEOs (MW > 100,000 Da) and, lower MW polymers (MW < 100,000 Da) are referred to as PEGs. Because of their low MW, PEG polymers do not have any drag-reducing properties while PEO polymers are potent drag-reducers.

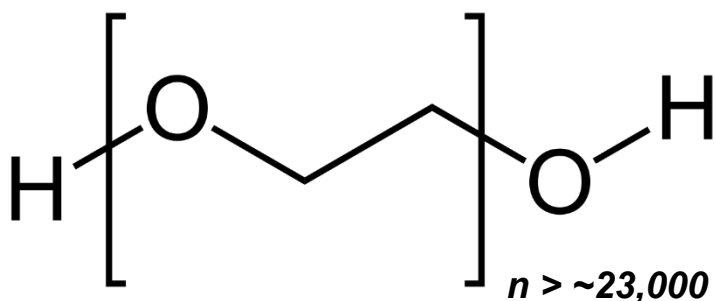


Figure 5. The chemical structure of PEO.

The direct connection between MW (analogous to polymer length) and the drag-reducing capabilities of PEO makes degradation of these macromolecules an extremely important clinical consideration. Mechanically induced degradation is especially well documented due to the

frequent use of DRPs within high shear environments, and is attributed to the disentanglement of polymer macromolecules and the shear-induced destruction of the polymers' backbone^{76,99}. PEO in particular is susceptible to degradation via chain scission upon exposure to oxidizing agents, ultraviolet light, and certain heavy metals¹⁰⁰. Thus, PEO stabilization requires careful consideration when subjected to various sterilization techniques or storage methods so as not to diminish the polymer's drag-reducing capabilities. For example, some traditional methods of sterilization such as autoclaving or UV irradiation would not be suitable candidates for PEO processing. The most feasible method of sterilization for clinical use appears to be gentle filtration through 0.22 μm sterile filters, which can limit exposure of the polymers to harmful shear stresses, oxidizing agents, or environments. This technique has been successfully used in *in vivo* DRP experiments showing no loss of their drag-reducing effects⁹¹.

1.4 Objectives

The preservation of microvascular blood flow is essential to the well-being of all mammals, yet many pathologies detrimentally affect the healthy flow of microvessels. SCD is the most commonly inherited blood disorder in the United States, and results in the occlusion of microvessels as a direct consequence of poor RBC hemorheology. Episodes of vaso-occlusion deprive tissues of oxygen and nutrients, which in addition to causing pain and ischemic organ damage, may progress to multi-organ syndromes such as VOE or ACS. Despite standard and emerging treatment options, the hospitalization prevalence of SCD patients remains high and presents an extraordinarily high economic burden of over 1.1 billion dollars annually in the US^{48,101}. Any improvement of microvascular blood flow for SCD patients that directly reduces or

prevents vaso-occlusion would substantially improve outcomes and the quality of life for many of those suffering from SCD, as well as a significant reduction in economic burden. The overarching purpose of this work is to develop and test two novel rheological-based approaches as potential options for the treatment of SCD. These approaches include the intravascular use of DRPs as well as a novel method of intracellular hemoglobin replacement therapy. This was accomplished through *in vitro* and *in vivo* studies in pursuit of the following three specific aims:

1.4.1 Study the Effects of DRP on Cellular Traffic *in vitro* Within Bifurcating Microchannel Models

The mechanism(s) with which DRPs act upon the microcirculatory system are still incompletely understood. The goal of this specific aim is to better understand the effects of DRP on the distribution of RBCs as they flow within bifurcating microchannels. This study examines the ability of DRPs to alter the traffic of mixtures of normal and less-deformable RBCs through branched microchannels and is intended to support and expand upon previous experiments within straight capillary tubes to promote DRPs for future clinical use. The conclusions of this work suggest that DRP additives may be used to improve microcirculation *in vivo* and indicates their potential for future clinical use.

1.4.2 Determine the Influence of DRP *in vivo* on Vaso-Occlusion and Neutrophil Aggregation in Transgenic SCD Mice

Vaso-occlusion within the microcirculation is a primary pathophysiology of SCD. The microcirculation of the mouse liver was intravitaly imaged using multiphoton microscopy to determine the occurrence of vaso-occlusion with lipopolysaccharide (LPS) as an inflammatory instigator. The influence of circulating DRP on vaso-occlusion was quantified in Townes transgenic SCD mouse models. The objective of this specific aim is to confirm our hypothesis that DRP decreases vaso-occlusion *in vivo* due to (at least in part) the mechanistic pathways found in Specific Aim 1. Reduced vaso-occlusion in SCD mouse models with the introduction of DRP may ultimately lead to decreased risk for VOC in SCD patients, and would merit additional exploration of DRP as a potential treatment option for SCD.

1.4.3 Perform Feasibility Testing for Intracellular Hemoglobin Replacement as a Novel Form of SCD Transfusion Therapy

One of the primary therapies for sickle cell disease is chronic transfusion of donor blood. Over time, 58% of chronically transfused patients will develop alloantibodies to these foreign RBCs making it difficult or impossible to identify compatible donors¹⁰². The primary objective for this aim was to develop a protocol wherein HbS will be removed from RBCs obtained from SCD patients and the hemoglobin replaced with healthy donor Hb while retaining the integrity of the patient's original RBC membrane. We hypothesized that newly refilled RBCs not containing HbS will lose their ability to sickle under hypoxic conditions and would have improved viscoelastic properties, thus improving their ability to perfuse the microvasculature and deliver oxygen when re-introduced to patients as an autologous blood transfusion.

2.0 The Effects of DRP on Cellular Traffic *in vitro* Within Bifurcating Microchannels

Results discussed in this chapter have been submitted to the *ASAIO Journal* and are currently accepted pending revisions as a manuscript entitled: “Hemorheological Approach to Improve Perfusion of RBCs with Reduced Deformability Using Drag-Reducing Polymer (in vitro study)” by Dan Crompton, Shushma Gudla, Jonathan H. Waters, Prithu Sundd, and Marina V. Kameneva.

Drag-reducing polymers (DRPs) are nontoxic water-soluble blood additives which have been shown to beneficially alter hemodynamics when delivered intravenously in nanomolar concentrations. This study examines the ability of DRPs to alter the traffic of mixtures of normal and less-deformable RBCs through branched microchannels and is intended to support and expand upon previous experiments within straight capillary tubes to promote DRPs for future clinical use. Branched polydimethylsiloxane (PDMS) microchannels were perfused with a mixture of normal bovine RBCs also containing heat treated less-deformable RBCs at a hematocrit of 30% with 10ppm of the DRP poly(ethylene oxide) (MW 4MDa). Suspensions were driven by syringe pump, collected at outlets, and RBC dimensions measured while subject to shear stress to determine the proportion of healthy RBCs in each sample. DRPs eliminated evidence of the plasma skimming phenomena and significantly increased the pressure drop across microchannels. Further, DRPs were found to cause an increase in the proportion of healthy RBCs exiting the branch outlet from $-8.5 \pm 2.5\%$ (control groups) to $+12.1 \pm 5.4\%$ ($n = 6, p = 0.02$). These results suggest DRP additives may be used to improve the perfusion of less-deformable RBCs *in vivo* and indicates their potential for future clinical use.

2.1 Introduction

Due in large part to their deformability, red blood cells (RBCs) will naturally radially migrate toward the center of vessels and channels under 300 μm in diameter, creating an RBC-rich central core. This phenomenon, known as the Fåhræus Effect leaves an RBC-poor fluid layer near the vessel wall otherwise called the cell-free layer (CFL)⁹. The thickness of the CFL may vary between 1 to 10 μm and is dependent on vessel diameter, Ht, flow velocity, RBC aggregation, and RBC deformability¹². The formation of the RBC central core also results in the margination of less-deformable cells towards the vessel wall such as platelets, leukocytes, and less-deformable RBCs¹⁰³. The margination of these cells increases their likelihood of being ‘skimmed’ into smaller vessels at bifurcations, which increases their concentration within the microvasculature and may increase their tendency to obstruct flow due to their poor deformability or size²⁴. Further, as a result of the RBC-poor fluid layer at the vessel periphery, a larger proportion of plasma enters smaller vessels at bifurcations reducing the microcirculatory hematocrit (Ht) to 20-50% than that of larger vessels¹⁷. This work focuses on how the addition of blood soluble drag-reducing polymers (DRPs) alter the traffic and relative concentration of less-deformable RBCs and healthy RBCs within branched *in vitro* microchannel models of the microvasculature.

DRPs are a unique class of soluble long-chain, high molecular weight ($\text{MW} > 10^6$ Da) molecules which significantly reduce pressure losses within turbulent pipe flow by up to 80% in low concentrations (Toms Effect)⁷³. DRPs are routinely used in industrial applications as a means of increasing flow efficiency and cost savings⁷⁶. Generally, turbulent flow conditions are not present in the cardiovascular system with the exception of transitional flow in the ascending aorta at peak ejection. Despite turbulent flow being essential for the observation of the Toms Effect, DRPs still generate significant changes to blood flow in laminar regimes, indicating that there is a

separate phenomenon occurring to cause the hemodynamic changes seen with the addition of DRP. Previous studies have shown that DRPs provide numerous beneficial hemorheological effects including increased capillary perfusion and oxygenation in animal models⁸², reduced liver ischemia/reperfusion injury⁹⁰, improvement of cerebral blood flow following traumatic brain injury⁹¹, increased survival following hemorrhagic shock⁸², increased survival following severe myocardial ischemia¹⁰⁴, and inhibition of experimental metastases of human breast cancer cells in mice⁹². Although not yet fully understood, the underlying mechanism of DRPs is theorized to originate from its ability to reduce flow separation and vortex size at bifurcations and significantly reduce or eliminate the width of the CFL⁹⁶. Additional studies have also shown that the DRP induced elimination of the CFL significantly reduces the margination of platelet-sized particles resulting in a more uniform distribution of rigid particles across the channel diameter¹⁹. The use of DRP blood additives to alter the margination of less-deformable cells is of particular interest for its potential to influence and improve microcirculatory blood flow.

Reduced RBC deformability is well known in blood disorders such as malaria and spherocytosis but is especially well documented as a result of RBC aging and in the case of sickle cell disease (SCD)¹⁰⁵. In this work we examine how the loss of RBC deformability affects the traffic patterns between healthy and less-deformable cells in microchannels, especially with the administration of DRP. We hypothesized that DRP additives to microchannel blood flow would lead to a reduction of marginating less-deformable RBCs. This action would decrease their susceptibility of being ‘skimmed’ into daughter branches and may lead to an increase in healthy (more deformable) RBCs found in daughter branches. The understanding of the microvascular effects DRPs have on blood flow, especially concerning populations of less-deformable RBCs has implications for the improvement of perfusion and is a step towards the practical clinical use of

DRPs. To test this hypothesis and improve our understanding of the mechanisms with which DRPs act upon small vessels, we conducted bifurcating microchannel flow studies using blood containing a mixture of both healthy and less-deformable RBCs.

2.2 Materials and Methods

2.2.1 Sample Preparation

Whole, fresh bovine blood obtained via venipuncture and anticoagulated in K₂EDTA was purchased from Lampire Biological Laboratories (Pipersville, PA) by overnight shipment. Whole blood was received on ice less than 24 hour after the time of drawing, and used in experiments only if samples were not delayed during shipment, were still chilled from the ice packs, and if samples were not found to contain any thrombus or above normal plasma free hemoglobin levels. Samples were consumed or discarded within 48 hours of receipt. Blood was filtered through a 40 µm blood transfusion filter (Haemonetics, Braintree, MA) and washed 3x with phosphate buffered saline (PBS) without Mg²⁺ or Ca²⁺ (Lonza, Switzerland) at 2000 g for 15 minutes and resuspended at 30% Ht in PBS with 1% bovine serum albumin (BSA) (Sigma Aldrich, St. Louis, MO). Fresh bovine blood suspensions at 30% Ht were used to verify the existence of the plasma skimming effect and were mixed with either the DRP polyethylene oxide (PEO) (molecular weight 4e10⁶ Da, Sigma Aldrich, St. Louis, MO) at a final concentration of 10 ppm (10 µg/ml) or an equal volume of the vehicle (PBS).

In following experiments, a mixture containing equal amounts of both healthy and less-deformable RBCs was prepared for the purpose of identifying the traffic patterns of RBCs based

on their deformability. Less-deformable RBCs were created via heat-treatment, an established method to produce RBCs with irreversible loss of membrane deformability^{106,107}. Less-deformable RBCs were treated for 30 minutes at 52°C in a Neslab RTE-7 hot water bath (Thermo Fisher Scientific, Waltham, MA). This method was found to reliably produce less-deformable RBCs without significant increases in RBC destruction as measured by plasma free hemoglobin release. RBC loss of deformability was verified visually under shear stress using a Linkam shearing stage (Linkam Scientific, Tadworth, UK) which is described in greater detail later in this section. A clear difference in RBC deformability between healthy and less-deformable RBCs is pictured in Figure 9. For use in microchannel experiments the mixture of healthy and less-deformable RBCs was prepared by mixing equal volumes of 30% Ht healthy RBCs with 30% Ht less-deformable RBCs, which was then split into two pools, either receiving DRP for a final concentration of 10 ppm or an equal volume of PBS.

2.2.2 Experimental Setup

Custom polydimethylsiloxane (PDMS) microchannels manufactured using soft lithography techniques from SynVivo Inc. (Huntsville, AL) were used in all experiments. Microchannels were designed with a height of 50 μm , 200 μm main channel diameter, and 100 μm daughter channel at a 45° bifurcation. PE-60 tubing (Braintree Scientific, Braintree, MA) was attached to inlet and outlet ports and their lengths minimized to prevent blood sedimentation. Channels were permanently bound to glass slides and passivated prior to experimentation with a 3% BSA solution. Blood was driven through the inlet of the channel via syringe pump (PhD Ultra Syringe Pump, Harvard Apparatus, Holliston, PA) in a syringe containing a miniature stirring rod

with which blood was gently mixed by adjacent stir plate to prevent RBC sedimentation. Pressure drop across the microchannel was measured using a pressure transducer which was calibrated against atmospheric pressure and a known pressure using a calibrated manometer. Outlet blood samples were collected at the level of the microchannel (Δ height = 0) in small reservoirs open to the atmosphere. Schematics of the microchannel and experimental setup are pictured in Figure 6 and Figure 7.

Validation of the plasma skimming effect within microchannels was verified using the blood suspensions not containing heat treated (less-deformable) RBCs. Samples were driven through microchannels at a rate of $5.9 \mu\text{L}/\text{min}$, and collected in triplicate from the parent and daughter outlets for Ht determination using micro-hematocrit glass capillary tubes (SurePrep heparinized capillary tubes; BD Clay Adams, Sparks, MD).

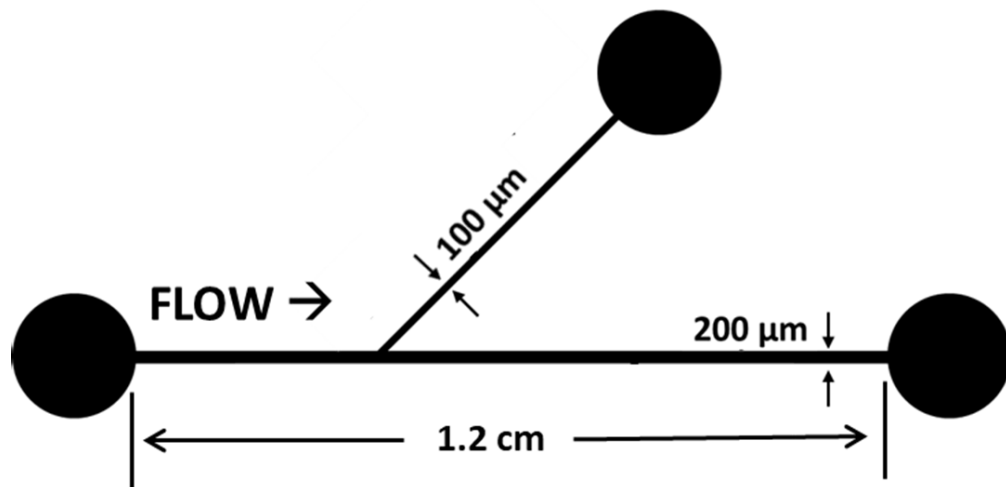


Figure 6. Schematic of custom PDMS microchannels. Main channel dimensions: $200\mu\text{m}$ (width) x $50\mu\text{m}$ (height), Daughter branch dimensions: $100\mu\text{m}$ (width) x $50\mu\text{m}$ (height). The main channel total length is 1.2 cm, and the daughter branch channel length is 0.4 cm. Note: schematic pictured is not to scale.

Blood suspensions containing a mixture of healthy and less-deformable cells were used for the determination of RBC traffic through microchannel bifurcations. Samples containing the mixture of both healthy and less-deformable RBCs were driven through microchannels at a rate of 5.9 $\mu\text{L}/\text{min}$ and collected from the parent and daughter outlets. Collected blood samples were then diluted in a suspension of isotonic 5.6% polyvinylpyrrolidone (PVP) (Sigma Aldrich, St. Louis, MO) and imaged while subject to shear stress using a Linkam shearing stage (Linkam Scientific, Tadworth, UK). RBC suspension in viscous PVP solution allowed for a greater range of deliverable shear stresses using the Linkam shearing stage. All samples, including those containing DRP were significantly diluted prior to deformability measurements by a 1:250 dilution (4 μL sample to 1 mL PVP solution) to prevent overlap of RBCs during image capture. The presence of DRP in samples was estimated to be approximately 0.04 ppm following PVP dilution and was not found to influence the results of deformability or logistic regression analysis.

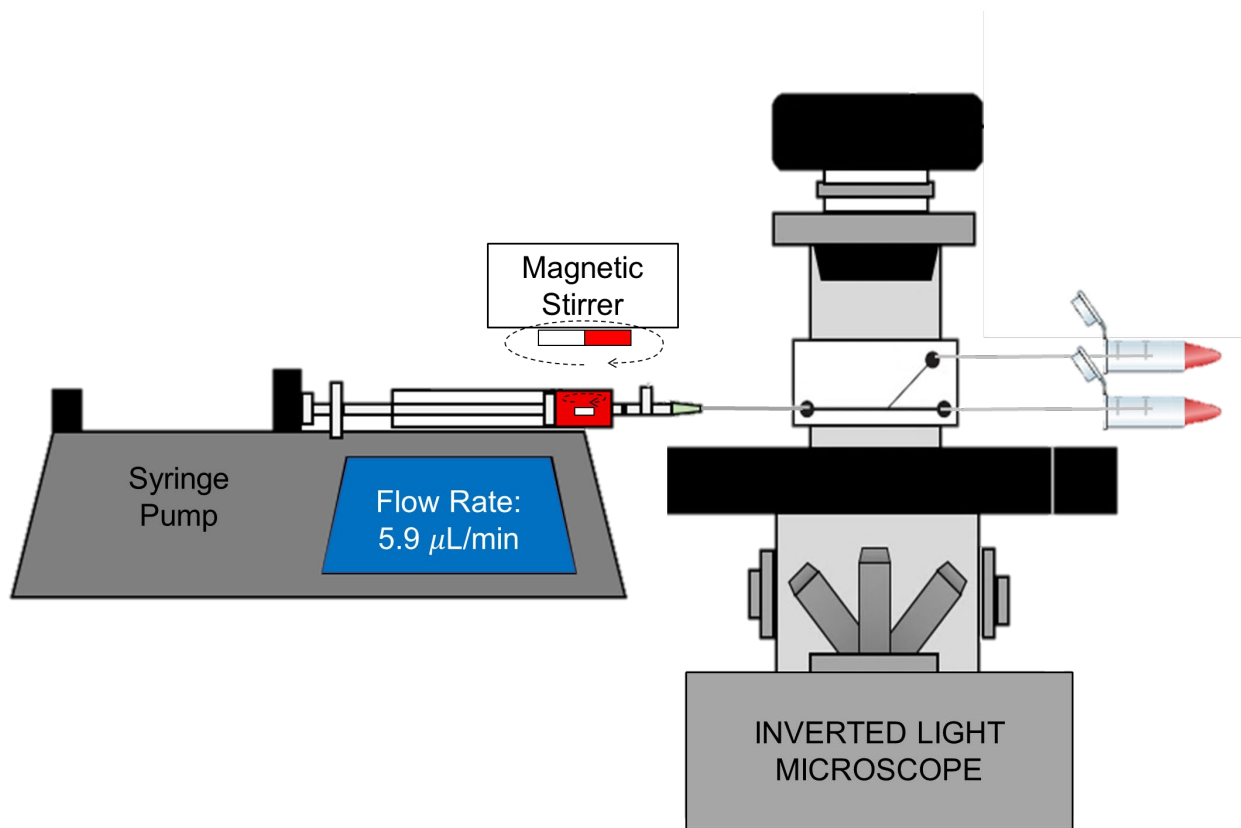


Figure 7. Experimental microchannel setup schematic.

2.2.3 Determination of RBC Deformability Via Ellipsometry

The Linkam CSS450 shearing stage (Linkam Scientific, Tadworth, UK) was used for the measurement of RBC deformability in this body of work. This system uses two parallel disks to produce Couette flow which can be imaged through a quartz aperture offset a known distance from the center of rotation¹⁰⁸. The system schematic and geometry are depicted in Figure 8.

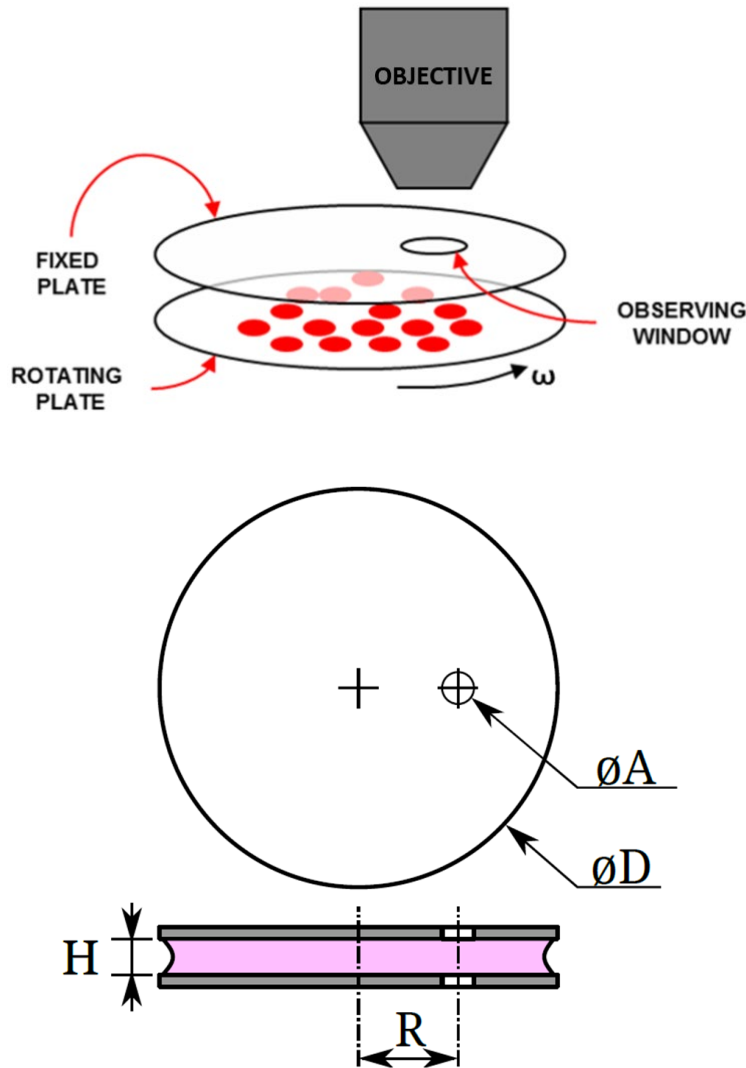


Figure 8. Linkam CSS450 parallel-plate shearing stage schematic (top) and parallel disk geometry (bottom). Aperture diameter (A , 2.5 mm), Disk diameter (D , 30 mm), Radius from center to aperture (R , 7.5 mm), and gap height (variable, set at 50 μm). Figure adapted with permission from Hellmuth¹⁰⁹.

Polyvinylpyrrolidone (PVP) at a concentration of 5.6 g/dL was suspended in isotonic solution (PBS w/o Ca^{2+} and Mg^{2+}), covered and gently rocked for 24-48 hours until homogeneous. PVP viscosity was measured prior to its use for the purpose of calculating delivered shear stresses.

The suspension of RBCs in viscous PVP solutions allowed for a greater range of deliverable shear stresses at lower shear rates while using the Linkam shearing stage. 3-4 μL of blood at a Ht of approximately 30% was pipetted into 1 mL of PVP solution and mixed until homogeneous. 100 μL of the sample were then pipetted onto the Linkam shearing stage which was gently closed and set to a gap height of 50 μm . Individual cells were brought into focus using a stroboscope (X-Strobe X400, Perkin Elmer, Salem, MA), focusing on cell midlines to create silhouettes for optimal cell size measurements. Samples were then sheared at desired rates ranging from 1 to 1000s^{-1} , and imaged using a top mounted camera (QiCAM, QImaging, Burnaby, Canada) at 50x magnification. The NIH-developed open source image processing program ImageJ¹¹⁰ was used to determine cell height and widths with the default threshold and particle analyzing tool, using specific parameters to omit overlapping cells, debris, or shadow. Please refer to Appendix C.1 for ImageJ particle analysis used in this work. Representative figure of images captured using the Linkam shearing device along before and after image processing are pictured in 9. Cellular deformability of the sample being measured may then quantified using the elongation index (EI):

$$\text{EI} = |(\text{length} - \text{width})/(\text{length} + \text{width})| \quad \text{Equation 2.1}$$

2.2.4 Image Processing

Images of RBCs were captured while samples were exposed to 52 Pa of shear stress (shear rate 1000 s^{-1}) and analyzed using ImageJ where individual cell height and widths were collected after thresholding and using the particle analyzing tool to omit overlapping cells, debris, or out of focus RBCs. Samples were measured in duplicate with upwards of 5000 individual RBCs analyzed

per sample to ensure consistency. Manual cell measurements were also performed using the ImageJ platform to check the accuracy of the particle analyzing tool and were found to be consistent. Figure 9 shows both representative images of RBCs captured while flowing under shear stress and identified RBCs following image analysis.

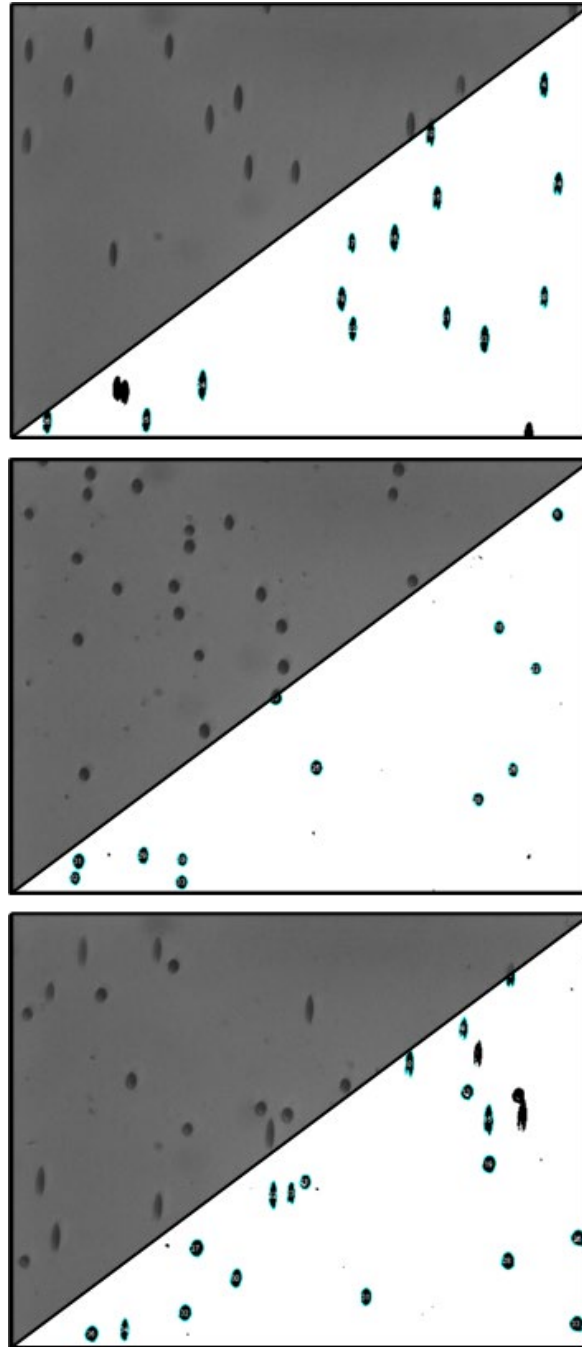


Figure 9. Representative images of healthy (Top), less-deformable (Middle), and mix of healthy and less-deformable (Bottom) RBCs captured using the Linkam device at 52 Pa of shear stress (1000s^{-1}). For each image, top-left cut-outs show original images, with the bottom-right cut-out showing results after image processing and measurement. Note overlapping RBCs, cellular debris and uneven illumination areas are not falsely counted as measured RBCs (cyan outline).

2.2.5 Data Analysis

A detailed description of the logistic regression algorithm and samples of the MATLAB scripting used to determine the proportion of healthy and less-deformable RBCs may be found in Appendices C.2 through C.5.

Briefly, a logistic regression algorithm for binary classification was used to determine the proportion of healthy and less-deformable RBCs found in each sample using the cell height and width measurements collected during image processing. Less-deformable cells could then easily be differentiated from deformable RBCs in an automated method. Before each experiment, RBC measurements from samples containing exclusively healthy and rigidified RBCs were plotted as cell length vs. cell width. Using this data, a decision boundary line or gate was drawn between the two groups of data. The slope and intercepts of the decision boundary line was optimized to minimize the error found when separating the two binary classifications (healthy vs. less-deformable RBCs) using a logistic regression algorithm. Using this decision boundary line, the classification of unknown RBC mixtures could then be determined using their height and width measurements based on their position above (healthy) or below (less-deformable) the decision boundary line. A graphical interpretation of the algorithm and description of this process is outlined in detail in Appendix B.1. The accuracy of the algorithm classifying cells as either healthy or less-deformable using training data was found to be > 99%.

Following the classification of cells, the relative percent of healthy cells to less-deformable cells exiting the branch outlet was then normalized to the sample blood pool using the formula:

Relative Percent (%)

$$= \left[\frac{\%Healthy\ RBCs_{Branch} - \%Healthy\ RBCs_{Main}}{\%Healthy\ RBCs_{Blood\ Pool}} \right] * 100 / Ht \quad \text{Equation 2.2}$$

where a positive relative percent value indicates more healthy RBCs exiting the daughter branch outlet than the main outlet, when normalized by the blood pool. A negative relative percent values indicated a larger majority of less deformable cell exiting the daughter branch outlet than the main outlet, when normalized by the blood pool.

2.2.6 Statistical Analysis

The matched, paired Student's t-test was used to evaluate differences between control and DRP groups. A value of $p < 0.05$ was assumed to indicate statistical significance.

2.3 Results

2.3.1 Microchannel Parameter Calculation

At a flow rate of 5.9 $\mu\text{L}/\text{min}$, the calculated wall shear rate found in the main channel was $1180\ \text{s}^{-1}$, with a Reynolds number of 0.34. The flow rate within the daughter channel branch was estimated using the volume of the blood sample collected divided by the running time of the experiment and was found to be approximately 2 uL/min , with no differences found between

control and samples containing DRP. The calculated wall shear rate of the daughter branch was found to be 900 s^{-1} , with a Reynolds number of 0.25. Similarly to previous work performed by Marhefka et al, the pressure drop across the entire microchannel was elevated in samples containing 10 ppm DRP ($10.9 \pm 4.2 \text{ mmHg}$) as compared to control blood samples ($5.6 \pm 1.5 \text{ mmHg}$), due to the increased near-wall viscosity caused by the elimination of the near wall CFL⁹⁷ (Figure 10).

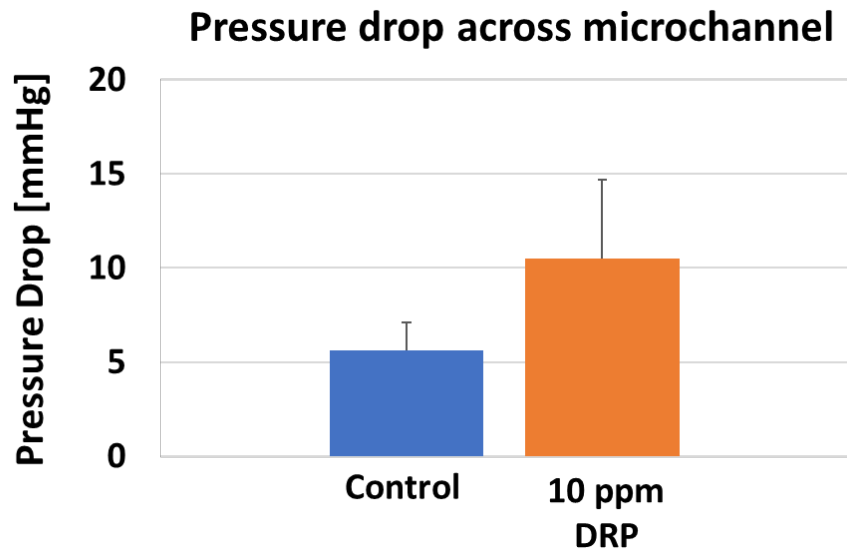


Figure 10. The measured pressured drop across the microchannle experiences a significant increase with the addition of nanomolar concentrations of DRP, theorized to be due to the reduction in the near-wall CFL and increase in the near-wall viscosity. $n = 5, p < 0.01$.

2.3.2 Microchannel Validation / Verification of the Plasma Skimming Effect

The presence of the plasma skimming effect and the existence of the CFL in our microchannel model was found using healthy blood at 30% Ht driven through our bifurcating

microchannels. Control blood samples were found to have a statistically significant drop in Ht between the parent branch and that of the daughter branch efflux ($p = 0.017$). The Ht of samples exiting the main outlet was $31.6 \pm 1.0\%$, while the Ht of the blood exiting the daughter branch was $28.3 \pm 2.2\%$. Conversely, the addition of 10 ppm of the DRP PEO demonstrated the elimination of the plasma skimming effect which led to non-significant differences between the parent and daughter branch efflux Ht (Figure 11). The Ht of samples containing 10 ppm DRP exiting the main outlet was $29.7 \pm 0.6\%$, while the Ht of the blood exiting the daughter branch was $28.5 \pm 1.4\%$.

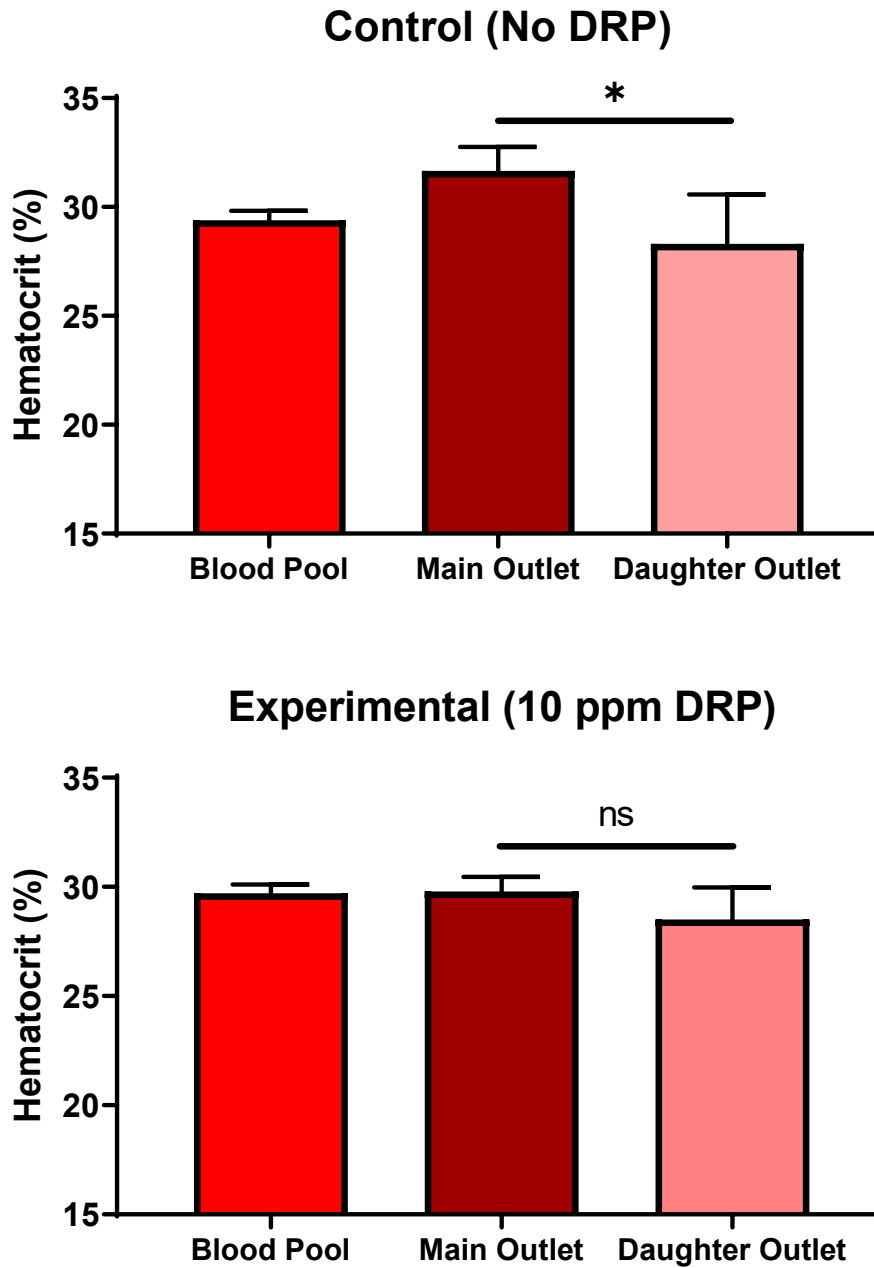


Figure 11. The plasma skimming effect, showing a decreased Ht in the daughter outlet as compared to the main ($n = 5$, $p = 0.017$) (Top). Non-significant Ht changes between main and daughter outlets with the addition of DRP, indicating the elimination of both the CFL and the plasma skimming effect ($n = 7$, $p > 0.05$) (Bottom).

2.3.3 Hemorheological Characterization of the Less-Deformable Blood Mixture

Preliminary work involving characterization of the deformability and viscosity of the heat treated less-deformable RBCs and mixtures were conducted prior to their use in microchannels. The RBC rigidification protocol was optimized for the production of the least deformable RBCs while incurring minimal hemolysis and maximum loss of deformability. This resulted in developing a hot water bath heat treatment protocol of 30 minutes at 52° C, pictured in Figure 12.

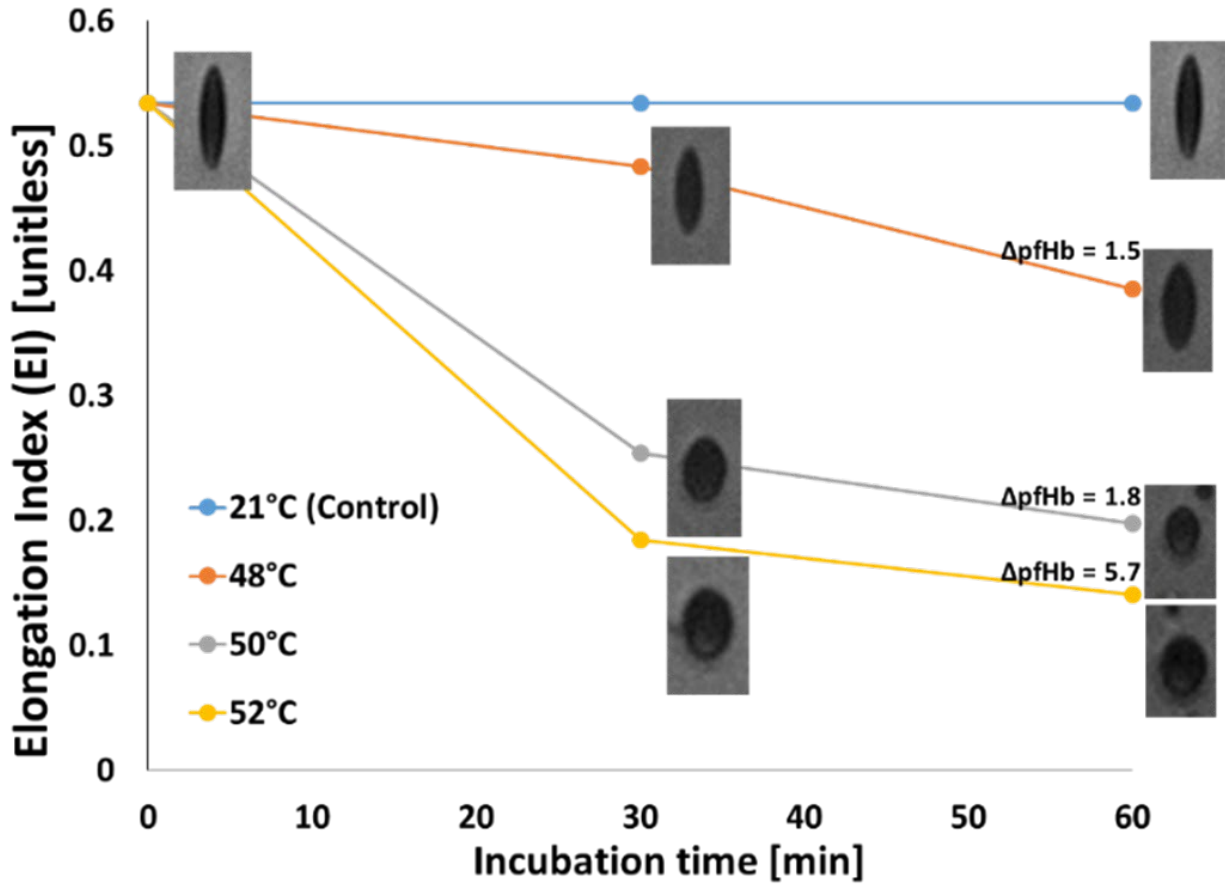


Figure 12. RBC rigidification protocol was found to be best using a 52°C water bath for 30 minutes for bovine blood. Measured plasma-free hemoglobin (Δ pfHb) was measured in mg/dL.

Data points not showing Δ pfHb values were negligible.

The viscoelasticity of the less-deformable RBCs and mixtures containing less-deformable RBCs were measured and compared. As expected, the viscosity of the heat-treated RBCs at identical Ht was elevated due to a reduction in deformability (Figure 13). A 50/50 mix of healthy and heat-treated RBCs was made to simulate the reduced deformability and increased viscosity of the blood from a red cell disorder such as SCD. This mixture of healthy and heat-treated RBCs was found to have a closely matched viscosity to SCD blood, especially at shear rate > 200.

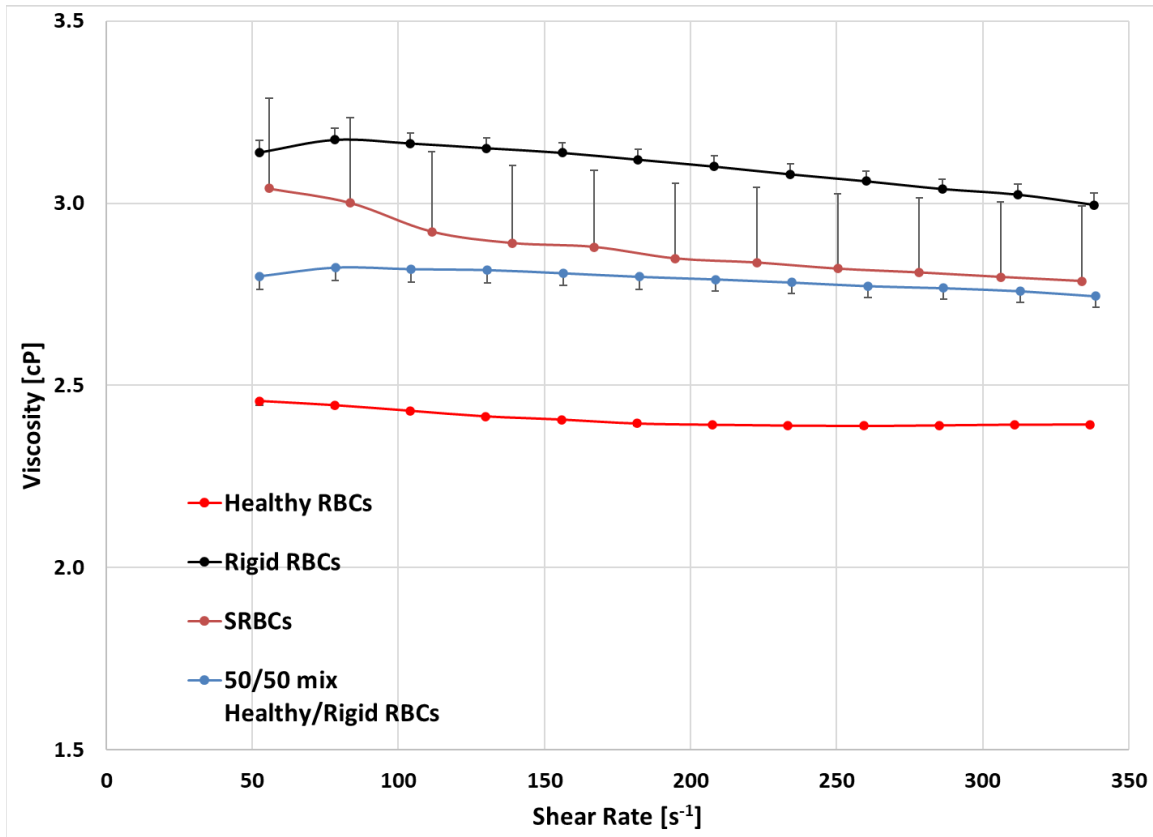


Figure 13. Viscosity measurements collected with the Vilastic-3 showing elevated viscosity of bovine RBCs following heat treatment (rigid) and compared to healthy and sickle RBCs (SRBCs). All samples were measured at 30% Ht and at room temperature. SCD blood viscosity measurements for comparison were collected from work performed in Chapter 4. Error bars represent mean \pm SE.

2.3.4 Distribution of Less-Deformable RBC Traffic Through Daughter Branch Outlets

It was found that the 50:50 mixture of healthy and less-deformable RBCs exhibited asymmetrical RBC flow patterns when driven through our bifurcating microchannels. In control experiments (without DRP), the relative percent of healthy RBCs exiting the daughter branch was

found to be $-8.5 \pm 2.5\%$, indicating an increased proportion of less-deformable RBCs exiting the daughter branch. Conversely, with the addition of 10 ppm DRP, it was found that relative percent was increased to $+12.1 \pm 5.4\%$, indicating more healthy RBCs exiting the daughter branch (Figure 4).

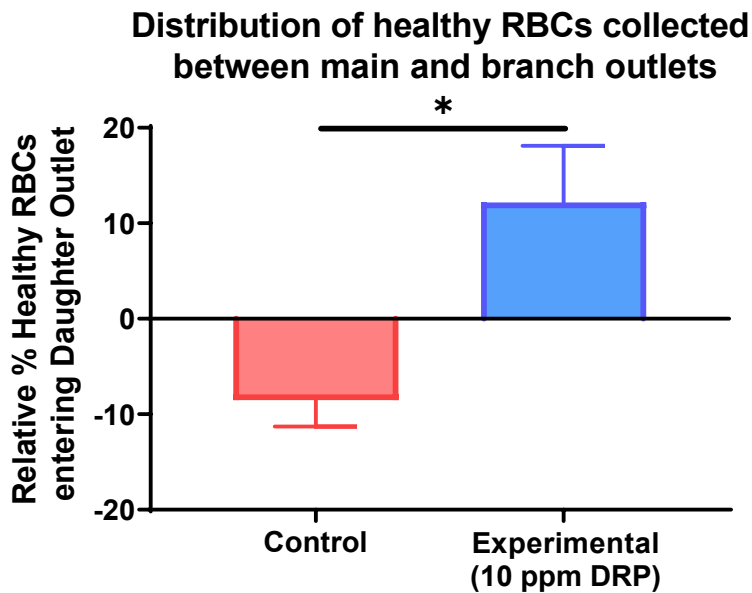


Figure 14. The percent differences of healthy RBCs between branch and main outlets. In control groups, an average of $-8.5 \pm 2.5\%$ fewer healthy RBCs exited the branch outlet than less-deformable RBCs. In groups with 10 ppm DRP, an average of $+12.1 \pm 5.4\%$ more healthy RBCs exited the branch outlet than less-deformable RBCs ($n = 6$, $p = 0.02$).

2.4 Discussion

The results discovered in these experiments imply a beneficial effect to blood flow within the microcirculation. The reduction of the near-wall CFL was determined by the increase in pressure drop across the microchannel and a non-statistical difference between parent and daughter

branch Ht. The increase in pressure drop across the microchannel is attributed to the increase in viscosity of the near-wall fluid layer as more viscous RBCs move into the vessel periphery. While not intuitively beneficial in a single microchannel model, an increase in the near-wall viscosity caused by DRPs has been shown to improve the number of functioning capillaries through recruitment of the capillary reserve and increase in pre-capillary pressures⁸⁴. Although the intravascular effects of DRPs are independent of vasoactivity⁹⁸, the increase in wall shear stress and shear rate, the vessel periphery may also improve perfusion through the release of shear-mediated vasodilatory agents such as nitric oxide (NO). In this study, the elimination of the plasma skimming effect following a single bifurcation also resulted in a homogeneous Ht distribution between main and daughter microchannels branches. This would suggest that the plasma skimming effect may be attenuated within the microvasculature, further improving the perfusion of all blood cells within individual small vascular branches.

The novel findings that DRP additives alter the local traffic of blood cells based on their deformability also poses clinical significance. Although reduced deformability is a natural phenomenon of RBC aging, the loss of deformability may be accelerated due to blood disorders such as SCD. Alternatively, aged RBCs with impaired mechanical properties may be transfused into the body^{111,112}. While not an inherent cause of microvascular vaso-occlusion, the loss of RBC deformability is a well-known contributor towards increased microvessel transit times and decreased perfusion of the microvascular system^{34,113}. The use of DRPs to increase the traffic of healthy, more deformable RBCs into daughter vessel bifurcations may help to maintain higher levels of microvascular flow to preserve or improve tissue oxygenation.

Finally, the ancillary observation of elevated wall shear stresses may also prevent immune surveillance cells from creating strong adhesions with the endothelium. In specific disease states

such as SCD where rampant inflammation is a major contributor towards vaso-occlusion, this effect may interfere with immune cell rolling, activation, and extravasation. Although warranting further study, this effect may help to suppress the pro-inflammatory state which leads to vascular dysfunction in SCD. This theory has been partially observed *in vivo*, where following liver ischemic/reperfusion injury, DRPs were shown to reduce neutrophil extracellular trap (NET) formation and platelet micro thrombi⁹⁰. Similarly, the administration of DRP has been shown to inhibit the extravasation and metastasis of human breast cancer cells in mice⁹², where the interaction and adhesion between endothelial, immune, and circulating tumor cells are known to play an important role in the development of metastases. The potential disruption of adhesion interactions between endothelial and circulating blood cells caused by the introduction of DRP would likely attenuate the incidence of vaso-occlusion of SCD *in vivo*, and warrants further examination.

While the entire mechanistic effect of DRP is not fully understood, this work takes a step towards their understanding using a bifurcating microchannel model. The conclusions drawn in this study demonstrate the potential of DRPs to alter the traffic of blood cells based on their deformability, and improve the microvascular flow of blood also containing less-deformable cells through daughter branches. Many questions remain unanswered surrounding the use of DRPs as a medical therapy; future study of their effects in both microchannel and animal models will serve to further validate the use of DRPs for their eventual clinical use.

2.4.1 Study Limitations

Visualization and labeling of flowing RBCs within our microchannel model could provide additional information on their margination and flow patterns. Future work is planned using multiphoton microscopy to circumvent these problems in later studies. Finally, a potential source of experimental error may have been introduced via the logistic regression algorithm used to identify healthy vs. less-deformable RBCs, however the training data used to validate this measurement system was found to show a high degree of accuracy and data replication was achieved when using blinded measurements also taken by hand.

2.5 Conclusions

This study demonstrates the novel finding that nanomolar additives of DRPs alter the traffic of less-deformable RBCs through bifurcations of branched microchannels. We hypothesized that the mechanism behind this effect was related to the documented ability of DRPs to reduce the size of the near-wall CFL. This effect caused less-deformable RBCs which were previously more likely to be skimmed into bifurcations to be replaced with normal RBCs, and increased the proportion of normal cells flowing through daughter branches. The conclusions of this study implicate the use of DRPs in the future as a means of improving microcirculatory blood flow *in vivo*.

3.0 The Influence of DRP *in vivo* on Vaso-Occlusion and Neutrophil Aggregation in Transgenic SCD Mice

The results discussed in this chapter have been published as: Crompton D, Vats R, Pradhan-Sundd T, Sundd P, and Kameneva MV. Drag-Reducing Polymers Improve Hepatic Vaso-occlusion in SCD Mice. *Blood Advances*. 2020 4(18) pp. 4333-4336¹¹⁴.

3.1 Introduction

Sickle cell disease (SCD) is an autosomal recessive blood disorder affecting over 100,000 individuals in the US⁴³. Mutant sickle hemoglobin (HbS) polymerizes within red blood cells (RBCs) under deoxygenated conditions resulting in cell rigidity, hemolysis, and vaso-occlusion⁷². These events catalyze an inflammatory response which can lead to acute painful vaso-occlusive episodes^{50,72}. Acute pain is the predominant cause for the seeking of medical treatment and results in an estimated cost of medical care for those with SCD of over 1.1 billion annually^{48,101}. The role of impaired hemorheology in SCD and its contribution towards vaso-occlusion is well documented^{52,105,115,116}. Poor blood rheology including elevated whole blood viscosity, plasma viscosity, RBC membrane rigidity, and cytosolic viscoelasticity impedes microvascular blood flow by increasing intravascular resistance and decreasing RBC velocity^{117,118}. Abnormal cellular adhesion markers presented on sickle RBCs due to membrane damage and on prematurely released reticulocytes further contribute to impaired flow and the precipitation of vaso-occlusion^{50,119,120}.

Recently, it has been shown that blood additives known as drag-reducing polymers (DRPs) beneficially alter blood rheology and significantly improve the hemodynamics and outcomes of animals following hemorrhagic shock⁸², liver ischemia/reperfusion injury⁹⁰, and traumatic brain injury⁹¹, while simultaneously providing increased capillary recruitment, perfusion, and oxygenation⁹⁸. However, the effects of DRPs are unknown in the context of SCD, where a rheology-based therapy to improve microcirculatory blood flow has the potential to greatly reduce the incidence of vaso-occlusion. In this study, we have used quantitative liver intravital microscopy (qLIM) to show that the administration of nanomolar concentrations of DRPs reduces vaso-occlusion within liver sinusoids of transgenic SCD mice following inflammatory stimulus via lipopolysaccharide (LPS).

3.2 Materials and Methods

3.2.1 Reagents and DRP Preparation

Polyethylene oxide (PEO, molecular weight 4000 kDa, Sigma-Aldrich, MO) was dissolved in sterile saline to a concentration of 0.2% (2000 ppm) and gently mixed for 4-6 hours. On the day of experimentation and prior to injection, PEO was diluted with sterile saline to 50 ppm and slowly rocked to ensure a homogeneous mixture. A new stock PEO solution was created for each experiment and solutions were not stored to eliminate the possibility of polymer storage-induced degradation. Lipopolysaccharide (LPS) derived from *Escherichia coli* O111:B4 was purchased from Sigma Aldrich (St. Louis, MO). Ketamine HCl (100 mg/mL) was purchased from Henry Shein Animal (Dublin, OH). Xylazine (20 mg/mL) was purchased from Lloyd Laboratories

(Shenandoah, IA). Texas Red Dextran (TXR-dextran, MW, 70 kDa) was purchased from Thermo Fisher Scientific (Waltham, MA). Alexa Fluor 546 rat anti-mouse Ly6G mAb clone 1A8 was purchased from Biolegend (San Diego, CA).

3.2.2 Mice

Male and female (12-16 weeks old) Townes SCD mice (SS, homozygous for $Hba^{tm1(HBA)Tow}$, homozygous for $Hb^{btm2(HBG1,HBB^*)Tow}$) were used in this study¹²¹. Experiments using non-sickle control (SCD trait mice (SA), homozygous for $Hbatm1(HBA)Tow$, compound heterozygous for $Hbb^{tm2(HBG1,HBB^*)Tow}/Hbb^{tm3(HBG1,HBB)Tow}$) were also conducted separately. All experiments were approved by the Institutional Animal Care and Use Committee at the University of Pittsburgh.

3.2.3 Surgical Preparation and qLIM Imaging

SCD Mice were injected with 0.1 μ g/kg LPS from *Escherichia coli* O111:B4 which was mixed with 50 μ L of either 50 ppm DRP solution or sterile saline into the tail vein. Approximately 1 hour later, mice were anesthetized with an intraperitoneal injection of 100 mg/kg of body weight ketamine HCl and 20 mg/kg of body weight xylazine. A tracheotomy was performed for mechanical ventilation with 95% O₂ and supply maintenance anesthesia (1-1.5% isoflurane). Mice were repositioned in the supine position and the right lobe of the liver was exposed and immobilized using a micro-machined liver window for imaging. The liver viewing window was

held through the use of light suction. The right carotid artery was cannulated for delivery of intravascular dyes including Texas Red (TXR)-dextran and Alexa Fluor 546 rat anti-mouse Ly6G mAb clone 1A8 used to visualize blood plasma and neutrophils respectively. qLIM movies were captured using a Nikon MPE multi-photon excitation microscope (Center for Biologic Imaging, University of Pittsburgh) at approximately 15 frames per second over a field of view (FOV) measuring 263 μm by 263 μm with 10-15 different FOVs recorded for each mouse. Details of the experimental methodology and setup are pictured in Figure 15 and have also been described in detail elsewhere^{122,123}.

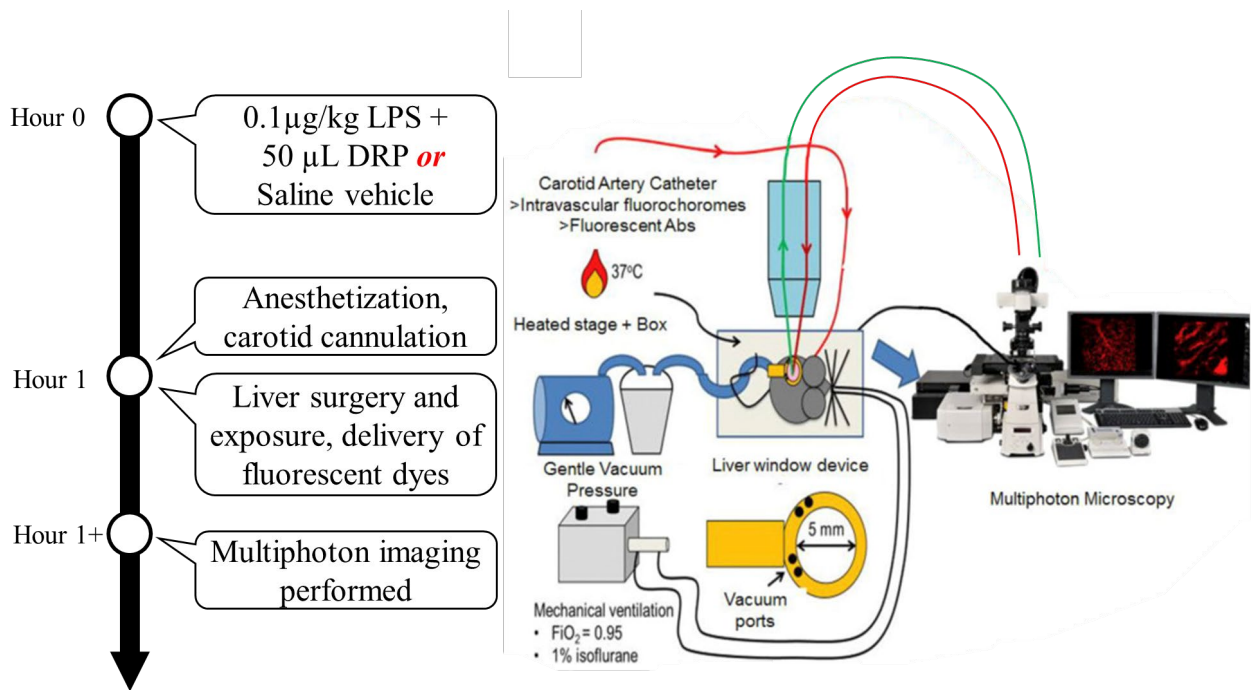


Figure 15. Schematic diagram of experimental process and qLIM imaging setup. Figure adapted with permission from Pradhan-Sundd et al¹²².

3.2.4 Image Analysis

All movies were processed using FIJI (ImageJ v2.0) software¹²⁴. Image subtraction was used to remove autofluorescence and minimize bleed through between channels, followed by the application of a 3x3 median filter to reduce noise. Signal contrast was further enhanced by adjusting the maxima and minima of the intensity histogram associated with each channel. All image processing operations were performed uniformly on every image frame over the entire FOV. Blood vessel identification and segmentation was performed using the Weka Segmentation tool (v3.2.33)¹²⁵ on FIJI. Only vessels identified with clearly defined (in focus) borders and having both borders of the vessel wall within the FOV were subject to quantitative analysis. Vaso-occlusion was defined as the complete and permanent cessation of all cellular traffic being identified during movie capture. Liver microcirculation in mice was observed using qLIM for maximum of 30 min. During this time, we did not see any resolution of sinusoidal vaso-occlusion. This finding is identical to the findings reported in our previous study¹²³. Areas of vaso-occlusion were defined as far as the cellular blockage was clearly visible within the vessel, and vessels without cellular traffic during image capture were not considered to be occluded. The percentage of flowing vessel area was quantified in addition to the count (quantity) of flowing vessels per FOV. Neutrophil-containing vaso-occlusions were defined as 2 or more neutrophils found within a vaso-occlusive region and within the lumen of the blood vessel(s). Multiple neutrophil-containing regions of vaso-occlusion were counted within a FOV only when occluded areas were within separate regions of microvascular branches or were separated by areas of flowing microvessels.

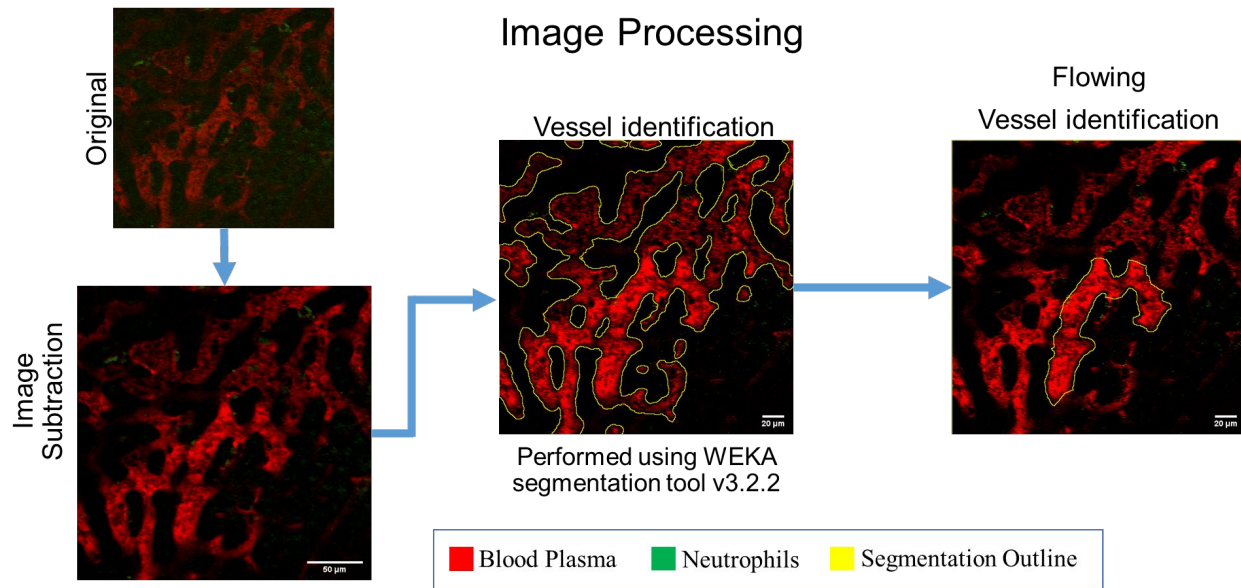


Figure 16. Flowchart of the image processing performed.

3.2.5 Statistical Analysis

The matched paired two-tailed Student's t-test was used to evaluate differences between SCD mice treated with LPS and SCD mice treated with both LPS and DRP. A value of $p < 0.05$ was assumed to indicate statistical significance.

3.3 Results

3.3.1 Experiments Performed on Mice Homozygous for SCD

Multi-photon qLIM imaging was used to observe the liver *in vivo* in SCD mice. Some degree of blood flow was observed in all mice, however large regions of vaso-occlusion were also

observed following inflammatory stimulus by intravenous LPS. Three SCD mice treated with LPS (39 FOVs) and three SCD mice treated with both LPS and DRP (30 FOVs) were used in this study. Blood flow in ~30 blood vessels was assessed in each FOV. As pictured in Figure 17, all vessels within the FOV were first identified using the Weka segmentation tool. For the sake of clarity and consistency, the same representative movie stills are shown for each step of the image analysis process.

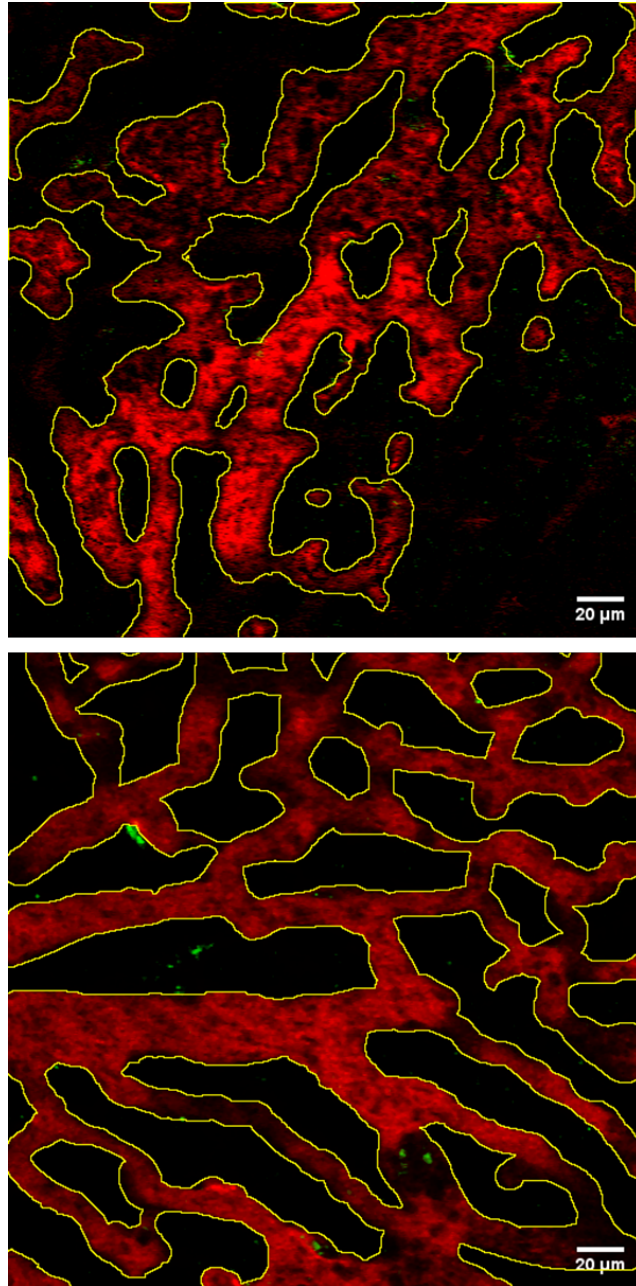


Figure 17. All vessels identified following the intravital qLIM imaging process. Representative still frame of SCD mouse liver receiving LPS (Top) and experimental animal still frame of SCD mouse liver receiving both LPS and DRP (Bottom). (TXR)-dextran and Ly6G green were used to stain the blood plasma and neutrophils respectively. RBCs can be discerned as dark shapes within the vessels and were not stained. Yellow outlines denote areas identified as vessels, with

20 μm scale bars.

Regions within the identified vessels which maintained flow throughout the image capture sequence were determined and labeled as flowing vessels. These regions were likewise identified within the FIJI/ImageJ software platform and used for the quantification of the percentage of microvessel flow maintained following LPS inflammatory stimulus (Figure 18).

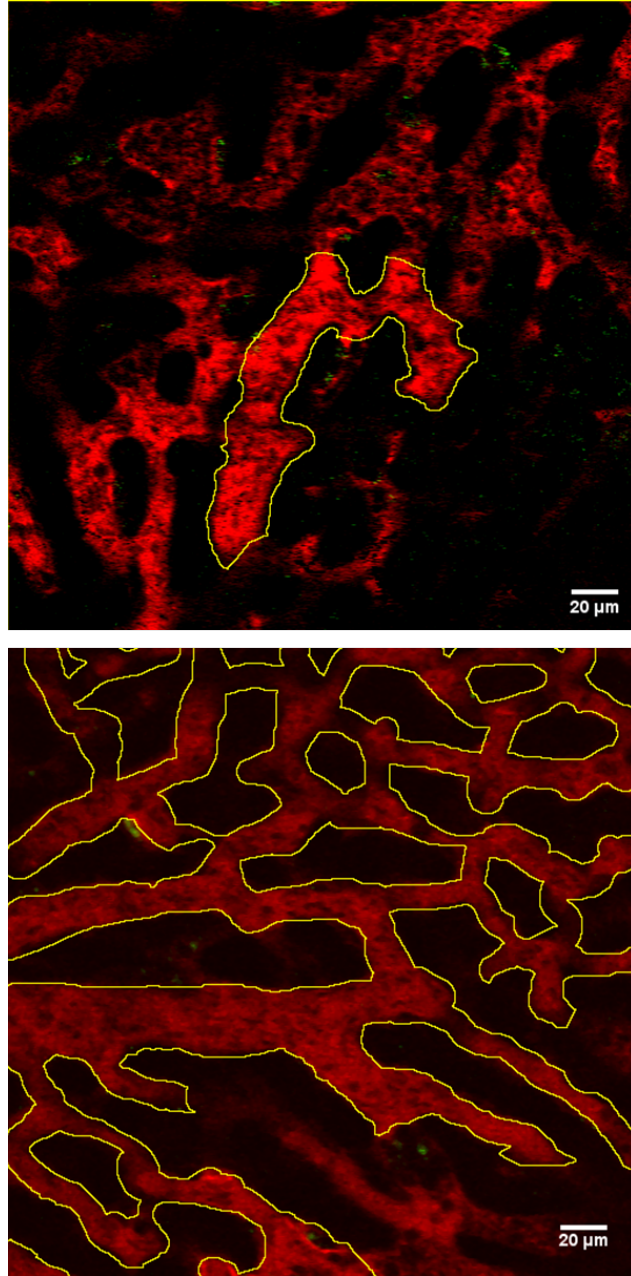


Figure 18. Segmentation of only flowing vessels identified following the intravital qLIM imaging process. Representative still frame of SCD mouse liver receiving LPS (Left) and experimental animal still frame of SCD mouse liver receiving both LPS and DRP (Right).

(TXR)-dextran and Ly6G green were used to stain the blood plasma and neutrophils respectively. RBCs can be discerned as dark shapes within the vessels and were not stained.

Yellow outlines denote areas identified as flowing vessels, with 20 μm scale bars.

DRPs significantly reduced the degree of vaso-occlusion observed within the liver sinusoids of SCD mice. Quantification of the total area of vessels in which microvessel flow was maintained revealed that only $35.0 \pm 4.8\%$ of microvessels remained flowing in SCD mice only receiving LPS animals, compared to $62.4 \pm 4.8\%$ in animals receiving both LPS and 10 ppm DRP (Figure 19). In similar findings, the administration of 10 ppm DRP also significantly increased the percentage of individual flowing vessels from $24.4 \pm 3.5\%$ to $56.3 \pm 5.1\%$ (Figure 20).

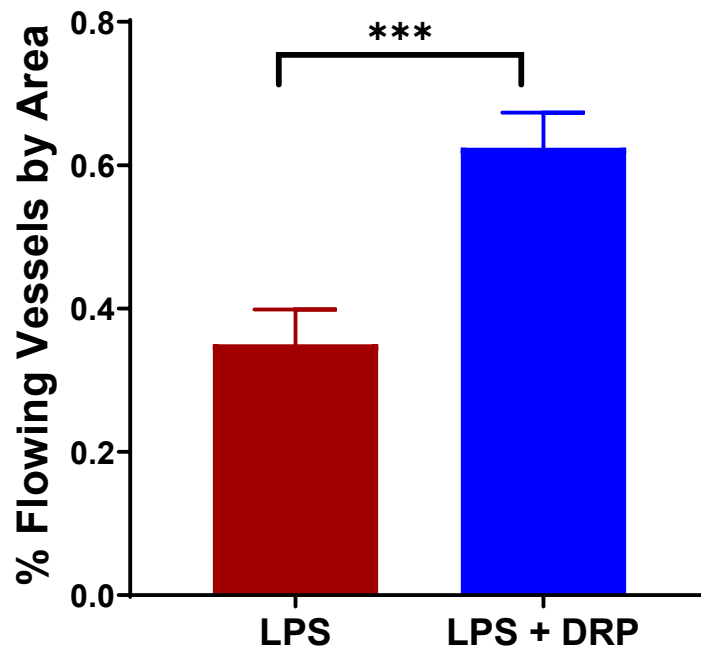


Figure 19. Quantification of the percentage of total flowing vessel area per FOV. Data presented as mean \pm SE, where *** denotes $p < 0.001$.

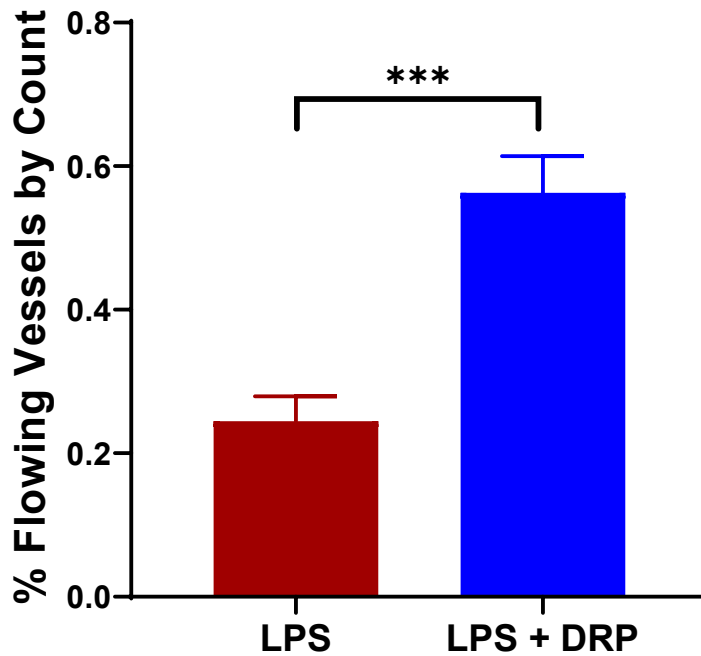


Figure 20. Quantification of the percentage of total flowing vessels per FOV by their individual count. Data presented as mean \pm SE, where *** denotes $p < 0.001$.

Examination of the number of neutrophil containing vaso-occlusions in each FOV demonstrated a significant increase in their number in SCD mice only receiving LPS compared to SCD mice receiving both LPS and DRP. A representative still from a SCD mouse only receiving LPS which includes a neutrophil containing vaso-occlusion and expanded inset is pictured in Figure 21. Quantification of the number of neutrophil containing vaso-occlusion in each FOV revealed an average of 9.02 ± 0.85 neutrophil containing vaso-occlusions in mice only receiving LPS, compared to 4.18 ± 0.72 in animals receiving both LPS and 10 ppm DRP (Figure 22).

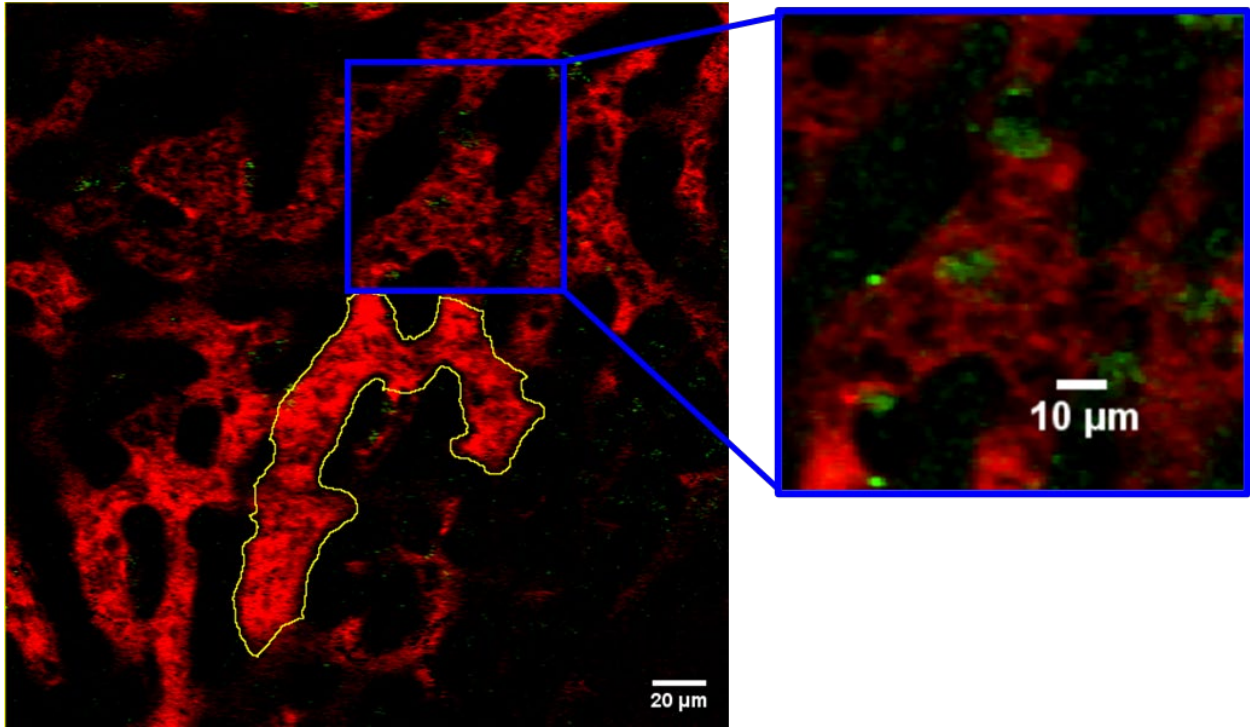


Figure 21. Still image from a SCD mouse receiving LPS showing a large neutrophil containing vaso-occlusion region in inset. Inset depicts occluded liver sinusoid with multiple neutrophils surrounded by RBCs within the luminal space. (TXR)-dextran and Ly6G green were used to stain the blood plasma and neutrophils respectively.

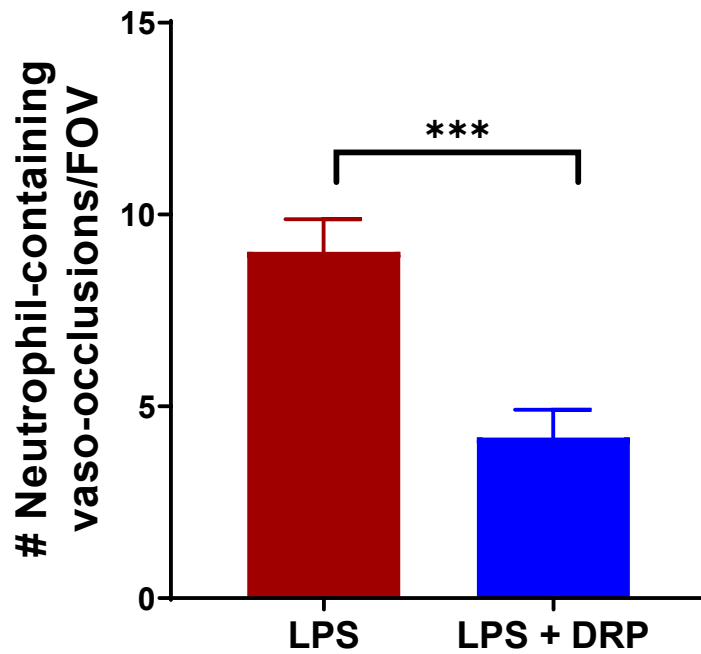


Figure 22. Number of neutrophil-containing vaso-occlusion per FOV in SCD mice. Data presented as mean \pm SE, where *** denotes $p < 0.001$.

3.3.2 Experiments Performed on SCD Trait (SA) Mice

Identical experiments performed on SCD trait (SA) mice were also conducted to evaluate the impact of LPS on liver vaso-occlusion at baseline (without DRP). The similarity of results found in this work and identical experiments performed in work by Vats et al¹²³, showcase the consistency of the experimental model and validation of the quantification methods used in this study. As pictured in Figure 23, nearly 100% percent of the vessels identified across all mice remained flowing ($n = 2$, FOVs = 21). No vaso-occlusions in SCD trait mice were found to contain neutrophils.

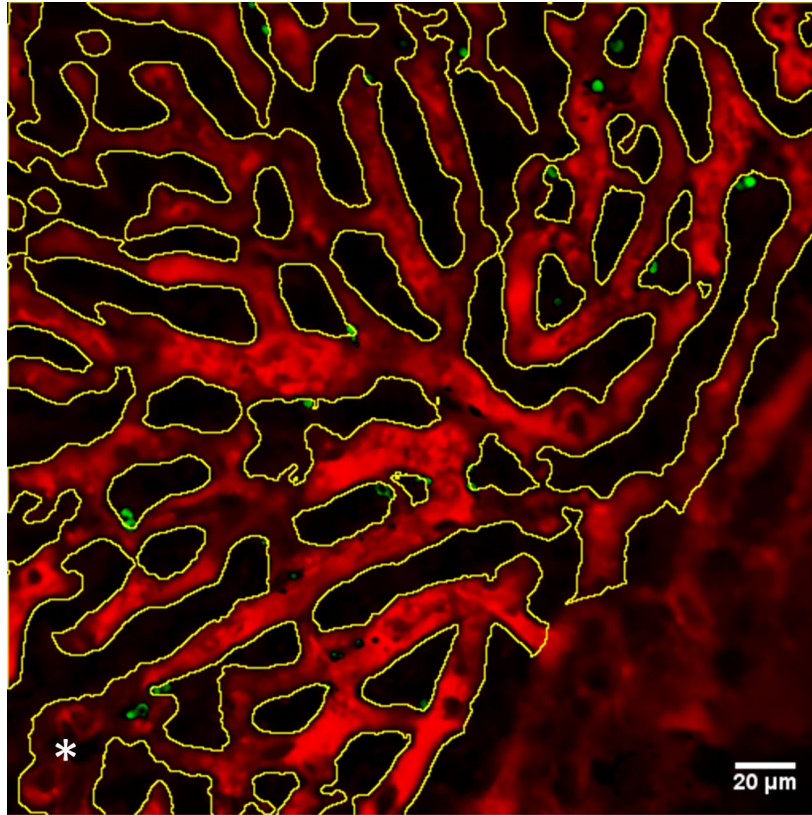


Figure 23. Representative SCD trait (SA) image, with all flowing vessels identified in yellow. Regions of vaso-occlusion are marked with *. (TXR)-Dextran and Ly6G green were used to stain the blood plasma and neutrophils, respectively. RBCs can be discerned as dark shapes within vessels and were not stained. Note region in bottom left of image still which was not analyzed due to out of focus vessels boundaries. Yellow outlines denote areas identified as vessels, with 20 scale bars.

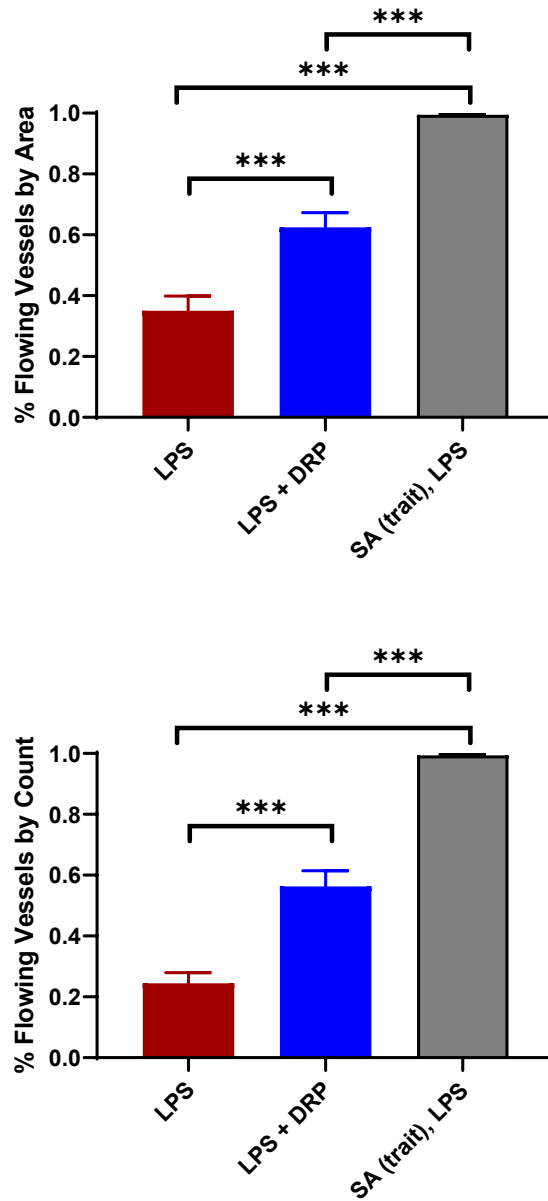


Figure 24. Sickle Cell trait (SA) mice receiving the same volume of LPS did not exhibit the same degree of vaso-occlusion as mice homogeneous for SCD. Quantification of percentage of flowing vessels by total area (top), and quantification of the percentage of total flowing vessels per FOV by their individual count (bottom). Data presented as mean \pm SE, where *** indicates $p < 0.001$. A total of 21 FOVs of the SA (trait) mice given LPS were collected and analyzed, with a subject count of $n = 2$.

3.4 Discussion

Vaso-occlusion within the liver sinusoids of SCD mice was successfully observed using qLIM. Given the recently documented transient liver ischemia and damage in SCD mice under basal conditions¹²³, all mice were observed to present some degree of vaso-occlusion following LPS inflammatory stimulus. The geometry or tortuosity of vessels did not appear to influence the likelihood of vessel vaso-occlusion. As shown in Figure 18, increased levels of vaso-occlusion were observed in SCD mice administered intravenous LPS compared to SCD mice administered both LPS and DRP. The administration of DRP resulted in a significant increase in both the percent area as well as the percentage of flowing vessels per FOV (Figure 19, Figure 20). Further, it was found that DRP significantly reduced the number of vaso-occlusions containing two or more neutrophils (Figure 22).

Although the rheological mechanisms of DRPs are not fully understood, it is currently hypothesized⁹⁶ that their ability to increase precapillary pressures and improve capillary recruitment and perfusion is a direct result of their reduction of flow separations and small vortices within blood vessels^{80,97}. We hypothesized that these mechanisms may help to reduce SCD vaso-occlusion by ameliorating flow stagnation, thereby reducing the probability that a single transient vaso-occlusive event would occur and/or propagate into the occlusion of a larger area. Further, the ability of DRP to diminish the width of the microvasculature near-wall “cell-free layer” has been shown to reduce plasma skimming into capillaries⁹⁷, increase near-wall shear stress and RBC

velocity⁹⁸, and has been shown to prevent the peripheral margination of platelets¹⁹. The demargination of immune surveillance cells accompanied by increased microvascular near-wall shear rates may potentially disrupt adhesion molecule interactions and possibly attenuate the risk of neutrophil induced vaso-occlusion. Comparable observation of this effect has previously been documented *in vivo*, where the administration of DRP demonstrated reduced neutrophil extracellular trap formation and platelet microthrombi⁹⁰, as well as inhibition of human breast cancer cell extravasation⁹². Previously, we have shown that DRP prevents margination of rigid particles within microchannels¹⁹. In the current study, we show that intravenous administration of DRP prevents intravenous LPS-triggered vaso-occlusion in the liver sinusoids. Taken together, these findings suggest a potential role for sickle RBCs in sinusoidal vaso-occlusion. The relative contribution of adhesion vs increased stiffness of RBCs to sinusoidal vaso-occlusion as well as the efficacy of DRP in preventing vaso-occlusion in lung, spleen, and other organs will be investigated in future studies.

3.5 Conclusions

In conclusion, our findings suggest that DRPs can be beneficial in preventing ischemic liver injury of SCD. These findings also warrant the need for further clinical studies to assess the efficacy of DRPs as a rheology-based prophylactic therapy to prevent ischemic-organ injury in SCD patients.

4.0 Development of an Intracellular Hemoglobin Replacement Therapy for the Potential Treatment of SCD and Rheological Characterization of Modified RBCs

4.1 Introduction

For SCD patients, the transfusion of red cell products remains a primary therapy¹²⁶ for the treatment of anemia, the dilution of circulating sickle RBCs, and the improvement of oxygen carrying capacity^{127,128}. Transfusions may either be given as an exchange procedure where a patient's blood is simultaneously removed as donor blood is given intravenously, or as a simple transfusion where donor blood products are given without the exchange of the patient's blood. Each type of transfusion procedure is a common treatment method for SCD patients and may be differentially indicated based on presenting clinical sequelae.

Intermittent transfusion therapy has been recognized to prevent or reduce the severity of SCD complications such as stroke¹²⁹, ACS¹³⁰, and an overall reduction in hospitalization rate¹³¹. However, chronic repetitive transfusions ultimately lead to RBC alloimmunization due to imperfect blood type matching between donors and recipients, especially because the majority of blood donors in western countries are of European descent and often express antigens not normally present in SCD patients of African descent¹³². There exist 35 blood grouping systems beyond the classic A/B/O classification, involving over 360 recognized individual blood antigens, many of whose alloantibodies are rapidly undetectable following patients receipt of transfusions^{132,133}. The most common consequences of alloimmunization in SCD patients are donor blood scarcity, transfusion delays, or life-threatening acute or delayed hemolytic transfusion reactions. While great advances have been made to adequately match donors and recipients in order to reduce

alloimmunization rates, it is estimated that more than 58% of SCD patients will eventually become alloimmunized¹⁰².

The purpose of this study is to provide proof-of-concept for a novel potential treatment of SCD wherein the removal of endogenous HbS from SCD patient RBCs is performed and subsequently replaced with exogenous healthy donor Hb. We hypothesized that newly refilled sickle RBCs not containing HbS will lose their ability to sickle and will have improved viscoelastic properties, thus improving their ability to deliver oxygen when re-introduced to patients as an autologous blood transfusion. The use of autologous SCD RBC membranes in this therapy would prevent the possibility of alloimmunization from donor blood transfusions and would provide additional treatment options for patients. To test the viability of this hypothesis, intracellular Hb exchange was performed on human SCD RBCs, and their rheological characteristics analyzed.

4.2 Materials and Methods

4.2.1 Hb Solution Preparation

Hb solutions were prepared by freezing washed and packed bovine RBCs previously anticoagulated in citrate phosphate dextrose-adenine 1 (CPDA-1). After thawing at room temperature, solutions were then diluted to 30% of original solution with sterile water to ensure complete lysis of RBCs. Hb solutions were then brought to a pH of 5.7-5.8 using 0.1 N HCl (approximately 0.1 vols) to encourage precipitation¹³⁴ of red cell stroma. Solutions were centrifuged at 12,500 g for 45 mins and the top stroma-free solution aspirated from the bottom pellet. Solutions were filtered serially using 6 um and 3 um Whatman filter papers (GE Healthcare

Division, Chicago, IL) at a vacuum of 40-60 mmHg, followed by sterilization and purification using a 0.22 μm Steritop™ vacuum filter apparatus (MilliporeSigma, Burlington, MA). Hb solutions were then raised back to a pH of 7.1-7.4 using sodium bicarbonate, and gentamicin Sulfate (100mg/mL, VetOne®, Boise, ID) added at 100 mg/L to prevent bacterial growth. Hb solutions were concentrated using 7k MWCO Snakeskin™ dialysis tubing (Thermo Fisher Scientific, Waltham, MA) on a bed of 35,000 MW polyethylene glycol (PEG) (Sigma-Aldrich, St. Louis, MO) to an approximate concentration of 28-30 g/dL. The entire Hb solution preparation procedure was performed at 0-4 °C to prevent the formation methemoglobin. Hb solutions were used within 1 week of their preparation. Viscoelasticity of Hb solutions was quantified using the Vilastic-3 (Vilastic Inc., Austin, TX).

4.2.2 Intracellular Hb Exchange Protocol

A modified version of the hemoglobin-free ghost RBC protocol^{135,136} was developed for the purpose of this study. Human sickle cell samples anticoagulated in CPDA-1 were obtained following SCD exchange transfusion procedures in accordance with the Institutional Review Board at the University of Pittsburgh. Received SCD blood samples were washed 3x in PBS (w/o Ca^{2+} or Mg^{2+}), their buffy coat removed, and resuspended at $50 \pm 1\%$ Ht in PBS. Briefly, sickle RBC membranes were made permeable in an acidic hypotonic solution to release intracellular HbS, then resealed following incubation in a hypertonic solution of concentrated healthy Hb for “refilling” of the empty membranes. Samples were chilled on ice overnight and then incubated in a water bath at 37 °C for one hour for final resealing of the membranes. These RBCs were then washed 3x at 12,500 g for 30 minutes in PBS. A simplified schematic of the procedure is shown

in Figure 25. For the purpose of control and comparison membranes, experiments also including sickle RBC ‘ghosts’ filled with PBS and intracellular Hb exchange of healthy human RBCs were also performed in parallel to SCD RBC experiments.

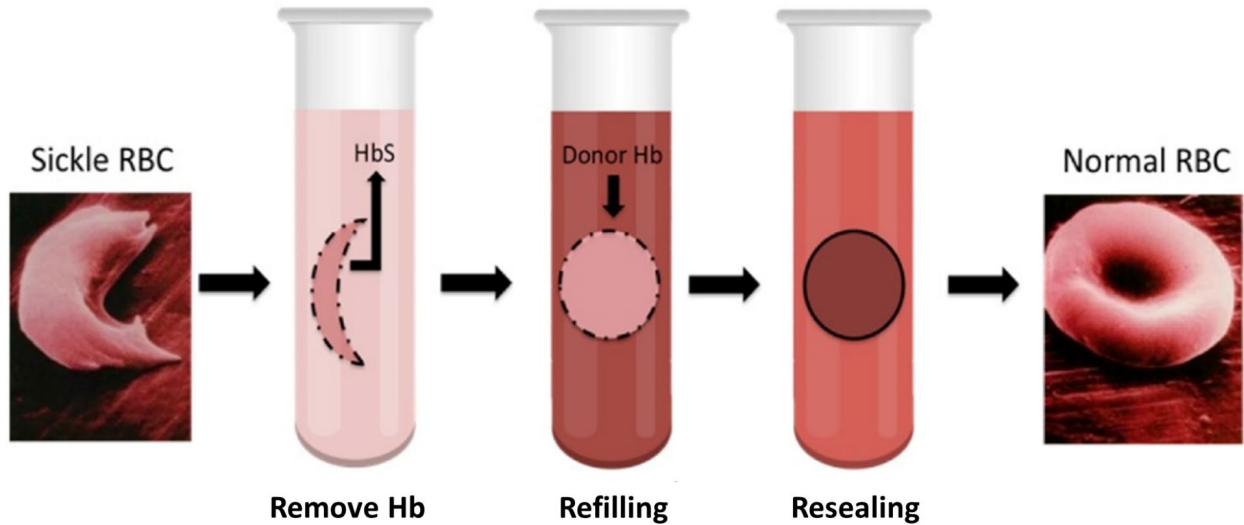


Figure 25. Schematic of the experimental protocol for intracellular Hb replacement.

4.2.3 Rheological Analysis of Modified RBCs

The mean corpuscular Hb concentration (MCHC) was determined using the formula:

$$MCHC [g/dL] = 100 * total Hb [g/dL] / Ht [%] \quad \text{Equation 4.1}$$

where total Hb (tHb) was measured using the OSM3 Hemoximeter (Radiometer Inc., Copenhagen, Denmark) and the Ht measured using heparinized capillary tubes (Sureprep™, Becton Dickinson, Franklin Lakes, NJ). RBCs were imaged using bright-field light microscopy at 40x magnification,

their deformability measured using a Linkam shearing stage (see Appendix A.1), and viscosity determined using the Vilastic-3 viscoelastometer (Vilastic Inc., Austin, TX). Custom miniature hollow fiber membrane channels were also manufactured for the purpose of oxygenation and deoxygenation of small volumes of RBC samples and Hb solutions (Figure 26). Samples were then able to be oxygenated or deoxygenated within an air-tight system using a syringe pump as either pure nitrogen or oxygen gases were passed through the oxygenator. Samples were rapidly deoxygenated to venous saturation or below ($\sim 50\%$ spO_2) in order to induce sickling, and their spO_2 measured using the ABL825 blood gas analyzer (Radiometer, Copenhagen, Denmark).

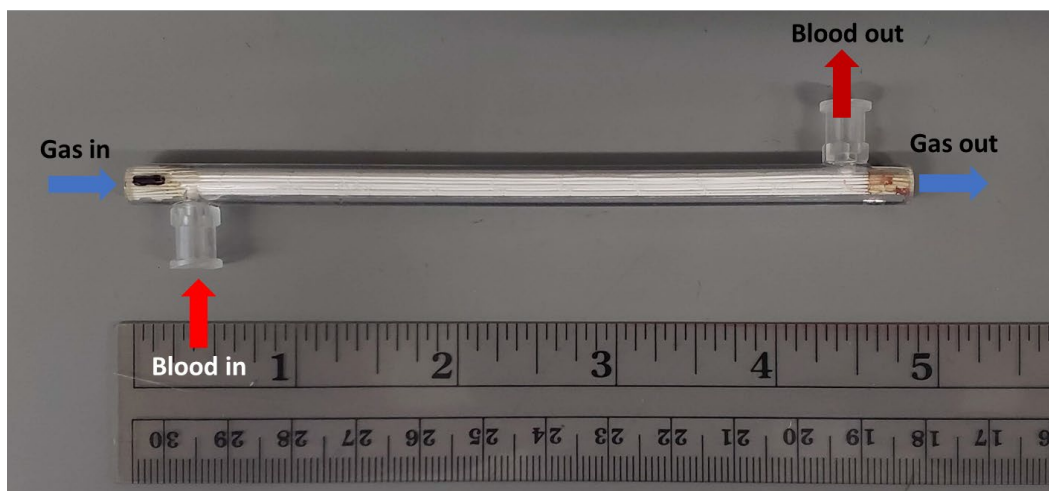


Figure 26. Custom mini hollow fiber membrane oxygenator made with polymethylpentene fibers.

The presence of residual HbS within refilled sickle RBCs was determined qualitatively using the SickScreen Hb solubility assay (Thermo Fisher Scientific, Waltham, MA). SickScreen testing kits use a modified Nalbandian procedure¹³⁷ which identifies the presence of HbS based on the differential solubility of HbS and HbA in a concentrated phosphate solution¹³⁸. Briefly, red cells are lysed in a surfactant, the hemoglobins reduced using sodium hydrosulfite,

after which the HbS proteins (if present) form a turbid suspension in concentrated phosphate solution. Healthy Hb/HbA remain in solution, and test interpretation is performed in a test tube rack with reading lines behind samples. The ability to visualize reading rack lines indicates a negative test (no HbS), while turbid solutions obscure reading lines in the presence of HbS.

4.2.4 Statistical Analysis

Statistical analysis was performed using the two-tailed independent Student's t test, with a value of $p < 0.05$ assumed to indicate statistical significance. Continuous variables presented as mean \pm standard deviation (SD).

4.3 Results

4.3.1 Modified RBC Hemoglobin Content and Morphology

Both ghost and refilled sickle RBCs were successfully made from SCD patient blood samples. Ghost sickle cells were found to be almost completely devoid of all hemoglobin (0.71 ± 0.09 g/dL), with refilled sickle cells containing an average of 7.9 ± 1.5 g/dL MCHC. No statistical significance was found between Hb encapsulation ability of healthy human refilled RBCs and refilled sickle RBCs ($p = 0.8$) (Figure 27). Statistical significance was found between the healthy human ghost RBCs and the sickle ghost RBCs ($p = 0.02$); however, we judged this difference to be acceptable because this quantity of Hb represents less than 2-3% of total cellular

Hb and approached the minimum total Hb testing capabilities of our hemoximeter. Further, this low concentration of native Hb, even if left behind within refilled RBCs, would likely not contribute towards SCD pathology.

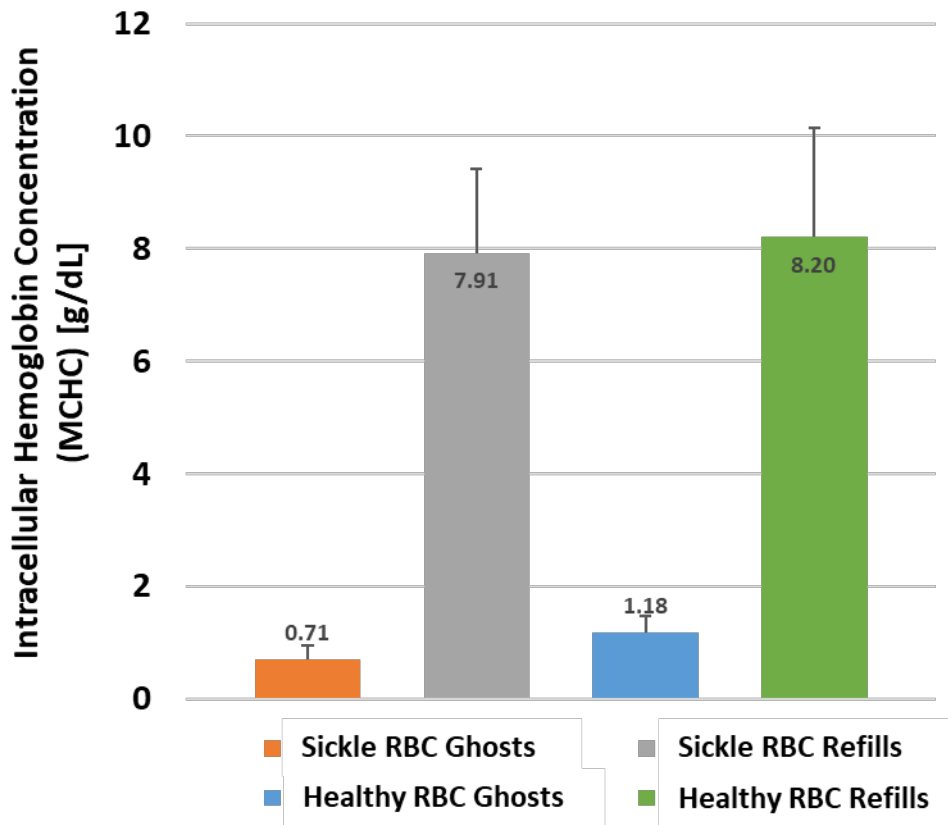


Figure 27. Mean corpuscular Hb concentration (MCHC) [g/dL] of refilled and ghost sickle RBC samples alongside healthy refilled and ghost RBCs created using identical protocols for comparison.

SickleScreen testing was performed according to the included written protocol, and all unmodified SCD blood samples tested positive for the presence of HbS. Both refilled and ghost sickle RBC samples displayed strong negative results, even after doubling the blood sample

volume to account for lower Hb concentrations as indicated by the instruction manual¹³⁸ (Figure 28). Further, when positive and negative SickScreen control samples were analyzed at matching tHb to that of the measured refilled SCD RBCs, the results of the SickScreen negative control closely match that of the refilled SCD RBCs, indicating a lack of intracellular HbS.

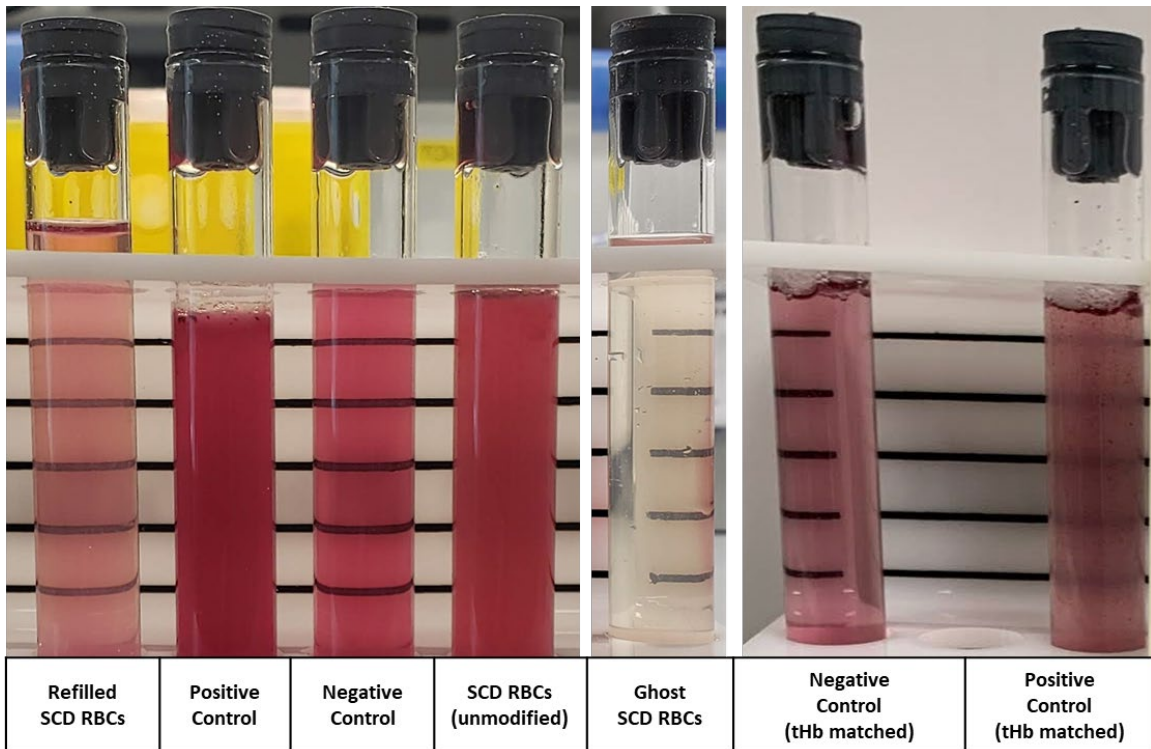


Figure 28. SickScreen testing results. In the presence of HbS, solutions become turbid and reading rack lines will no longer be visible. Positive SickScreen control samples and unmodified sickle RBCs were determined to contain HbS. Both ghost and refilled RBC samples derived from SCD blood were found to no longer contain appreciable HbS following Hb replacement therapy.

Unmodified sickle RBCs imaged under bright-field light microscopy displayed clear signs of sickling in both oxygenated and deoxygenated states. In their oxygenated state, a majority of sickle RBCs were observed as discoid in shape, with approximately a quarter or less of RBCs

observed as sickle in shape, or were distorted with at least one or more spiny membrane protrusion(s) (Figure 29A). Following deoxygenation, unmodified sickle RBCs were nearly all distorted into sickle or oblong shapes, many of which displaying multiple membrane spines (Figure 29B). These spines are most likely due to the rapid deoxygenation of these cells in our gas exchange device, which may have caused the simultaneous formation of multiple intracellular Hb fiber bundles. Refilled sickle RBCs showed no signs of sickling in either oxygenated or deoxygenated states (Figure 29C-D). Ghost sickle RBCs devoid of all Hb were only imaged in an oxygenated state (Figure 29E) and were not tested for their ability to sickle upon deoxygenation due to their lack of intracellular Hb.

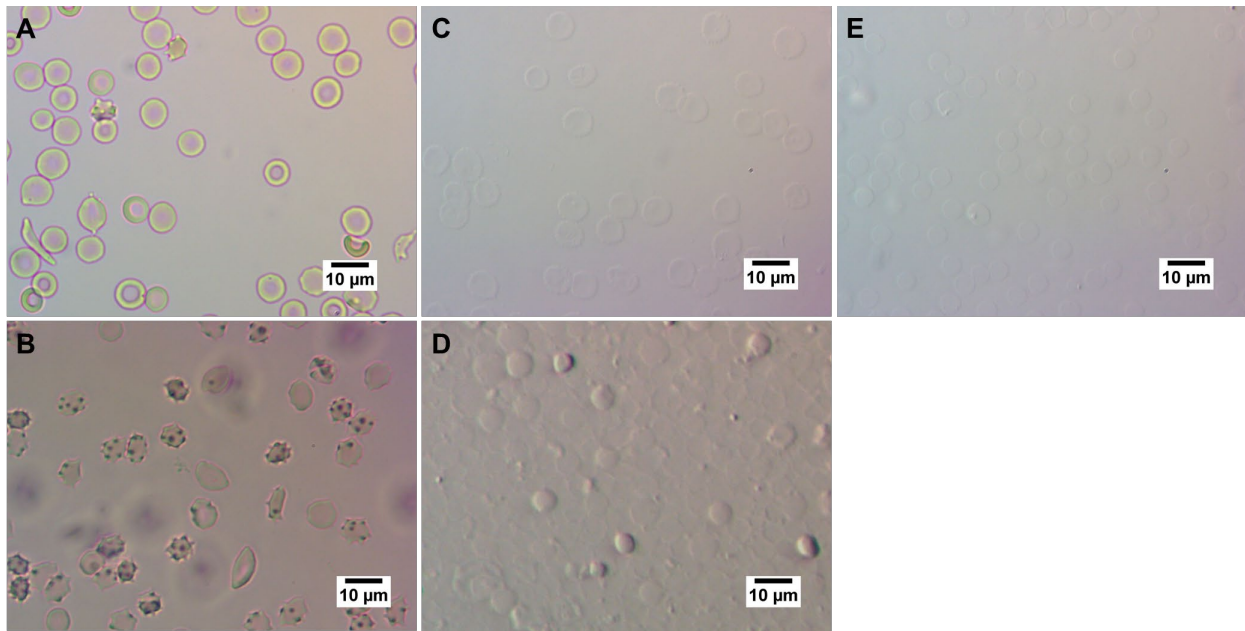


Figure 29. (A) Oxygenated unmodified sickle RBCs, (B) Deoxygenated unmodified sickle RBCs, (C) Oxygenated refilled sickle RBCs, (D) Deoxygenated refilled sickle RBCs, (E) Oxygenated ghost sickle RBCs.

4.3.2 Cell Deformability

Cellular deformability characterized by the dimensionless elongation index (EI) showed healthy human RBCs as the most deformable, and unmodified sickle RBCs as the least deformable. While it was found that all types RBCs derived from sickle blood samples were significantly less deformable than healthy RBCs, there was still a measurable improvement in the deformability of both ghost and refilled RBCs derived from sickle blood samples. A summary of the EI data gathered is depicted in Figure 30.

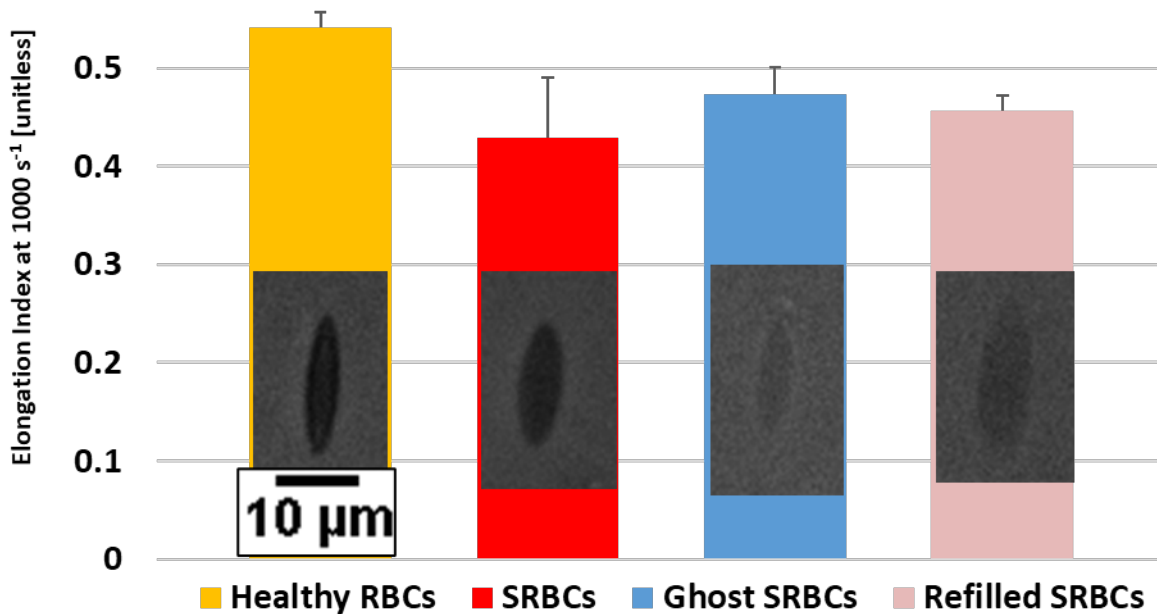


Figure 30. EI of sickle RBCs undergoing intracellular Hb exchange therapy in comparison to healthy human RBCs. Healthy human RBCs (n = 3) were found to have a significantly greater EI than unmodified sickle RBCs (n = 6, p = 0.018), ghost sickle RBCs (n = 6, p = 0.004), and refilled sickle RBCs (n = 5, p < .001). Both refilled and ghost sickle RBCs were not found to have a significantly greater ability to deform than unmodified sickle RBCs following intracellular Hb exchange (p > 0.05). Data represents mean ± SD, scale bar represents 10 μm and applies to all inset images.

4.3.3 Viscoelasticity

The viscoelasticity of donor bovine Hb was measured for the purpose of optimizing donor Hb encapsulation within test membranes. Because the viscosity of Hb rises exponentially with concentration, these measurements were used to identify the maximum concentration of Hb which

can be handled and used in our intracellular Hb replacement therapy (Figure 31). Sample measurement over different shear rate ranges were due to device constraints using viscous test fluids. Elasticity of bovine Hb samples below approximately 30 g/dL were negligible and within the range of signal noise for the Vilastic-3.

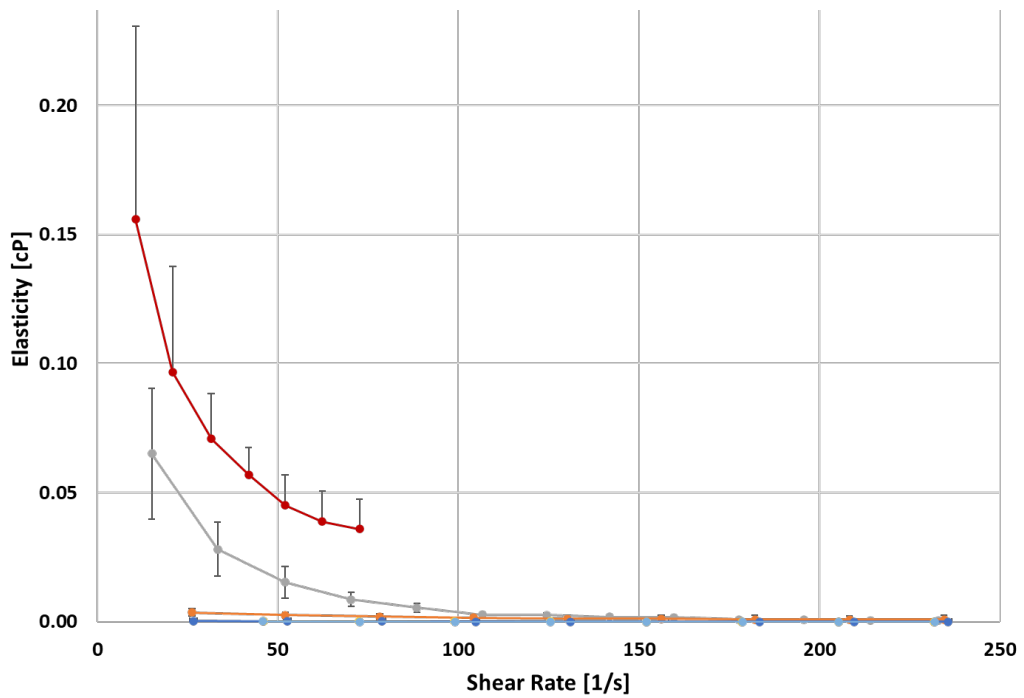
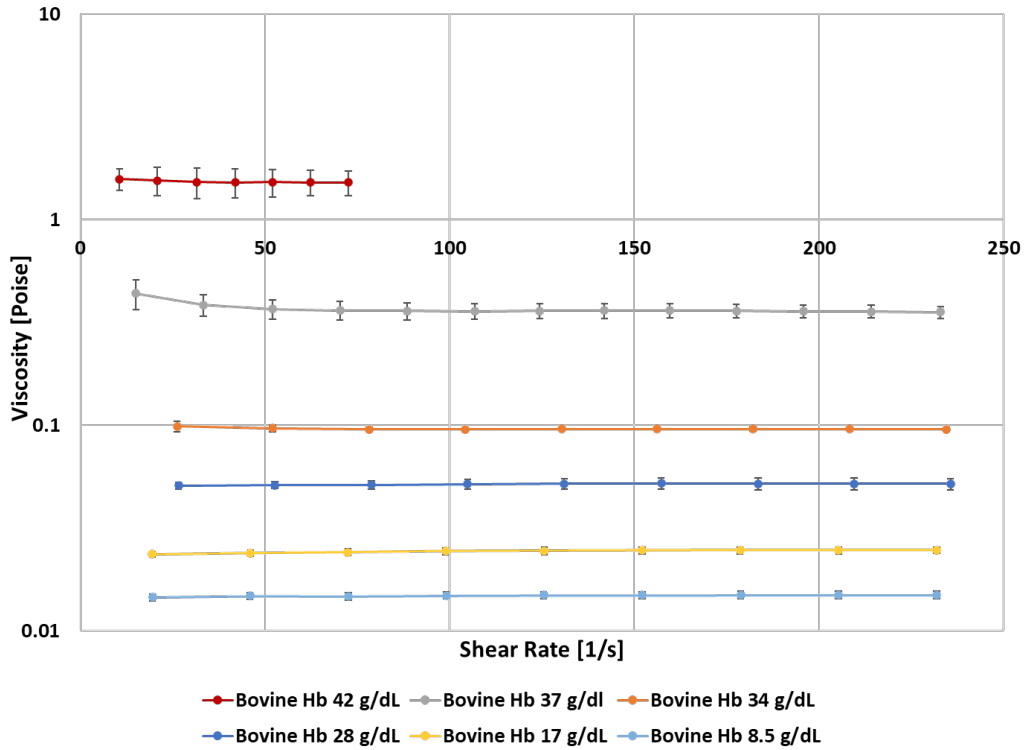


Figure 31. Viscosity (Top) and elasticity (Bottom) of purified bovine hemoglobin at various concentrations. Data presented represents mean \pm SD. Middle figure legend represents both Top and Bottom graphs.

Bovine Hb viscoelasticity was compared to purified and concentrated HbS obtained from SCD patient blood samples for the purpose of identifying intracellular contents before and after Hb exchange. SCD HbS was processed identically to that of bovine Hb. As expected, HbS viscoelasticity was greater than bovine Hb at similar concentrations and increased significantly upon deoxygenation. Sample measurement over different shear rate ranges were due to device constraints using viscous test fluids. Deoxygenated bovine Hb viscoelasticity was not measured due to its known characteristic of constant viscoelasticity regardless of oxygenation status.

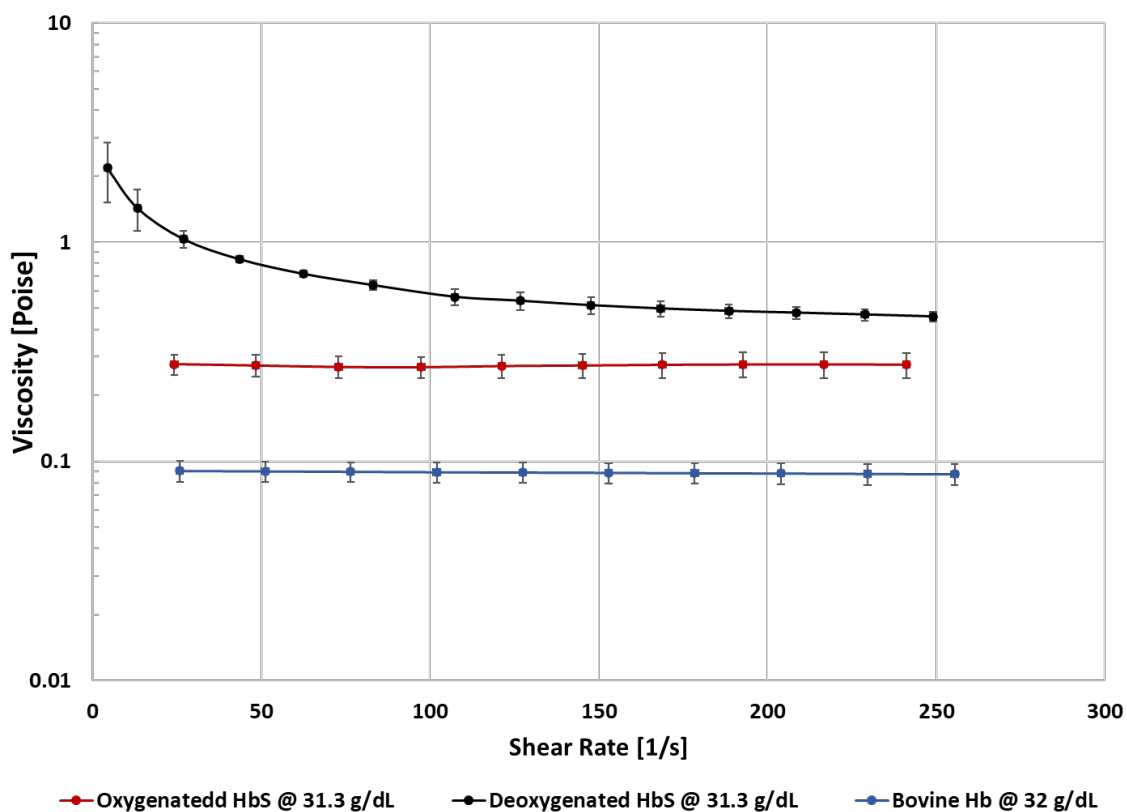


Figure 32. Viscosity (Top) and elasticity (Bottom) of purified and concentrated SCD HbS solution in deoxygenated and oxygenated state. Bovine Hb viscoelasticity also included for comparison. Data presented represents mean \pm SD.

Comparison of viscosity (Figure 33, Top) and elasticity (Figure 33, Bottom) of SCD blood samples undergoing intracellular Hb exchange therapy. Samples were measured at $40 \pm 1\%$ Ht and suspended in an identical suspension fluid (PBS). Measurements were made at 40% Ht for observation of more pronounced non-Newtonian flow behavior. Healthy human blood samples suspended in PBS were also measured under identical conditions for comparison. As expected, deoxygenated unmodified SCD RBCs demonstrated the highest viscosity, greater than of itself in an oxygenated state. Both oxygenated and deoxygenated SCD blood viscosity was up to twice that of healthy blood samples and other modified RBCs. Especially at lower shear rates, SCD blood and deoxygenated SCD blood showed elevated viscosity and elasticity even following washing and suspension in PBS due to the presence of rigid RBCs and increased tendencies to aggregate. Following the intracellular Hb exchange process, samples exhibit a marked decrease in viscoelasticity of modified RBCs, most likely owing to the removal of viscous HbS and its replacement with less viscous donor Hb solution. Ghost modified RBCs derived from SCD patient samples were found to be least viscous of all samples measured, due to the complete removal of all Hb-containing intracellular contents. Following deoxygenation, refilled modified SCD RBCs were found not to increase in viscoelasticity to the same degree of unmodified SCD RBCs due to their lack of sickling HbS. Ghost modified RBCs were unable to be deoxygenated and measured due to their almost complete lack of Hb.

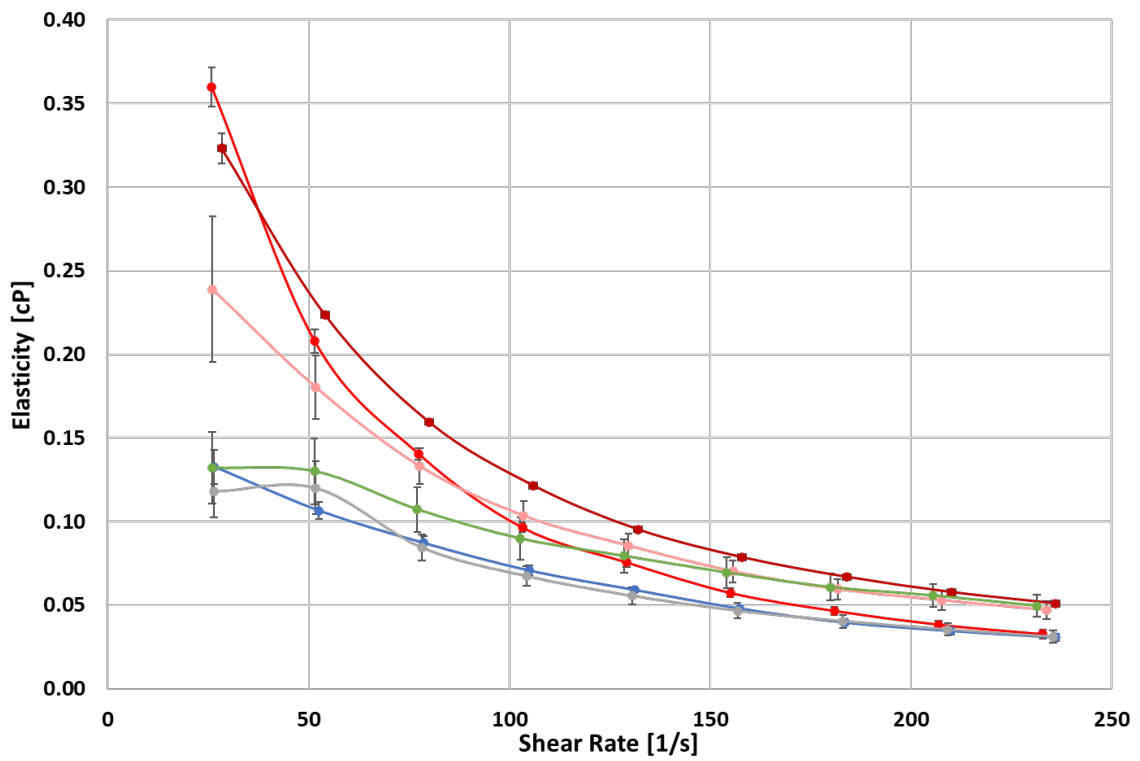
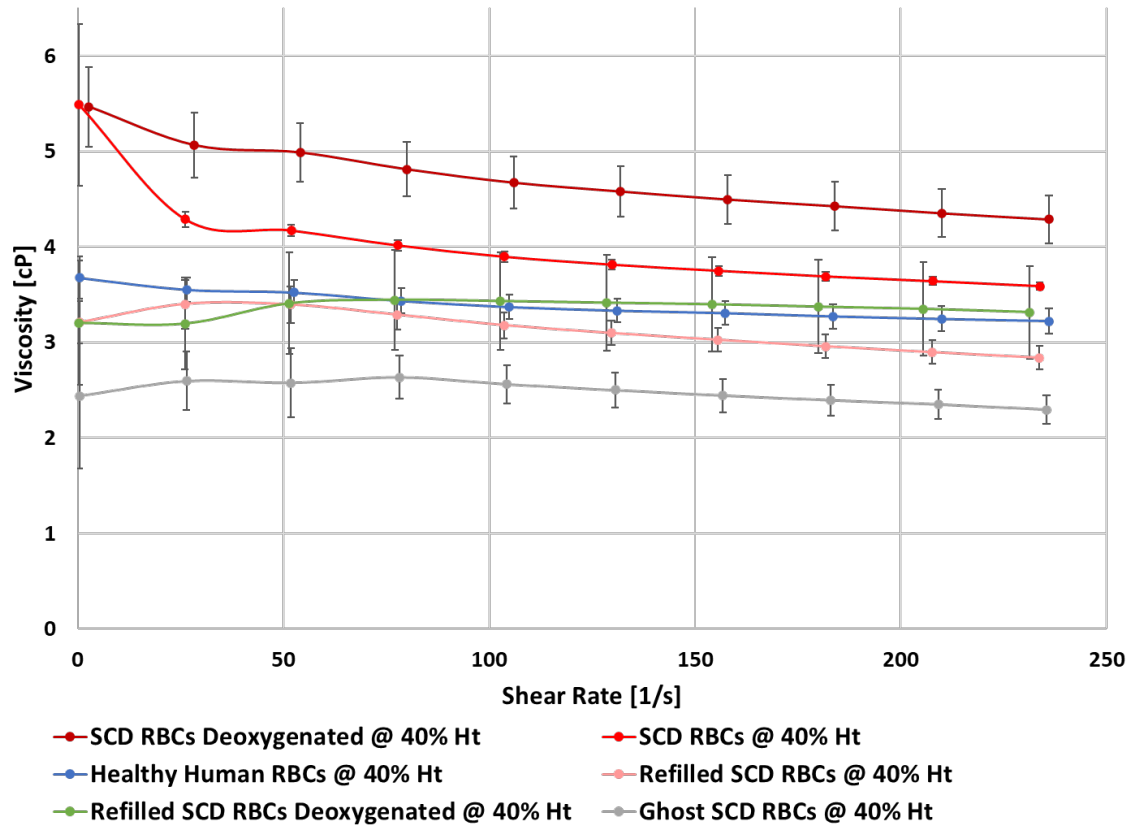


Figure 33. Viscosity (Top) and elasticity (Bottom) of SCD blood samples undergoing intracellular Hb exchange therapy. Middle figure legend represents both Top and Bottom graphs.

Data shown as mean \pm SD.

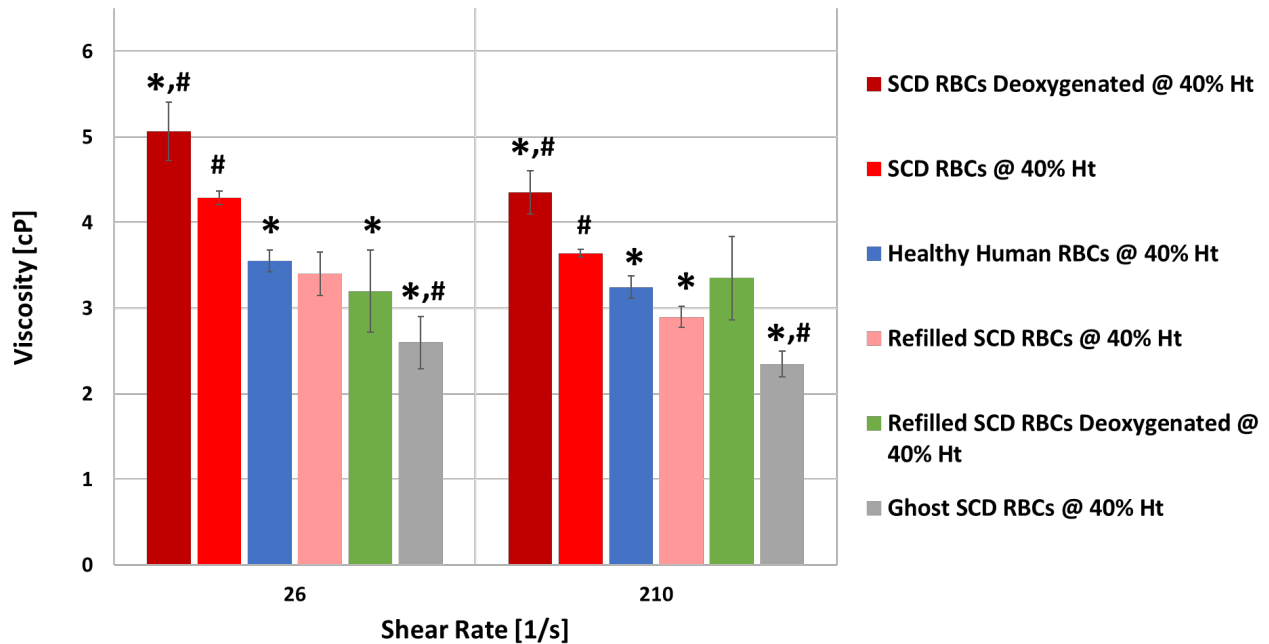


Figure 34. Statistical analysis of viscosity differences at low (26s^{-1}) and high (210 s^{-1}) shear rates. * represents significant statistical difference from SCD RBC samples ($p < 0.05$), and # represents significant statistical difference from healthy human blood samples ($p < 0.05$). Data shown as mean \pm SD.

4.4 Discussion

This work demonstrates the proof-of-concept that SCD patient red blood cells can be emptied and refilled with a donor Hb solution, theoretically allowing for frequent and chronic transfusion without elicitation of immune response. This “intracellular transplantation” process halts the erythrocytic damages that cyclic HbS polymerization and de-polymerization inflicts upon the RBC membrane by replacement of HbS with donor bovine Hb. Bovine Hb is a logical choice

for the testing of this new therapy due its cost and availability, its close similarity to human Hb in regards to both its size and MW (~64,500 Da), and has previously been extensively studied as a potential intravenous oxygen carrier^{139,140}. Unbeknownst at the onset of this work, a single previous study to replace the Hb within sickle RBCs had been performed by researchers with relative success¹⁴¹. However, to our knowledge, our work is the first to perform Hb replacement in SCD RBCs in large enough quantities such that it is possible to also measure the rheological characteristics of modified cell membranes and blood suspensions using our own internally developed intracellular Hb replacement protocol.

The successful removal of HbS and the inability of refilled RBCs to sickle validates our ability to perform intracellular Hb exchange. Although the manner of testing residual HbS contents of sickle RBCs was qualitative, the strong negative results of the SickScreen testing kit show the success of the procedure and do not immediately indicate a need for quantitative testing. Studies to determine the exact proportion of residual HbS and freshly encapsulated donor Hb in refilled RBCs using Hb gel electrophoresis or radiolabeled donor Hb will be planned in future development of this protocol.

EI measurements of RBC deformability following intracellular Hb exchange show that while both refilled and ghost cells derived from sickle RBCs showed a small improvement in their ability to deform, the change was not significant enough to reach the ability to deform to that of the same levels of healthy human RBCs. While this finding does not conform to our hypothesis that intracellular Hb exchange would improve the deformability of cells, it does give insight to the degree of pre-existing cellular membrane damage. Sickle cell RBC membrane damage is inextricably linked to the polymerization of HbS within RBCs and subsequent accelerated RBC aging. This is known to cause membrane abnormalities including ion and water channel

deficiencies, membrane protein defects and dysfunction, and membrane rigidity¹⁴². In the testing paradigm used in this study, cellular deformability is dependent on a combination of both cytoplasmic viscosity and the micro-rheologic mechanical properties of the membrane. However, the measurable increase in deformability of ghost sickle RBCs to refilled sickle RBCs may be explained by differences in the intracellular content. Although undergoing identical protocols, the ghost RBCs refilled with PBS solution displayed greater deformability due to their less viscous contents. Deformability is an important determining factor in RBCs' splenic removal from circulation. It would be valuable to perform more research on these modified RBCs to ensure that these cells would not be prematurely removed from circulation, including comparing modified RBC lifespan to that of sickle RBCs or conducting mechanical fragility testing.

The process of intracellular Hb exchange significantly reduced the viscoelasticity of both refilled and ghost modified sickle RBCs from the level of that of unmodified SCD RBCs towards healthy human RBCs at a matched Ht. This result is attributed to the removal of the viscous intracellular HbS contents of sickle RBCs. Further, the noticeable non-Newtonian viscosity behavior exhibited by both oxygenated and deoxygenated unmodified SCD samples was decreased following intracellular exchange, indicating that elevated viscosity caused by cytoplasmic contents and aggregability was diminished following our protocol. The significant decrease in viscoelasticity of modified SCD RBCs to that of healthy RBCs has implications for the improvement of their flow through the microcirculation. The observed reduction in aggregability and overall viscoelasticity suggest decreased transit time of modified RBCs, while their inability to sickle may also decrease potential blockages within small vessels. These results taken together show that our intracellular Hb exchange procedure may help to maintain improved blood rheology

following transfusion and attenuate the existence of the vicious cycle which perpetuates inflammation and vaso-occlusion in SCD.

This work demonstrates our ability to perform intracellular Hb exchange within RBCs without further damaging or depreciating their existing rheological properties. However, it should be considered a proof-of-concept feasibility study and is not intended for direct translation into animal or human studies. Additional considerations should be met before the use of these cells in live animal subject(s). For example, due to the nature of the process used to create both ghost and refilled RBCs, the action of using hypotonic solutions to permeabilize cell membranes will cause a certain fraction of RBCs to undergo irreversible hemolysis, creating vesicular fragments. While the recovered ghost or refilled cells are extensively washed in a PBS solution, there presumably remains a small amount of these membrane fragments in the final cell suspension. Microparticles, especially those derived from the hemolysis of sickle RBCs which contain heme groups, have been linked to the triggering of vaso-occlusion and the activation of endothelial cells especially in SCD^{143,144}. Future work to develop additional steps to either assess the quantity of these microparticles or to remove or separate them from ghost or refilled cell suspensions should be developed in order to prevent adverse/deleterious reactions from their administration. In addition, although donor Hb encapsulation was demonstrated in this study, the MCHC of refilled cells remains only just above a quarter of the native MCHC of unmodified RBCs (~32 – 34 g/dL). As a transfusion therapy, the goal of this work is to improve the relative percentage of circulating healthy Hb with the least amount of donor modified cells. In order for this, the total donor Hb encapsulation should be maximized as much as possible. In this work, the process of refilling cells with donor Hb is dependent on the concentration gradient between the Hb-rich ‘resealing solution’ and the permeabilized cell membranes. Because the encapsulation of donor Hb relies on its rapid

mixing in solution, the viscosity of ultra-concentrated donor Hb solutions (Figure 31) becomes a limiting factor in the ability to refill cell membranes. A balance between donor Hb viscosity and concentration was made in order to optimize the ability of Hb encapsulation, where a concentration of approximately 28-30 g/dL was found to work the best in our protocol.

Finally, while the therapy outlined above for the refilling of SCD membranes shows great promise, the process used in these experiments may also be useful for basic science research. The ability to determine the properties of the sickle RBC membrane independent of its cytoplasmic contents can be extremely useful for determining information relevant to their rheology and cellular adhesion following the administration of new SCD drug therapies. Further, the same process may also be expanded upon to create autologous RBC membranes encapsulating large quantities of foreign substance cargo for the growing field of RBC drug encapsulation and delivery¹⁴⁵.

4.5 Conclusions

This chapter summarizes the work performed towards creating a novel potential therapy for the treatment of SCD. This therapy utilizes a specialized method for the replacement of intracellular HbS of sickle RBCs based on previous methods used to create Hb-free 'ghost' RBCs. Our results demonstrate that following intracellular Hb exchange, HbS is not found within modified RBCs in appreciable amounts and their ability to sickle is lost, especially following deoxygenation. Deformability results show a measurable but insignificant increase in deformability of modified refilled sickle RBCs, which is most likely due to membrane damage prior to the collection of samples. Viscoelasticity results show a significant decrease in the bulk

viscosity of blood suspensions containing modified refilled sickle RBCs which also no longer increase in viscosity following deoxygenation. Modified 'refilled' sickle RBC sample viscosity was not significantly different than healthy human RBCs at identical concentration. While these proof-of-concept results show promise as a proof-of-concept, further examination is necessary before translation into animal studies.

5.0 Summary

5.1 Conclusions

Although originating from a single point mutation, SCD is a complex and multi-faceted disease, resulting in a number of pathophysiologies generated by the polymerization of HbS within sickle RBCs. Most notably the polymerization of HbS within sickle RBCs results in hemolysis, vaso-occlusion, and the activation of inflammatory pathways⁵⁰. Collectively, these pathophysiologies contribute to the poor rheological characteristics of SCD blood, impacting nearly all organ systems with ischemic injury and resulting in painful VOEs. While drugs such as hydroxyurea, L-glutamine, and voxelotor are approved by FDA for reducing certain complications such as the frequency of VOE, recurrent SCD patient hospitalization rates and the associated economic healthcare burden remain unacceptably high^{65-67,69}. Novel treatments or therapies are sorely needed to adequately combat SCD, where any reduction in the severity or frequency of complications promises to dramatically extend and improve the quality of life for those suffering from SCD.

The ultimate goal of this dissertation is the investigation of two potential therapies for the treatment of SCD: 1) The application of intravenous DRPs and 2) A novel method of intracellular hemoglobin replacement therapy.

In vitro work performed using custom built bifurcating microchannels showcased the ability of nanomolar concentrations of DRPs to significantly alter the traffic patterns of RBCs based on their deformability. Microchannels were first validated for the presence of the plasma skimming effect, as well as the subsequent elimination of the plasma skimming effect following

the addition of DRPs to RBC suspensions. Following their validation, microchannels were perfused with a mixture of healthy and less-deformable RBCs, where the addition of DRP showed a decrease in the proportion of less-deformable RBCs exiting the smaller daughter branch outlet. The results of this study have direct implications for the treatment of SCD, where less-deformable cellular traffic such as sickle RBCs are more likely to occlude smaller vessels and initiate inflammatory pathways or hemolyze.

The effects of intravascular DRP were also observed to reduce the severity of vaso-occlusion in transgenic SCD mice following inflammatory stimulus. Remarkably, the addition of DRP demonstrated a significant reduction in both area of vaso-occlusion and number of vaso-occluded vessels within liver sinusoids. Further, DRP was shown to reduce the number of neutrophil-containing vaso-occlusions. Neutrophil activation and adherence to sickle RBC and endothelial cells are an influential contributor towards obstruction of blood flow and further perpetuation of inflammatory pathways in SCD⁶². The ability of DRP to prevent vaso-occlusion as documented in this *in vivo* study poses tremendous potential as a future rheology-based therapy for the treatment of SCD.

Finally, a proof-of-concept therapy of RBC intracellular Hb replacement was developed and performed on sickle RBCs. The successful removal of HbS was observed in the creation of Hb-free ghost RBCs which were used as control membranes for rheological characterization and testing. Sickle RBCs were then refilled with donor bovine Hb solution, and their rheological characteristics including deformability and viscoelasticity were measured. Refilled sickle RBCs no longer contained HbS, were slightly more deformable than unmodified sickle RBCs, and were significantly less viscous than unmodified RBCs. Intracellular Hb replacement therapy has critical

clinical significance to substitute or replace transfusion therapy for SCD patients which are or may become alloimmunized to exogenous blood transfusion products.

Each of these two potential therapies seek to improve the standards of treatment for SCD patients. DRPs have the potential to be used to improve overall perfusion and reduce the occurrence of vaso-occlusion. Sickle RBCs refilled with donor Hb solution have the potential to be used as an autologous blood transfusion in place of inadequately matched blood transfusions.

5.2 Future Studies

5.2.1 Determine the Effects of DRP on Changes in Rigid Particle Traffic Through Branched Microchannels

The results of Chapter 2 found a significant change in the cellular traffic of less-deformable RBCs through branched microchannels. While this change in traffic can be used to infer similar changes in microchannel traffic of less-deformable cells such as sickle RBCs, neutrophils also play a large role in the precipitation of vaso-occlusion in SCD. Studies of the effects on DRP on neutrophil or rigid neutrophil-sized particle trafficking through bifurcating microchannels would be helpful in elucidating the potential mechanisms DRP may have in reducing microvessel vaso-occlusion. Imaging techniques to visualize cell or particle position and velocity within blood flow would help to gain perspective on flow patterns and allow for investigation of flow through more than one generation of microvessel bifurcations. It is well documented that neutrophil induced vaso-occlusion occurs most frequently in post-capillary venules^{146,147}. Future investigation into

microchannels with venule geometries would help to determine the ability of DRPs to demarginate neutrophil traffic and potentially reduce cellular wall/endothelium interactions.

5.2.2 Attenuation of Neutrophil-Platelet Interactions with DRP

Previously, a whole blood microfluidic imaging approach for the determination of neutrophil-platelet interactions was performed using SCD blood¹⁴⁸. This study used quantitative microfluidic fluorescence microscopy (qMFM) to observe immune cell aggregate formation, interaction, and arrest during physiologic flow at the vessel wall of PDMS microchannels. The replication of this study with the inclusion of DRP under normalized shear stresses would gain valuable insight in the mechanisms with which DRPs may act to prevent the interaction or arrest of platelets and neutrophils *in vivo*.

5.2.3 Expanded Intravital Imaging Work in Transgenic SCD Mice

Intravital observation of the effects of DRP on other ischemically damaged organ systems such as the lungs and spleen would further validate their use as a potential SCD treatment. Additionally, advanced multi-photon imaging techniques to determine the blood velocity and velocity profiles in observed microvessels would help to shed light on the effects of DRP's intravascular rheological changes as well as any changes in capillary recruitment or perfusion following an inflammatory stimulus. Although it was not attempted in this work, scanning slices of the of the microvasculature through the z-axis (depth) using multi-photon instrumentation would enable the 3-dimensional reconstruction of vessel beds. Because of the innate tortuosity of microvessels, the 2-dimensional images captured in this aim were inherently intersected by vessels

traveling either into or out of the field of view. While the cessation of flow in these intersecting vessels was still able to be clearly identified, this 3-dimensional imaging technique may give a better picture of the degree and size of vaso-occlusion found in mice from between groups studied. Finally, quantification of the levels of inflammatory signaling molecules and markers presented in SCD mice after administration of DRP would serve to highlight any reduction in inflammation, and would be especially helpful in determining the benefits of DRP in attenuating IR/I caused by vaso-occlusion.

5.2.4 Intracellular Hb Replacement Future Studies

Future studies and steps to further validate the feasibility and efficacy of intracellular Hb replacement therapy should be conducted prior to their use in animal testing. The first step of permeabilizing the RBC membrane to remove sickle Hb likely causes some degree of vesicular fragmentation. Membrane fragmentation and the release of free hemoglobin groups have been previously identified to exacerbate inflammatory pathways in SCD patients⁵⁰. Plasma free heme and microparticle detection should be performed to ensure refilled RBCs would not cause initiation of inflammatory pathways. If microparticles were found to be present in refilled RBCs, increased washing or density dependent separation protocols should be developed to reduce risk of adverse effects. Further, both the membrane and cytoskeletal integrity of these newly refilled red cell must be explored. Due to known membrane damage via sickling-dependent mechanics, the refilled cells must be further analyzed to answer questions such as the occurrence or degree of membrane flipping and preservation of the spectrin network during the Hb replacement process using electron microscopy, and must also include study of the changes in aggregation and adhesion in refilled RBCs as compared to their original unmodified sickle membranes. The answers to these studies

would help to determine the viability of our Hb exchange process as a novel technique for the treatment of SCD in its ability to deter or prevent vaso-occlusion *in vivo*.

Studies of cellular mechanical fragility to determine the potential circulating lifespan of refilled sickle RBCs should also be performed, however, due to previously documented decrease in mechanical fragility of hemoglobin-free ghost RBCs¹⁴², favorable mechanical fragility properties seem unlikely using the membranes of prior-damaged SCD RBCs. In addition, these studies should be repeated using donor human hemoglobin to determine if the size of bovine versus human hemoglobins effect the refilling process, however due to their close molecular weight (Bovine: ~64,500 Da, Human: ~64,00 Da) we do not expect this to become a major obstacle. Finally, future studies should be carried out specifically using donor human Hb of mis-matched blood type(s) to conclusively determine if the donor Hb causes a reaction to the host receiving refilled RBCs in terms of aggregation (*ex vivo*) and inflammatory activation and vaso-occlusion (*in vivo*).

Appendix A Drag-reducing Polymers Improve Oxygen Transfer Rate in Miniature Hollow Fiber Membrane Oxygenators

The work described in this section was presented in part at the ASAIO 65th Annual Meeting in San Francisco, CA¹⁴⁹.

Appendix A.1 Introduction

Hollow fiber membrane oxygenators (HFMOs) are medical devices used to supplant the function of the lungs during cardiopulmonary bypass or may be used over the period of a few days to weeks in the form of extracorporeal membrane oxygenation (ECMO) to treat acute respiratory failure (ARF). Despite sharing an identical purpose, few comparisons can be made between the natural lungs and membrane oxygenators, either in their geometries or ability to provide gas exchange. In the lung, alveolar gas exchange to capillaries occurs between the alveolus and capillary cell membranes at a distance of just less than 1 μm over an area of 140 m^2 for a gas exchange capability of 200 mL/min (resting) to over 3200 mL/min during exercise¹⁵⁰. Alternatively, modern hollow fiber membrane oxygenators (HFMOs) have a membrane thickness through which gas exchange occurs of 10 – 50 μm , a maximal total surface area of around 4 m^2 , and gas exchange capabilities of approximately 200 – 400 mL/min even when provided with a supply of pure oxygen.

HFMOs achieve gas exchange via diffusion across small semi-permeable hollow fibers from which gas species may either enter (O_2) or exit (CO_2) blood down their respective

concentration gradients. Typical HFMOs are configured such that intraluminal sweep gas flows within bundles of hollow fibers, with extraluminal blood flow flowing around and past the bundle fibers. Device gas exchange is directly proportional to membrane permeability and surface area, however, the inherent thrombogenicity of large areas of blood contacting materials within HFMOs is a limiting factor towards device size and overall gas exchange capabilities. Thrombogenicity-related complications resulting in device failure or events requiring device swap/exchange such as thrombosis or worsening gas exchange over time are frequent^{151,152}, and result in an unacceptably high need for device swap at least once in up to 28% of ECMO cases¹⁵². Further, the necessary use of anticoagulation therapy to prevent thrombotic complications often cause device-related coagulation disorders (39% of cases¹⁵²) which result in frequent bleeding events. High mortality rates and accompanying high risk of complications associated with the use of membrane oxygenators highlights the need for novel methods to alleviate risks, increase successful outcomes, and improve patient care.

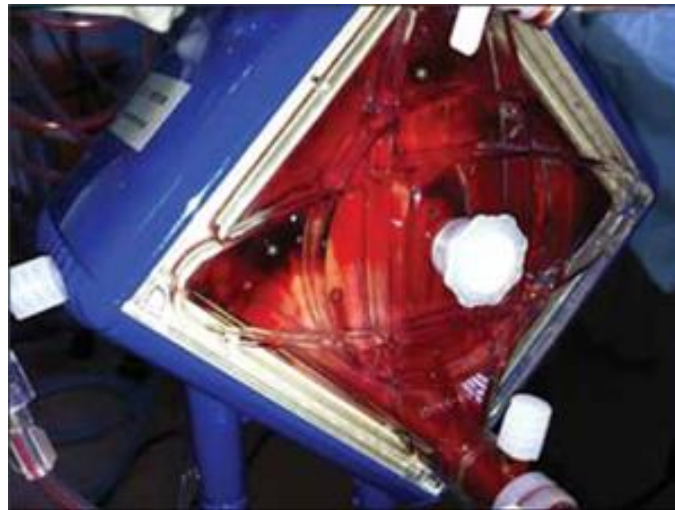


Figure 35. Thrombus formation found within ECMO artificial lung device requiring device exchange. Image used with permission from Parlar et al ¹⁵³.

HFMOs are designed such that gas transfer is maximized while minimizing device surface area. This is often achieved through a combination of active and passive mixing techniques aimed towards creating blood flow paths where the diffusional boundary layer is reduced in order to increase gas permeance and overall transfer efficiency. Previously, non-toxic blood additives known as drag reducing polymers (DRPs) have shown *in vitro* and *in vivo* to reduce the size of stagnant zones at bifurcation regions⁸⁰, eliminate regions of recirculation following microchannel expansions⁹⁷, and reduce of the size of the near-wall “cell-free” layer (CFL) within the microvasculature and microchannels^{19,97}. This study aims to test our hypothesis that the addition of DRPs will reduce small areas of flow separation and/or recirculation within the fiber bundle of a miniature HFMO and increase gas transfer efficiency.

Appendix A.2 Materials and Methods

Appendix A.2.1 Miniature HFMO Experiments with DRP

Bovine blood anticoagulated in K₂EDTA was washed in PBS and suspended at $30 \pm 1\%$ Ht in a PBS solution with 1% BSA. Blood suspensions were deoxygenated to venous conditions using a custom polymethylpentene miniature HFMO using a syringe pump (PhD Ultra Syringe Pump, Harvard Apparatus, Holliston, PA) using a blend of N₂, CO₂, and O₂ for a final oxygen saturation of $65 \pm 5\%$ with a pCO₂ of 45 ± 5 mmHg. Once conditioned, blood was split into two pools, one receiving the DRP PEO at a final concentration of 5 ppm, and the other receiving an equal volume of the saline vehicle. Blood was then pumped through the same miniature HFMO at a rate of 45 mL/min with sweep gas of pure O₂ flowing at a rate of 300 mL/min measured with a

GR Series mass flow controller (Fathom Technologies, Georgetown, TX). Blood samples taken from the inlet and outlet of the oxygenator device were used to calculate oxygen gas transfer rates using a Rapid Point 405 Blood Gas Analyzer with Co-oximetry (Siemens Healthcare Diagnostics Inc., Tarrytown, NY) to measure blood gases and oxygen saturation. An example of the experimental setup used in all miniature HFMO experiments is pictured in Figure 36.

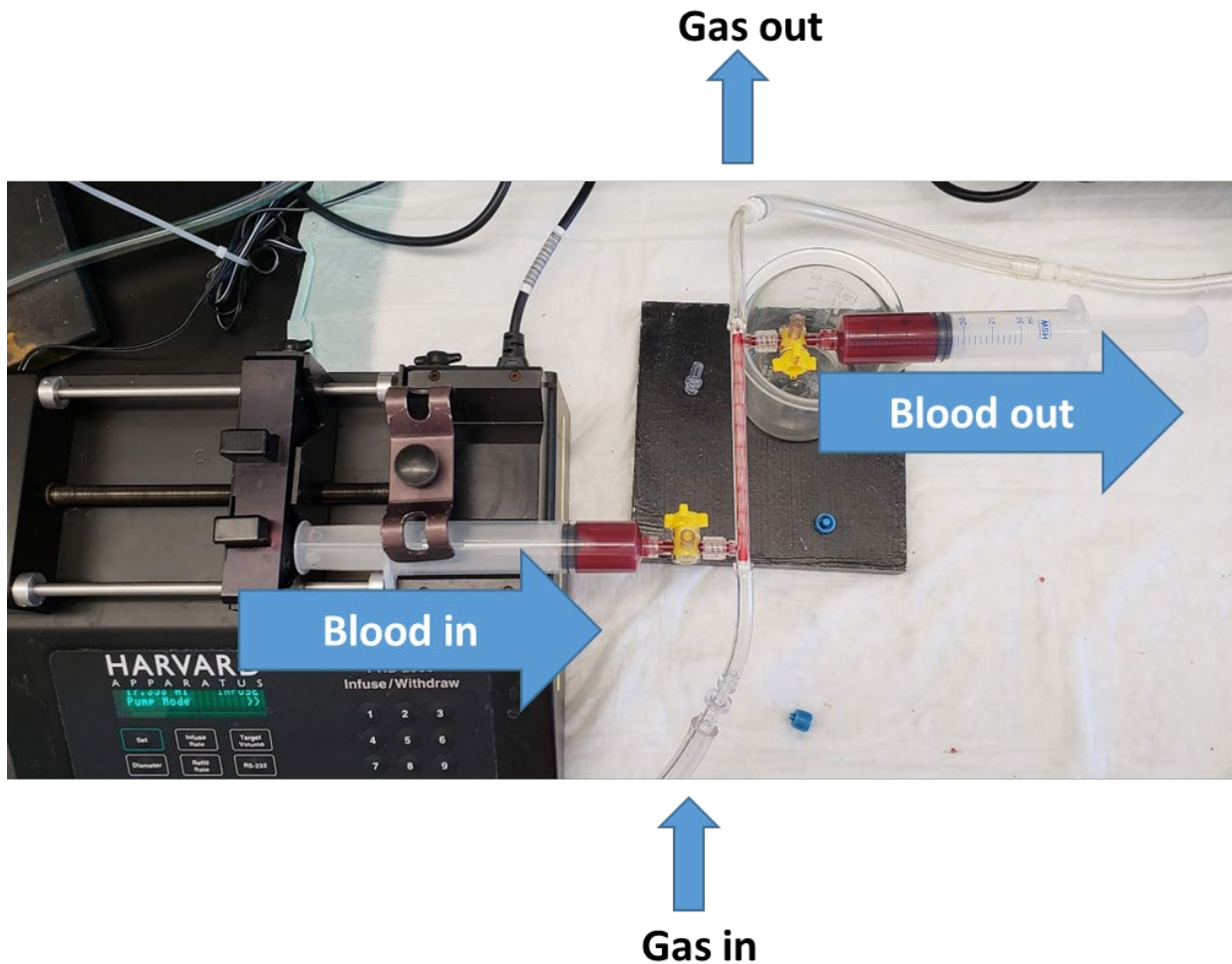


Figure 36. Experimental setup used for the deoxygenation and oxygenation of both blood and Hb solutions using our custom made miniature HFMO device.

Purified Hb solutions were prepared by lysing washed, packed bovine in sterile water to a final concentration of 10 g/dL. Solutions were then centrifuged at 12,500 g for 45 mins and the top stroma-free solution aspirated from the bottom pellet. Solutions were filtered serially using 6 um and 3 um vacuum filters, and antibacterial (Gentamicin Sulfate 100mg/mL, VetOne®, Boise, ID) added at 100mg/L. The entire Hb solution preparation procedure was performed at 0-4°C to prevent the formation methemoglobin. Hb solutions were used within 1 week of their preparation. Bovine Hb solutions were treated identically to bovine blood suspensions and deoxygenated to venous conditions for a final oxygen saturation of $65 \pm 5\%$ with a pCO_2 of 45 ± 5 mmHg. Once deoxygenated, Hb solution was split into two pools, one receiving the DRP PEO at a final concentration of 5 ppm, and the other receiving an equal volume of the saline vehicle. Hb solutions were then pumped through the same miniature HFMO at a rate of 45 mL/min with sweep gas of pure O₂ flowing at a rate of 300 mL/min. Blood gas and oxygen concentration measurements were made in an identical manner to that of the blood experiments.

Oxygen transfer rate across the miniature HFMO was calculated using the formula:

$$\dot{V}_{O_2} = Q * (\alpha_{O_2} * \Delta P_{O_2} + C_T * \Delta S_{O_2}) \quad \text{Equation B.1}$$

where \dot{V}_{O_2} is the oxygen exchange rate, Q is the blood flow rate, α_{O_2} is the oxygen solubility in blood ($3e-5$ mL O₂ / mL Blood * mmHg), ΔP_{O_2} is the partial pressure difference of O₂ across the device, C_T is the binding capacity (0.167 mL O₂ / mL blood), and ΔS_{O_2} is the oxygen saturation difference across the device.

Appendix A.3 Results

Appendix A.3.1 Miniature HFMO Experiments with DRP

Results of the oxygen transfer rate using blood are shown in Figure 37. The addition of 5 ppm of the DRP PEO significantly increased the oxygen transfer rate of the miniature HFMO from 1.51 ± 0.15 mL/min to 1.81 ± 0.12 mL/min, representing a 20% increase in the overall efficiency of the device (Control n = 4, DRP n = 5, p = 0.02).

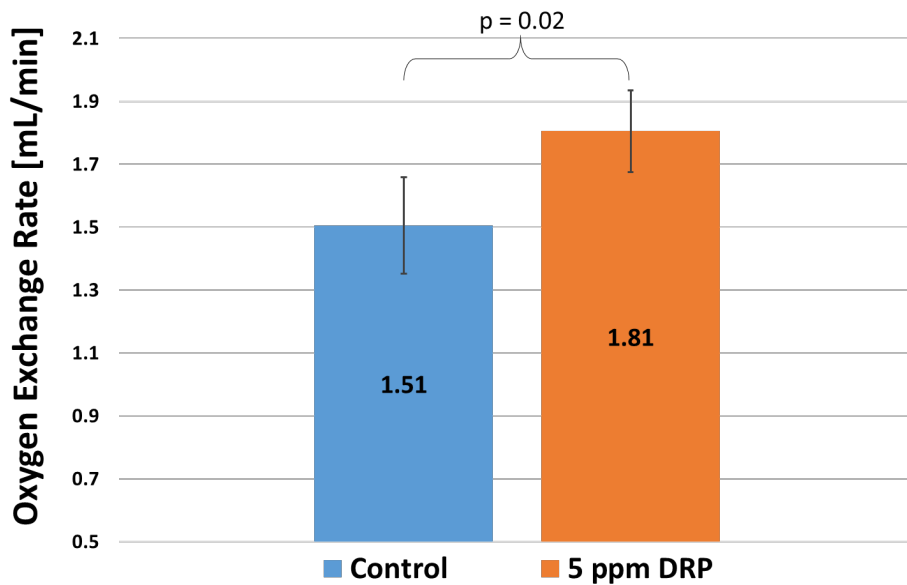


Figure 37. Oxygen exchange rate across the miniature HFMO with bovine blood. Results represent mean \pm SD.

Results of the oxygen transfer rate within the miniature HFMO using Hb solutions are shown in Figure 38. The addition of 5 ppm of the DRP PEO was not shown to significantly alter the oxygen transfer rate within the miniature HFMO. Control experiments showed an oxygen transfer rate of 1.71 ± 0.09 mL/min and 1.67 ± 0.10 mL/mL with the addition of 5 ppm of the DRP PEO (Control n = 5, DRP n = 6, p = 0.54).

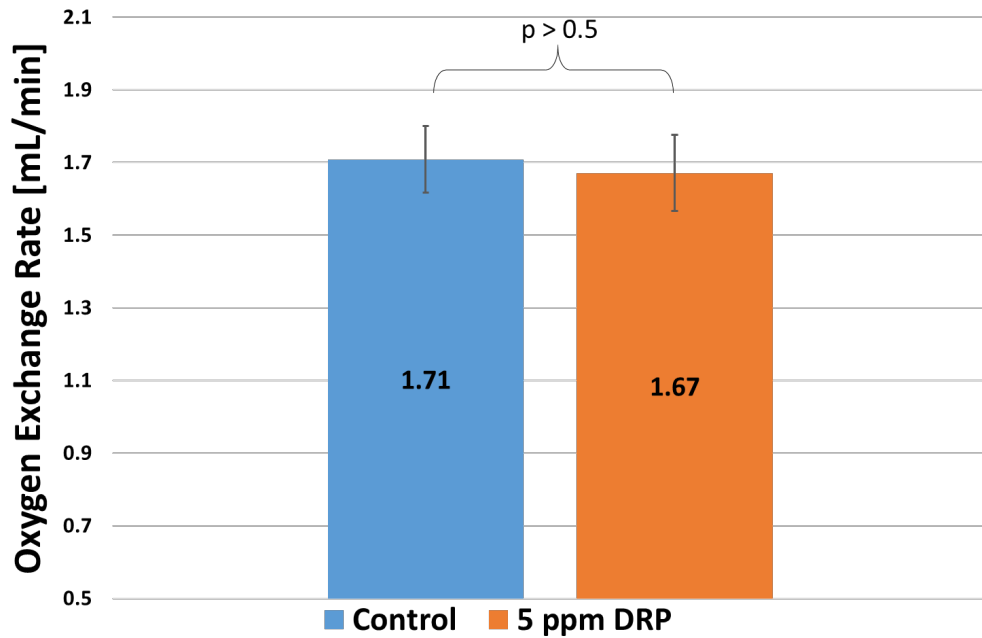


Figure 38. Oxygen exchange rate across the miniature HFMO with bovine Hb solution. Results represent mean \pm SD.

Appendix A.4 Discussion

Membrane oxygenators provide a necessary and life-saving technology for those suffering from ARF, however the high risk of complications represent an area which can be improved. To help address this problem, our group investigated the addition of DRP to increase the oxygen transfer capabilities of a miniature HFMO. It is not currently practical or feasible to increase the efficiency of gas exchange within membrane oxygenators by drastically increasing the surface area or decreasing membrane thickness without undesirable consequences. Therefore, the aim of this work was to increase the gas exchange efficiency in an existing oxygenator by altering the blood flow within them rather than the oxygenator itself. *In vitro* testing demonstrated that the addition of nanomolar concentrations of DRP to blood significantly improved the gas transfer efficiency compared to paired blood suspensions receiving the same volume of saline and run through the same device. We hypothesized that this result was due to the DRP-induced reduction in small regions of flow separation within the fiber bundle, as well as the reduction of the near-wall CFL, causing more RBCs to flow closer to the fiber bundle and increasing device efficiency. A visual schematic of this theory is pictured in Figure 39.

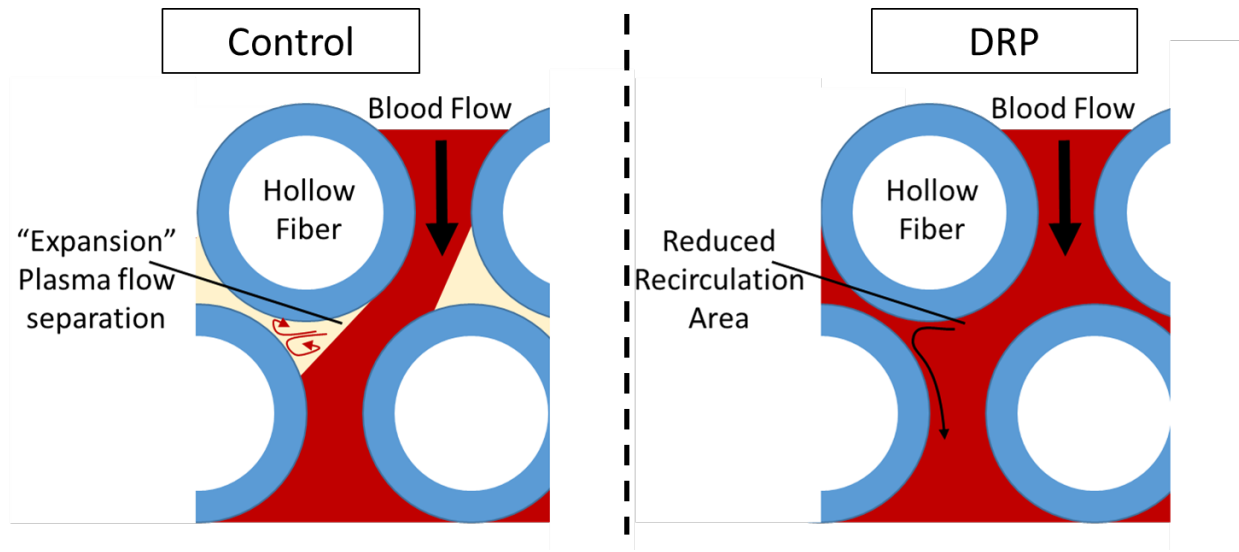


Figure 39. Schematic of proposed possible mechanism for improved gas transfer performance of HFMOs with DRPs. Following the introduction of DRPS within the HFMO device, recirculation and stagnant zones are eliminated or diminished, allowing for improved blood mixing and movement of RBCs closer to fiber membranes.

While this study was not able to visualize these effects within the fiber bundle, our hypothesis is supported by previous theoretical studies which show that hemoglobin saturation increases faster and peaks at higher levels as the CFL is reduced within membrane oxygenators¹⁵⁴. Our hypothesis is further supported with the accompanying results showing that the addition of the same concentration of DRP did not statistically influence the oxygen exchange rate using Hb solutions of similar total Hb concentration. Since the homogeneous cell-free Hb solution would not produce a marginalized CFL or experience plasma flow separation, the addition of DRP would not affect gas exchange rates. Therefore, the increased device efficiency using DRP is likely related to the altered flow patterns of RBCs within the fiber bundle and the movement of RBCs closer to the membrane fibers.

Increased gas transfer efficiency has the potential to reduce the total surface area required in oxygenators, enabling the use of smaller devices. Reduced blood-contacting membrane surface area would in turn reduce the risk of thrombogenesis, requiring less anticoagulation and antiplatelet drugs, further contributing to decreased complications by reducing bleeding and coagulation disorder risks. Additionally, the potential for improved blood washing of stagnant zones within the oxygenator device has the potential to further improve device thrombogenicity without compromising device design or efficiency.

Appendix A.5 Conclusions

Nanomolar concentrations of DRPs significantly increased the oxygen transfer rate within a miniature HFMO device by up to 20%. The results of this study suggest that altered flow patterns of RBCs closer to the fiber bundle and improved circulation of blood flow through the device may explain the increase in device efficiency. The use of DRPs to increase oxygen exchange in HFMOs could potentially allow for the use of smaller oxygenator devices and/or lower anticoagulation requirements to significantly reduce complications during therapy.

Appendix B Supplementary Methods

The following expanded protocols and methods were used in the course of this work:

Appendix B.1 Logistic Regression Algorithm

Logistic regression is a method of classifying data in discrete rather than continuous outcomes (e.g. True/False, Yes/No). This algorithm was applied to identify healthy vs. less-deformable RBCs using the height and width measurements of RBCs collected using the Linkam CSS450 shearing stage (Linkam Scientific, Tadworth, UK).

This algorithm uses a hypothesis, h_{θ} , which is represented by a sigmoid function (also known as a logistic function), g , to map the probability that a given input array, x , either predicts a data point to be one class or the other.

$$h_{\theta}(x) = g(\theta^T x) \quad \text{Equation B.1}$$

$$g(z) = \frac{1}{1 + e^{-z}} \quad \text{Equation B.2}$$

In this example, the input array ‘ x ’ contains the height and width parameters of individually measured RBCs, and θ^T values represent the parameters of a decision boundary line drawn separating the two classification groups (healthy vs. less-deformable) in two-dimensional space. A cost function, J , (Equation A.4) was used to determine the error of the drawn decision boundary line. The error of the cost function was minimized using a method of gradient descent (Equation

A.5) which minimized the classification error between the two groups and improved the accuracy of the logistic regression algorithm.

$$J(\theta) = \frac{1}{m} \sum_{i=1}^m [-y^{(i)} \log(h_{\theta}(x^{(i)})) - (1 - y^{(i)}) \log(1 - h_{\theta}(x^{(i)}))] \quad \text{Equation B.3}$$

$$\frac{\partial J(\theta)}{\partial \theta_j} = \frac{1}{m} \sum_{i=1}^m [h_{\theta}(x^{(i)}) - y^{(i)}] x_j^{(i)} \quad \text{Equation B.4}$$

In practical terms, RBC height and width measurements from samples containing exclusively healthy or less-deformable RBCs were plotted as cell length vs. cell width (Figure 40). Using this data, a decision boundary line or gate was drawn between the two groups of data. The slope and position of the decision boundary line was optimized to minimize the error found when separating the two binary classifications (normal vs. less-deformable RBCs) using the logistic regression algorithm.

Using this decision boundary, the classification of unknown RBC mixtures derived from the same blood source as the training data could then be determined using their height and width measurements based on their position above (normal) or below (less-deformable) the decision boundary gate. A graphical interpretation of the algorithm is shown in Figure 40. The accuracy of the algorithm classifying cells as either healthy or less-deformable using training data was found to be > 99%.

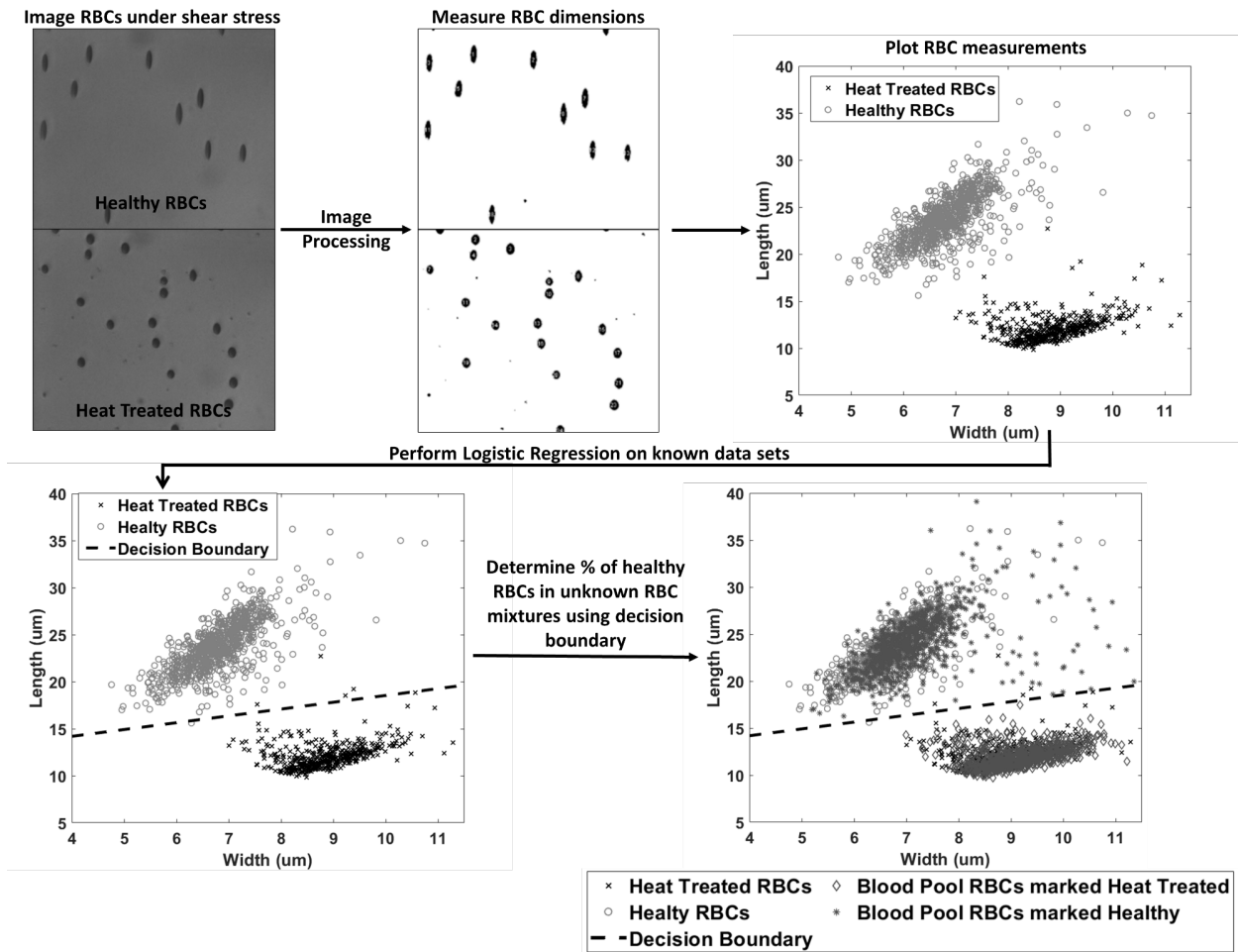


Figure 40. Flowchart of logistic regression algorithm. Healthy and less-deformable RBC length and width measurements are collected and plotted separately, with each point representing the measurements of a single RBC. A decision boundary gate is then created using a logistic regression algorithm, classifying points above the boundary as ‘healthy’ and below the boundary as ‘less-deformable. Following validation, the percentage of healthy or less-deformable heat treated RBCs can be identified from sample mixtures containing unknown percentages of each.

Appendix B.2 Viscoelastometry Methods

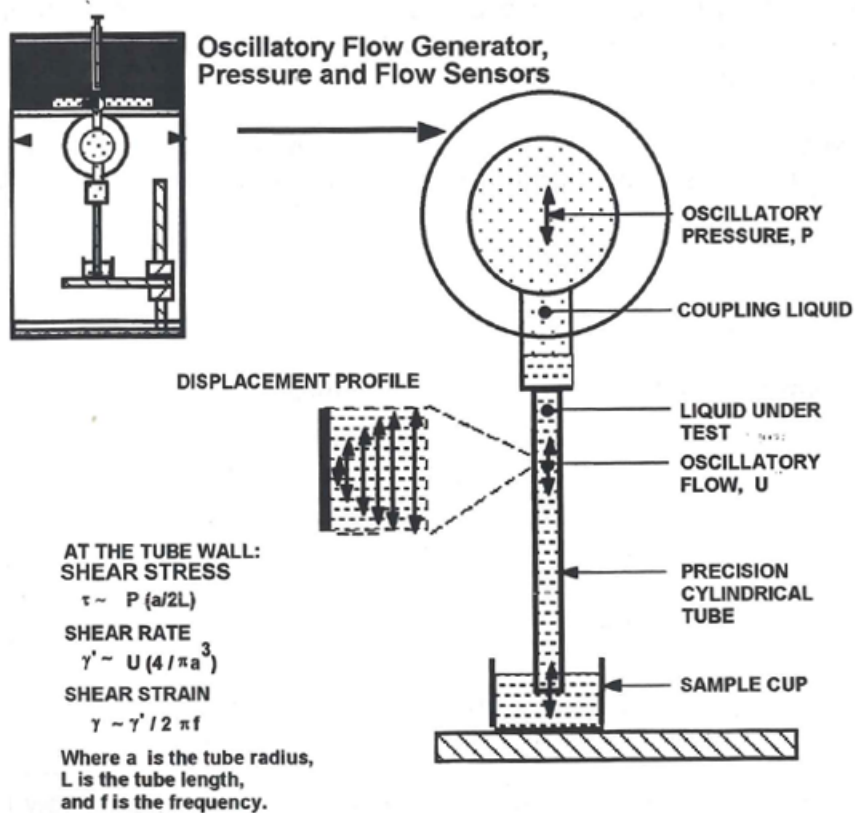
Viscosity and elasticity measurements were performed using the Vilastic-3 viscoelastometer (Vilastic Inc., Austin, TX). The Vilastic-3 is a viscoelasticity analyzer with high sensitivity capable to performing precise measurements of viscosity and elasticity of biologic and non-biologic fluids over a wide range of shear rates. The Vilastic system operates on the fundamental principle of oscillatory flow within a straight tube containing a sample to be measured. A membrane above the sample tube forces the fluid within the measurement tube into oscillatory flow, and the pressure gradient and flow through the tube are measured. The shear stress at the tube wall is directly proportional to the pressure generated, and the shear strain and shear rate are directly proportional to the volume flow measured, enabling accurate measurement of viscosity and elasticity. A schematic of the principle of measurement is pictured in Figure 41.

Prior to data collection, the Vilastic-3 instrument was calibrated and verified to be free of air bubbles using saline. Samples were loaded into a stainless-steel capillary tube measuring 6.18 cm in length and having an inner radius of 0.512 mm. Approximately 0.75 mL of sample test fluid was aspirated into the measurement tube. After the first sample was loaded, a sample evaluation was run to determine the possible shear rate range(s) capable of being measured. The sample was then discarded, the coupling reservoir and measurement tube emptied and rinsed 3x with DI water, and filled again with saline solution. Another sample of testing fluid was then loaded and the desired shear rate range protocol run. Depending on the allowable shear rate range as determined by the sample evaluation, RBC suspensions were run at approximately 25 to 250 s^{-1} in increments of 20 s^{-1} . More viscous hemoglobin solutions generally had shorter shear rate testing ranges and were measured through their max possible range. Oscillatory flow was set at a frequency of 2 Hz

for all measurements collected, which was chosen as a representative of the frequency range of blood flow within the human body.

VILASTIC 3 PRINCIPLE OF MEASUREMENT

Oscillatory flow is generated at a selected frequency in a precision measurement tube. Sensors monitor the pressure "P" and volume flow "U" at the entrance to the tube. Precise resolution of magnitude and phase of the pressure and volume flow allows calculation of the viscous and elastic components of the shear stress, shear rate, and shear strain at the tube wall. From these values the viscosity and elasticity (or storage and loss moduli) are obtained.



[G. B. Thurston, J. Acoustical Soc. Amer. 32, 210 (1960)]
[G. B. Thurston, Biorheology 13, 191 (1976)]

Figure 41. Schematic of the Vilastic-3 viscoelastometer principle of measurement.

Appendix C Programming Code and Scripts

The following appendix sections include ImageJ macro and MATLAB function files used to perform RBC identification, measurement, and execute the logistic regression algorithm used in Chapter 2.

Appendix C.1 ImageJ Macro for Initial Image Processing and Particle Identification

```
>input = getDirectory("image");  
>setBatchMode(true);  
>list = getFileList(input);  
>for (i = 0; i < list.length; i++) {  
>>setAutoThreshold("Default");  
>run("Analyze Particles...", "size=150-700 pixel circularity=0.40-1.00 show=Nothing  
display exclude include");  
>run("Open Next");  
>}  
>setBatchMode(false);
```

Appendix C.2 Automation of ImageJ Macro Within MATLAB

```
% Linkam output automation using ImageJ and MIJ packages

clc, clear, close all

% add mij.jar java package
% can be found at http://bigwww.epfl.ch/sage/soft/mij/
javaaddpath 'C:\Program
Files\MATLAB\R2015a\java\jar\mij.jar'

% add ij.jar to usable path -should be included with your
normal IJ install
javaaddpath 'C:\Program
Files\MATLAB\R2015a\java\jar\ij.jar'

% initialize MIJ
MIJ.start;
% Installs most current "measure500.ijm" with path
% Note: 'measure500' is a misnomer...now measures all RBCs
in dir (1/3/17)
% MIJ.run('Install...',
'path=[/Applications/ImageJ/plugins/measure500.ijm]');
MIJ.run('Install...',
'path=[C:\Users\Dan\Documents\ImageJ\ImageJ\plugins]');

% *****
% NOTE!:
% Make your folders in the form of:
% Parent\Experiment_shearRate_trial\image.tif
% where 'Parent' is the input below (commonly the exp date)
and
% EXP_shearRate_trial holds your tiff images
% *****

parent = '<parent directory>';
parentContents = dir(parent);
dirs = {};

folderList = {};

for f = length(parentContents):-1:1
```

```

    if parentContents(f).name(1) == '.'
        folderList{f} = [];
    elseif parentContents(f).isdir
        folderList{f} = char(parentContents(f).name);
    else
        folderList{f} = [];
    end
end

end
folderList = folderList(~cellfun('isempty', folderList));

for n = 1:length(folderList)
%     dirs(n) = strcat(parent,'/',folderList(n)); % MAC
VERSION
    dirs(n) = strcat(parent,'\ ',folderList(n)); % WINDOWS
VERSION
end

%% END DATE FOLDER SECTION

% % % legendList = {};
for iA = length(dirs):-1:1
    % move in directory specified by parent folder and
    trial folder
    cd(char((dirs(iA))));
%     pwd % (for testing)
    tifList = dir(char(dirs(iA)));

    trueTifList = {};
    for j = 1:length(tifList)
        [~,~,ext] = fileparts(tifList(j).name);
        if strcmp(ext, '.tif')
            trueTifList = [trueTifList; tifList(j).name];
        end
    end

end

%create string in form of 'path=[<path>]' for use with MIJ
%     for macs:
%     MIJpath =
strcat('path=[',char(dirs(iA)), '/',trueTifList(1),']');
    MIJpath =
strcat('path=[',char(dirs(iA)), '\ ',trueTifList(1),']');

```

```

%% DO IMAGEJ THINGS HERE

    MIJ.run('Open...', MIJpath);
%

%      %when first .tif is open via 'MIJPath', run the
measure500 macro
    MIJ.run('measure500');

    % ***** 'data' collected in columns:
Area,X,Y,Major,Minor,Angle*****

    data = MIJ.getResultsTable;

    % Append table to include EI
    data = [data abs((data(:,4) - data(:,5)) ./ (data(:,4)
+ data(:,5)))]];
    dateInfo = datestr(now, '__dd_mmm_yyyy_HH_MM_SS');
    csvwrite(strcat(char(dirs(iA)),dateInfo, '.txt'),data);

    clear data
%      clear fileName
% %      clear legendList
    MIJ.run('Clear Results');
    MIJ.closeAllWindows;
end
%END MIJ SECTION

%return back to the original date folder
cd(parent);
MIJ.closeAllWindows;
MIJ.exit;

```

Appendix C.3 Logistic Regression Algorithm

```
% Uses input from RBC_measure to differentiate between
heathy/rigid RBCs
clc, clear, close all
format long

parent = '<parent dir>';

addpath 'C:\Users\Dan\Box Sync\Art Blood
Shared\DJC\Linkam\MATLAB'
if isdir(fullfile(parent, 'Graphs')) == false
    mkdir(parent, '\Graphs')
end

cd(char(parent));
parentContents = dir(parent);

% Take only txt files as input
txtList = {};
for j = 1:length(parentContents)
    [~,NAME,EXT] = fileparts(parentContents(j).name);
    if strcmp(EXT, '.txt')
        txtList = [txtList; parentContents(j).name];
    end
end

% Load txt file name, using only those with 7 columns
% columns: Area,X,Y,Major,Minor,Angle, EI
for n = 1:length(txtList)
    temp = txtList(n);
    load(char(temp));
    [~,NAME,~] = fileparts(char(temp));

    [~,width] = size(eval(NAME));
    if width ~= 7
        txtList(n) = [];
    end
end
```

```

txtNames = {};
for t = 1:length(txtList)
    [~,NAME,~] = fileparts(char(txtList(t)));
    txtNames = [txtNames; NAME];
end

%% 500 SR
CM_500 = txtList(contains(txtList, 'CM') &
contains(txtList, '500'));
CB1_500 = txtList(contains(txtList, 'CB1') &
contains(txtList, '500'));
CB2_500 = txtList(contains(txtList, 'CB2') &
contains(txtList, '500'));

XM_500 = txtList(contains(txtList, 'XM') &
contains(txtList, '500'));
XB1_500 = txtList(contains(txtList, 'XB1') &
contains(txtList, '500'));
XB2_500 = txtList(contains(txtList, 'XB2') &
contains(txtList, '500'));

Test_500 = {CM_500 CB1_500 CB2_500 XM_500 XB1_500 XB2_500};

Pool_500 = txtList(contains(txtList, 'Pool') &
contains(txtList, '500'));
Rigid_500 = txtList(contains(txtList, 'Rigid') &
contains(txtList, '500'));
Healthy_500 = txtList(contains(txtList, 'Healthy') &
contains(txtList, '500'));

theta500 =
LogisticRegression(parent, Pool_500, Rigid_500, Healthy_500, Te
st_500);

%% 1000 SR
CM_1000 = txtList(contains(txtList, 'CM') &
contains(txtList, '1000'));
CB1_1000 = txtList(contains(txtList, 'CB1') &
contains(txtList, '1000'));
CB2_1000 = txtList(contains(txtList, 'CB2') &
contains(txtList, '1000'));

```

```

XM_1000 = txtList(contains(txtList,'XM') &
contains(txtList,'1000'));
XB1_1000 = txtList(contains(txtList,'XB1') &
contains(txtList,'1000'));
XB2_1000 = txtList(contains(txtList,'XB2') &
contains(txtList,'1000'));

Test_1000 = {CM_1000 CB1_1000 CB2_1000 XM_1000 XB1_1000
XB2_1000};

Pool_1000 = txtList(contains(txtList,'Pool') &
contains(txtList,'1000'));
Rigid_1000 = txtList(contains(txtList,'Rigid') &
contains(txtList,'1000'));
Healthy_1000 = txtList(contains(txtList,'Healthy') &
contains(txtList,'1000'));

theta1000 =
LogisticRegression(parent,Pool_1000,Rigid_1000,Healthy_1000
,Test_1000);

```

Appendix C.4 LogisticRegression.m MATLAB Function File

```

function [theta] = LogisticRegression(parent, pool, rigid,
healthy, test)

parent = fullfile(parent,'Graphs');

poolData = [];
for p = 1:length(pool)
    poolData = [poolData ; csvread(char(pool(p)))
p*ones(length(csvread(char(pool(p))))),1)];
end

rigidData = [];
for r = 1:length(rigid)

```

```

        rigidData = [rigidData; csvread(char(rigid(r)))
r*ones(length(csvread(char(rigid(r)))),1)];
end

healthyData = [];
for h = 1:length(healthy)
    healthyData = [healthyData; csvread(char(healthy(h)))
h*ones(length(csvread(char(healthy(h)))),1)];
end

X = [ones(length(rigidData),1), rigidData(:,4:5);
ones(length(healthyData),1), healthyData(:,4:5)];
y = [zeros(length(rigidData),1)
;ones(length(healthyData),1)];

int_theta = zeros(3,1);

[theta, cost] = fminunc(@(t)(costFuncJ(t, X, y)),
int_theta);

h = 1 ./ (1 + exp(-(X*theta)));
idx_h = round(h);

hPool = zeros(length(poolData),1);
for p = 1:length(poolData)
%     hPool(p) = theta(1) + theta(2)*pool(p,4) +
theta(3)*pool(p,5);
    if theta(1) + theta(2)*poolData(p,4) +
theta(3)*poolData(p,5) > 0
        hPool(p) = 1; % healthy == 1
    elseif theta(1) + theta(2)*poolData(p,4) +
theta(3)*poolData(p,5) < 0
        hPool(p) = 0; % rigid == 0
    end
end

figure('units','normalized','outerposition',[0 0 1 1])

hold on
% 5: width (X axis), 4: length (Y axis)

```

```

plot(poolData(hPool==1 &
poolData(:,8)==1,5),poolData(hPool==1 &
poolData(:,8)==1,4), 'mo');
plot(poolData(hPool==1 &
poolData(:,8)==2,5),poolData(hPool==1 &
poolData(:,8)==2,4), 'md');
plot(poolData(hPool==0 &
poolData(:,8)==1,5),poolData(hPool==0 &
poolData(:,8)==1,4), 'bo');
plot(poolData(hPool==0 &
poolData(:,8)==2,5),poolData(hPool==0 &
poolData(:,8)==2,4), 'bd');

plot(rigidData(rigidData(:,8)==1,5),rigidData(rigidData(:,8)
)==1,4), 'k+');
plot(rigidData(rigidData(:,8)==2,5),rigidData(rigidData(:,8)
)==2,4), 'k*');

plot(healthyData(healthyData(:,8)==1,5),healthyData(healthy
Data(:,8)==1,4), 'r+');
plot(healthyData(healthyData(:,8)==2,5),healthyData(healthy
Data(:,8)==2,4), 'r*');

% calculate and plot decision boundary.
plot_x = [0.9*min(X(:,2)), 1.1*max(X(:,2))];
plot_y = (-1./theta(3)).*(theta(2).*plot_x + theta(1));
theta
plot(plot_y, plot_x)
hold off
axis([ 0.02 0.08 0.04 0.22]);
title(char(pool), 'interpreter', 'none');
legend('Pool Healthy t1', 'Pool Healthy t2', 'Pool Rigid
t1', 'Pool Rigid t2', 'Rigid Control t1', 'Rigid Control
t2', 'Healthy Control t1', 'Healthy Control t2', 'Decision
Boundary');

controlContents = [
length(poolData),
length(poolData(hPool==1)),
100*length(poolData(hPool==1))/length(poolData),
length(poolData(hPool==0)),
100*length(poolData(hPool==0))/length(poolData),
length(healthyData),

```

```

length(rigidData)];

controlText = sprintf('\n cells in Pool: %d\n\n healthy: %d
(%f%%)\n\n rigid: %d (%f%%)\n\n in rigid control: %d\n\n in
healthy control: %d',controlContents);
ax = axis;
text(0.65*ax(2),ax(4),controlText,'VerticalAlignment','top'
);

name = char(pool(1));
saveas(gcf,fullfile(parent,name(1:end-4)),'jpeg')

table(controlContents)

if exist('test','var') == true
    for cell = 1:length(test)
        % PLOT CONTROLS HERE REPEATEDLY
        figure('units','normalized','outerposition',[0 0 1
1])
        subplot(1,2,1), hold on
        % column 5: width (X axis), column 4: length (Y
axis)
        plot(poolData(hPool==1 &
poolData(:,8)==1,5),poolData(hPool==1 &
poolData(:,8)==1,4),'mo');
        plot(poolData(hPool==1 &
poolData(:,8)==2,5),poolData(hPool==1 &
poolData(:,8)==2,4),'md');
        plot(poolData(hPool==0 &
poolData(:,8)==1,5),poolData(hPool==0 &
poolData(:,8)==1,4),'bo');
        plot(poolData(hPool==0 &
poolData(:,8)==2,5),poolData(hPool==0 &
poolData(:,8)==2,4),'bd');

plot(rigidData(rigidData(:,8)==1,5),rigidData(rigidData(:,8)
)==1,4),'k+');

plot(rigidData(rigidData(:,8)==2,5),rigidData(rigidData(:,8)
)==2,4),'k*');

```

```

plot(healthyData(healthyData(:,8)==1,5),healthyData(healthy
Data(:,8)==1,4),'r+');

plot(healthyData(healthyData(:,8)==2,5),healthyData(healthy
Data(:,8)==2,4),'r*');
    plot(plot_y, plot_x)
    hold off
    axis([ 0.02 0.08 0.04 0.22]);
    title(char(pool),'interpreter','none');
    legend('Pool Healthy t1','Pool Healthy t2','Pool
Rigid t1','Pool Rigid t2','Rigid Control t1','Rigid Control
t2','Healthy Control t1','Healthy Control t2','Decision
Boundary');
    controlText = sprintf('\n cells in Pool: %d\n\n
healthy: %d (%f%)\n\n rigid: %d (%f%)\n\n in rigid control:
%d\n\n in healthy control: %d',controlContents);
    ax = axis;

text(0.28*ax(2),ax(4),controlText,'VerticalAlignment','top'
);

    % DO STUFF TO INDIVIDUAL TEST (experimental) CASES
    tempTest = [];
    for trial = 1:length(test{cell})
        tempTest = [tempTest;
csvread(char(test{cell}(trial)))
trial*ones(length(csvread(char(test{cell}(trial)))),1)];
    end
    hTest = zeros(length(tempTest),1);
    for t = 1:length(tempTest)
        if theta(1) + theta(2)*tempTest(t,4) +
theta(3)*tempTest(t,5) > 0
            hTest(t) = 1; % healthy == 1
        elseif theta(1) + theta(2)*tempTest(t,4) +
theta(3)*tempTest(t,5) < 0
            hTest(t) = 0; % rigid == 0
        end
    end

    % make subplot part 2
    subplot(1,2,2), hold on

```

```

        plot(tempTest(hTest==1 &
tempTest(:,8)==1,5),tempTest(hTest==1 &
tempTest(:,8)==1,4), 'mo');
        plot(tempTest(hTest==1 &
tempTest(:,8)==2,5),tempTest(hTest==1 &
tempTest(:,8)==2,4), 'rd');

        plot(tempTest(hTest==0 &
tempTest(:,8)==1,5),tempTest(hTest==0 &
tempTest(:,8)==1,4), 'bo');
        plot(tempTest(hTest==0 &
tempTest(:,8)==2,5),tempTest(hTest==0 &
tempTest(:,8)==2,4), 'cd');

        plot_x = [0.9*min(X(:,2)), 1.1*max(X(:,2))];
        plot_y = (-1./theta(3)).*(theta(2).*plot_x +
theta(1));
        plot(plot_y, plot_x)
        hold off
        axis([ 0.02 0.08 0.04 0.22]);

        testContents = [
length(tempTest),
length(tempTest(hTest==1)),
100*length(tempTest(hTest==1))/length(tempTest)
length(tempTest(hTest==0)),
100*length(tempTest(hTest==0))/length(tempTest)];
        testText = sprintf('\n cells in experimental run:
%d\n\n healthy cells: %d (%f%%)\n\n rigid cells: %d
(%f%%)',testContents);
        ax = axis;

text(0.28*ax(2),ax(4),testText,'VerticalAlignment','top');

title(char(test{cell}(trial)),'interpreter','none');
        legend('Healthy t1','Healthy t2','Rigid t1','Rigid
t2','Decision Boundary')
        name = char(test{cell}(trial));
        saveas(gcf,fullfile(parent,name(1:end-4)),'jpeg')
        table(testContents,'VariableNames',{name(1:end-4)})
        clear tempTest hTest testContents

```

```

        end
    else
    end

disp('Exiting Function Logistic Regression');
end

```

Appendix C.5 costFunction.m MATLAB Function File

```

function [ J, grad] = costFuncJ(theta, X, y)

[m,n] = size(X);
J = 0;
grad = zeros(n,1);

h = 1 ./ (1 + exp(-(X*theta)));

J = 1/m * sum(-y.*log(h)-(1-y).*log(1-h)); % cost

for k = 1:n
grad(k) = 1/m * sum(X(:,k)'*(h-y));
end

end

```

Bibliography

1. Wintrobe MM. Laboratory Hematology: Examination of the Blood and Bone Marrow. In: *Wintrobe's Clinical Hematology*. Lippincott Williams & Wilkins; 2008:1-20.
2. Caro CG, Pedley TJ, Schroter RC, Seed WA. Blood. In: *The Mechanics of the Circulation*. Oxford University Press; 1978:151-180.
3. Popel AS, Johnson PC. Microcirculation and Hemorheology. *Annu Rev Fluid Mech*. 2005;37(8):43-69.
4. Cengel YA, Cimbala JM. Laminar and Turbulent Flows. In: *Fluid Mechanics: Fundamentals and Applications*. Second Edi. Tata-McGraw Hill Companies Publications; 2006:337-417.
5. Caro CG, Pedley TJ, Schroter RC, Seed WA. The Systemic Microcirculation. In: *The Mechanics of the Circulation*. Cambridge University Press; 1978:350-433.
6. Formaggia L, Quarteroni A, Veneziani A. Physiology and Pathology of the Cardiovascular System. In: *Cardiovascular Mathematics: Modeling and Simulation of the Circulatory System*. 1st ed. Springer Sciences and Business; 2010:1-39.
7. Popel AS, Regirer SA, Usick PI. A Continuum Model of Blood Flow. *Biorheology*. 1974;11(6):427-437.
8. Sharan M, Popel AS. A two-phase model for flow of blood in narrow tubes with increased effective viscosity near the wall. *Biorheology*. 2001;38:415-428.
9. Fåhræus R. The Suspension Stability of the Blood. *Physiol Rev*. 1929;9(2):241-274.
10. Goldsmith HL, Cokelet GR, Gaehtgens P. Robin Fåhræus: Evolution of his concepts in cardiovascular physiology. *Am J Physiol*. 1989;257(3):H1005-H1015.
11. Fåhræus R, Lindqvist T. The viscosity of the blood in narrow capillary tubes. *Am J Physiol*. 1931;96(3):562-568.
12. Kim S, Ong PK, Yalcin O, Intaglietta M, Johnson PC. The cell-free layer in microvascular blood flow. *Biorheology*. 2009;46(3):181-189.
13. Goldsmith HL, Marlow JC. Flow Behavior of Erythrocytes II. Particle Motions in Concentrated Suspensions of Ghost Cells. *J Colloid Interface Sci*. 1979;71(2):383-407.
14. Geislinger TM, Franke T. Hydrodynamic lift of vesicles and red blood cells in flow - From Fåhræus & Lindqvist to microfluidic cell sorting. *Adv Colloid Interface Sci*. 2014;208:161-176.

15. Chen Y, Li D, Li Y, Wan J, Li J, Chen H. Margination of Stiffened Red Blood Cells Regulated by Vessel Geometry. *Sci Rep.* 2017;7(1):1-9.
16. Katanov D, Gompper G, Fedosov DA. Microvascular blood flow resistance: Role of red blood cell migration and dispersion. *Microvasc Res.* 2015;99:57-66.
17. Boyle J. Microcirculatory hematocrit and blood flow. *J Theor Biol.* 1988;131(2):223-229.
18. Sarelius IH, Duling BR. Direct measurement of microvessel hematocrit, red cell flux, velocity, and transit time. *Am J Physiol.* 1982;243(6):H1018-H1026.
19. Zhao R, Marhefka JN, Antaki JF, Kameneva MV. Drag-reducing polymers diminish near-wall concentration of platelets in microchannel blood flow. *Biorheology.* 2010;47:193-203.
20. Zhao H, Shaqfeh ESG. Shear-induced platelet margination in a microchannel. *Phys Rev E - Stat Nonlinear, Soft Matter Phys.* 2011;83(6):1-6.
21. Freund JB. Leukocyte margination in a model microvessel. *Phys Fluids.* 2007;19(2):023301.
22. Namgung B, Ng YC, Leo HL, Rifkind JM, Kim S. Near-wall migration dynamics of erythrocytes in vivo: Effects of cell deformability and arteriolar bifurcation. *Front Physiol.* 2017;8:1-10.
23. Zhang X. Cross-stream distribution of red blood cells in sickle-cell disease. *Am Phys Soc.* 2017;62:KP1-038.
24. Perkkiö J, Wurzinger LJ, Schmid-Schönbein H. Fåhræus-vejlens effect: Margination of platelets and leukocytes in blood flow through branches. *Thromb Res.* 1988;50(3):357-364.
25. Lipowsky HH. Microvascular rheology and hemodynamics. *Microcirculation.* 2005;12(1):5-15.
26. Thurston GB. Viscoelasticity of Human Blood. *Biophys J.* 1972;12(4):1205-1217.
27. Thurston GB, Henderson NM. Effects of flow geometry on blood viscoelasticity. *Biorheology.* 2006;43(6):729-746.
28. Thurston GB. The effects of frequency of oscillatory flow on the impedance of rigid, blood filled tubes. *Biorheology.* 1976;13(3):191-199.
29. Thurston GB. Frequency and shear rate dependence of viscoelasticity of human blood. *Biorheology.* 1973;10(3):375-381.
30. Engstrom KG, Moller B, Meiselman HJ. Optical evaluation of red blood cell geometry using micropipette aspiration. *Blood Cells.* 1992;18(2):258-265.
31. Bessis M, Mohandas N, Feo C. Automated ektacytometry: A new method of measuring red cell deformability and red cell indices. *Blood Cells.* 1980;6(3):315-327.

32. Parrow NL, Violet P-C, Tu H, et al. Measuring Deformability and Red Cell Heterogeneity in Blood by Ektacytometry. *J Vis Exp*. 2018;(131):1-9.
33. Musielak M. Red blood cell-deformability measurement: Review of techniques. *Clin Hemorheol Microcirc*. 2009;42(1):47-64.
34. Lipowsky HH, Cram LE, Justice W, Eppihimer MJ. Effect of erythrocyte deformability on in vivo red cell transit time and hematocrit and their correlation with in vitro filterability. *Microvasc Res*. 1993;46(1):43-64.
35. Skalak R, Hanss M, Chien S. Indices of Filterability of Red Blood Cell Suspensions. *Biorheology*. 1983;20(3):311-316.
36. Nowakowski R, Luckham P, Winlove P. Imaging erythrocytes under physiological conditions by atomic force microscopy. *Biochim Biophys Acta - Biomembr*. 2001;1514(2):170-176.
37. Guo Q, Duffy SP, Matthews K, Santoso AT, Scott MD, Ma H. Microfluidic analysis of red blood cell deformability. *J Biomech*. 2014;47(8):1767-1776.
38. Zare RN, Kim S. Microfluidic platforms for single-cell analysis. *Annu Rev Biomed Eng*. 2010;12:187-201.
39. Késmárky G, Kenyeres P, Rábai M, Tóth K. Plasma viscosity: A forgotten variable. *Clin Hemorheol Microcirc*. 2008;39(1-4):243-246.
40. Baskurt OK, Hardeman MR, Rampling MW. Macro- and Micro-Rheological Properties of Blood. In: *Handbook of Hemorheology and Hemodynamics*. Vol. 69. IOS Press; 2007:45-71.
41. Weatherall D. Hemoglobinopathies Worldwide: Present and Future. *Curr Mol Med*. 2008;8(7):592-599.
42. Weatherall DJ, Clegg JB. Inherited haemoglobin disorders: An increasing global health problem. *Bull World Health Organ*. 2001;79(8):704-712.
43. Hassell KL. Population Estimates of Sickle Cell Disease in the U.S. *Am J Prev Med*. 2010;38(4):512-521.
44. Vos T, Allen C, Arora M, et al. Global, regional, and national incidence, prevalence, and years lived with disability for 310 diseases and injuries, 1990–2015: a systematic analysis for the Global Burden of Disease Study 2015. *Lancet*. 2016;388(10053):1545-1602.
45. National Institutes of Health. The Management of Sickle Cell Disease. *NIH Publ No 02-2117*. Published online 2002.
46. Williams TN, Mwangi TW, Wambua S, et al. Sickle cell trait and the risk of Plasmodium falciparum malaria and other childhood diseases. *J Infect Dis*. 2005;192(1):178-186.

47. Williams TN. Red blood cell defects and malaria. *Mol Biochem Parasitol.* 2006;149(2):121-127.
48. Rees DC, Williams TN, Gladwin MT. Sickle-cell disease. *Lancet.* 2010;376(9757):2018-2031.
49. Franklin Bunn H. Pathogenesis and Treatment of Sickle Cell Disease. *N Engl J Med.* 1997;337:762-769.
50. Sundd P, Gladwin MT, Novelli EM. Pathophysiology of Sickle Cell Disease. *Annu Rev Pathol Mech Dis.* 2019;14:263-292.
51. Platt OS. Sickle cell anemia as an inflammatory disease. *J Clin Invest.* 2000;106(3):337-338.
52. Barabino GA, Platt MO, Kaul DK. Sickle Cell Biomechanics. *Annu Rev Biomed Eng.* 2010;12(1):345-367.
53. Bensinger TA, Gillette PN. Hemolysis in Sickle Cell Disease. *Arch Intern Med.* 1974;133(4):624-631.
54. Kaul DK, Fabry ME, Windisch P, Baez S, Nagel RL. Erythrocytes in sickle cell anemia are heterogeneous in their rheological and hemodynamic characteristics. *J Clin Invest.* 1983;72(1):22-31.
55. Klug PP, Lessin LS, Radice P. Rheological Aspects of Sickle Cell Disease. *Arch Intern Med.* 1974;133(4):577-590.
56. Chien S. Red cell deformability and its relevance to blood flow. *Annu Rev Physiol.* 1987;49:177-192.
57. Chien S. Rheology of sickle cells and erythrocyte content. *Blood Cells.* 1977;3(2):283-303.
58. Brandow AM, Carroll CP, Creary S, et al. American Society of Hematology 2020 guidelines for sickle cell disease: Management of acute and chronic pain. *Blood Adv.* 2020;4(12):2656-2701.
59. Gladwin MT, Vichinsky E. Pulmonary Complications of Sickle Cell Disease. *N Engl J Med.* 2008;359(21):2254-2265.
60. Melton CW, Haynes J. Sickle Acute Lung Injury: Role of Prevention and Early Aggressive Intervention Strategies on Outcome. *Clin Chest Med.* 2006;27(3):487-502.
61. Chen G, Zhang D, Fuchs TA, Manwani D, Wagner DD, Frenette PS. Heme-induced neutrophil extracellular traps contribute to the pathogenesis of sickle cell disease. *Blood.* 2014;123(24):3818-3827.

62. Zhang D, Xu C, Manwani D, Frenette PS. Neutrophils, platelets, and inflammatory pathways at the nexus of sickle cell disease pathophysiology. *Blood*. 2016;127(7):801-809.
63. Ansari J, Gavins FNE. Ischemia-Reperfusion Injury in Sickle Cell Disease: From Basics to Therapeutics. *Am J Pathol*. 2019;189(4):706-718.
64. Harris JW, Brewster HH, Hale Ham T, Castle WB. Studies on the Destruction of Red Blood Cells: The Biophysics and Biology of Sickle-Cell Disease. *AMA Arch Intern Med*. 1956;97(2):145-168.
65. Platt OS. Hydroxyurea for the Treatment of Sickle Cell Disease. *N Engl J Med*. 2008;358(13):1362-1369.
66. Niihara Y, Miller ST, Kanter J, et al. A Phase 3 Trial of L-Glutamine in Sickle Cell Disease. *N Engl J Med*. 2018;379(3):226-235.
67. Brousseau D, Owens P, Mosso A, Panepinto J, Steiner C. Acute Care Utilization and Rehospitalizations for Sickle Cell Disease. *Jama*. 2010;303(13):1288-1294.
68. Ataga KI, Kutlar A, Kanter J, et al. Crizanlizumab for the prevention of pain crises in sickle cell disease. *N Engl J Med*. 2017;376(5):429-439.
69. Vichinsky E, Hoppe CC, Ataga KI, et al. A Phase 3 randomized trial of voxelotor in sickle cell disease. *N Engl J Med*. 2019;381(6):509-519.
70. Yazdanbakhsh K, Ware RE, Noizat-Pirenne F. Red blood cell alloimmunization in sickle cell disease: pathophysiology, risk factors, and transfusion management. *Blood*. 2012;120(3):528-537.
71. Walters M, Patience M, Leisenring W, et al. Bone Marrow Transplantation for Sickle Cell Disease. *N Engl J Med*. 1997;335:897-904.
72. Ware RE, de Montalembert M, Tshilolo L, Abboud MR. Sickle cell disease. *Lancet*. 2017;390(10091):311-323.
73. Toms BA. Some Observations on the Flow of Linear Polymer Solutions Through Straight Tubes at Large Reynolds Numbers. *Proc Int Congr Rheol*. 1948;1:135-141.
74. Gadd GE. Turbulence Dampening and Drag Reduction Produced by Certain Additives in Water. *Nature*. 1965;206(4983):463-467.
75. Gadd GE. Reduction of Turbulent Friction in Liquids by Dissolved Additives. *Nature*. 1966;212(5065):874-877.
76. Kulicke WM, Kötter M, Gräger H. Drag reduction phenomenon with special emphasis on homogeneous polymer solutions. *Polym Charact Solut*. 1989;89:1-68.
77. Driels MR, Ayyash S. Drag Reduction in Laminar Flow. *Nature*. 1976;259:389-390.

78. Keller A, Kiss G, Mackley MR. Polymer Drag Reduction in Taylor Vortices. *Nature*. 1975;257:304-305.
79. Mostardi R, Thomas L, Greene H, VanEssen F, Nokes R. Suppression of Atherosclerosis in Rabbits Using Drag Reducing Polymers. *Biorheology*. 1978;15(1):1-14.
80. Kameneva MV, Polyakova MS, Fedoseeva EV. Effect of drag-reducing polymers on the structure of the stagnant zones and eddies in models of constricted and branching blood vessels. *Fluid Dyn*. 1990;6:956-959.
81. Kameneva MV, Polyakova MS, Gvozdkova IA. Nature of the influence of polymers that lower hydrodynamic resistance on blood circulation. *Proc Acad Sci USSR Biophys Sect*. Published online 1988:22-24.
82. Kameneva MV, Wu ZJ, Uraysh A, et al. Blood soluble drag-reducing polymers prevent lethality from hemorrhagic shock in acute animal experiments. *Biorheology*. 2004;41(1):53-64.
83. Pacella JJ, Kameneva MV, Csikari M, Lu E, Villanueva FS. A novel hydrodynamic approach to the treatment of coronary artery disease. *Eur Heart J*. 2006;27(19):2362-2369.
84. Pacella JJ, Kameneva MV, Villanueva FS. Drag reducing polymers improve coronary flow reserve through modulation of capillary resistance. *Biorheology*. 2009;46(5):365-3781.
85. Cotoia A, Kameneva MV, Marascalco PJ, Fink MP, Delude RL. Drag-reducing hyaluronic acid increases survival in profoundly hemorrhaged rats. *Shock*. 2009;31(3):258-261.
86. Marascalco PJ, Blair HC, Nieponice A, Robinson LJ, Kameneva MV. Intravenous injections of soluble drag-reducing polymers reduce foreign body reaction to implants. *ASAIO J*. 2009;55(5):503-508.
87. Chen X, Zha D, Xiu J, et al. A new hydrodynamic approach by infusion of drag-reducing polymers to improve left ventricular function in rats with myocardial infarction. *Int J Cardiol*. 2011;147(1):112-117.
88. Hu F, Zha D, Du R, et al. Improvement of the microcirculation in the acute ischemic rat limb during intravenous infusion of drag-reducing polymers. *Biorheology*. 2011;48:149-159.
89. Brands J, Kliner D, Lipowsky HH, Kameneva MV, Villanueva FS, Pacella JJ. New Insights into the Microvascular Mechanisms of Drag Reducing Polymers: Effect on the Cell-Free Layer. *PLoS One*. 2013;8(10):1-10.
90. Tohme S, Kameneva MV, Yazdani HO, et al. Drag reducing polymers decrease hepatic injury and metastases after liver ischemia-reperfusion. *Oncotarget*. 2017;8(35):59854-59866.

91. Bragin DE, Kameneva MV, Bragina OA, et al. Rheological effects of drag-reducing polymers improve cerebral blood flow and oxygenation after traumatic brain injury in rats. *J Cereb Blood Flow Metab.* 2017;37(3):762-775.
92. Ding Z, Joy M, Kameneva MV, Roy P. Nanomolar concentration of blood-soluble drag-reducing polymer inhibits experimental metastasis of human breast cancer cells. *Breast Cancer Targets Ther.* 2017;9:61-65.
93. Bragin DE, Bragina OA, Kameneva MV, Nemoto EM. Resuscitation with Drag Reducing Polymers after Traumatic Brain Injury with Hemorrhagic Shock Reduces Microthrombosis and Oxidative Stress. *Adv Exp Med Biol.* 2020;1232:39-45.
94. Stein PD, Sabbah HN. Turbulent blood flow in the ascending aorta of humans with normal and diseased aortic valves. *Circ Res.* 1976;39(1):58-65.
95. Antiga L, Steinman DA. Rethinking turbulence in blood. *Biorheology.* 2009;46(2):77-81.
96. Kameneva MV. Microrheological effects of drag-reducing polymers in vitro and in vivo. *Int J Eng Sci.* 2012;59:168-183.
97. Marhefka JN, Zhao R, Wu Z, Velankar SS, Antaki JF, Kameneva MV. Drag reducing polymers improve tissue perfusion via modification of the RBC traffic in microvessels. *Biorheology.* 2009;46(4):281-292.
98. Pacella JJ, Kameneva MV, Lavery LL, et al. A novel hydrodynamic method for microvascular flow enhancement. *Biorheology.* 2009;46(4):293-308.
99. Barnard BJS, Sellin RHJ. Degradation of Dilute Solutions of Drag-reducing Polymer. *Nat Phys Sci.* 1972;236(62):12-14.
100. McGary CW. Degradation of poly(ethylene oxide). *J Polym Sci.* 1960;46(147):51-57.
101. Kauf TL, Coates TD, Huazhi L, Mody-Patel N, Hartzema AG. The cost of health care for children and adults with sickle cell disease. *Am J Hematol.* 2009;84(6):323-327.
102. Thompson AA. Ideal donors, imperfect results in sickle cell disease. *Blood.* 2013;122(6):858-859.
103. Caro CG, Pedley TJ, Schroter RC, Seed WA. The Systemic Circulation. In: *The Mechanics of the Circulation.* ; 1978:350-433.
104. Pacella J, Kameneva MV, Lu E, Csikari M, Fischer D, Villanueva FS. Effect of drag reducing polymers in myocardial perfusion during coronary stenosis. *Eur Heart J.* 2006;19:2362-2369.
105. Huisjes R, Bogdanova A, van Solinge WW, Schiffelers RM, Kaestner L, van Wijk R. Squeezing for life - Properties of red blood cell deformability. *Front Physiol.* 2018;9(656):1-22.

106. Rakow AL, Hochmuth RM. Effect of heat treatment on the elasticity of human erythrocyte membrane. *Biophys J*. 1975;15(11):1095-1100.
107. Utoh J, Zajkowski-Brown J, Haraski H. Effects of heat on fragility and morphology of human and calf erythrocytes. *J Inverstigative Surg*. 1992;5:305-313.
108. Linkam Scientific Instruments. *CSS450 Optical Rheology System User Guide v1.3.*; 2014.
109. Hellmuth R. Modelling shear-induced platelet aggregation in general flow. Published online 2016.
110. Schneider CA, Rasband WS, Eliceiri KW. NIH Image to ImageJ: 25 years of image analysis. *Nat Methods*. 2012;9(7):671-675.
111. Raval JS, Waters JH, Seltsam A, et al. The use of the mechanical fragility test in evaluating sublethal RBC injury during storage. *Vox Sang*. 2010;99(4):325-331.
112. Xu Z, Zheng Y, Wang X, Shehata N, Wang C, Sun Y. Stiffness increase of red blood cells during storage. *Microsystems Nanoeng*. 2018;4(1):1-6.
113. Cabrales P. Effects of erythrocyte flexibility on microvascular perfusion and oxygenation during acute anemia. *Am J Physiol - Hear Circ Physiol*. 2007;293(2):1206-1215.
114. Crompton D, Vats R, Pradhan-sundd T, Sundd P, Kameneva MV. Drag-reducing polymers improve hepatic vaso-occlusion in SCD mice. *Blood Adv*. 2020;4(18):4333-4336.
115. Ballas SK, Mohandas N. Sickie red cell microrheology and sickie blood rheology. *Microcirculation*. 2004;11(2):209-225.
116. Connes P, Alexy T, Detterich J, Romana M, Hardy-Dessources M-D, Ballas S. The role of blood rheology in sickie cell disease. *Blood Rev*. 2016;30(2):111-118.
117. Chien S, King R, Kaperonis A, Usami S. Viscoelastic Properties of Sickie Cells and Hemoglobin. *Blood Cells*. 1981;8(1):53-64.
118. Chien S, Usami S, Bertles JF. Abnormal rheology of oxygenated blood in sickie cell anemia. *J Clin Invest*. 1970;49(4):623-634.
119. Caprari P, Massimi S, Diana L, et al. Hemorheological Alterations and Oxidative Damage in Sickie Cell Anemia. *Front Mol Biosci*. 2019;6(142):1-8.
120. Kaul DK, Finnegan E, Barabino GA. Sickie Red Cell - Endothelium Interactions. *Microcirculation*. 2009;16(1):97-111.
121. Wu LC, Sun CW, Ryan TM, Pawlik KM, Ren J, Townes TM. Correction of sickie cell disease by homologous recombination in embryonic stem cells. *Blood*. 2006;108(4):1183-1188.

122. Pradhan-Sundd T, Vats R, Russell JO, et al. Dysregulated Bile Transporters and Impaired Tight Junctions During Chronic Liver Injury in Mice. *Gastroenterology*. 2018;155(4):1218-1232.
123. Vats R, Liu S, Zhu J, et al. Impaired bile secretion promotes hepatobiliary injury in Sickle Cell Disease. *Hepatology*. Published online 2020.
124. Schindelin J, Arganda-Carrera I, Frise E, et al. Fiji - an Open platform for biological image analysis. *Nat Methods*. 2009;9(7):676-682.
125. Arganda-Carreras I, Kaynig V, Rueden C, et al. Trainable Weka Segmentation: A machine learning tool for microscopy pixel classification. *Bioinformatics*. 2017;33(15):2424-2426.
126. Yawn BP, John-Sowah J. Management of sickle cell disease: Recommendations from the 2014 expert panel report. *Am Fam Physician*. 2015;92(12):1069-1076.
127. Chou ST, Fasano RM. Management of Patients with Sickle Cell Disease Using Transfusion Therapy: Guidelines and Complications. *Hematol Oncol Clin North Am*. 2016;30(3):591-608.
128. Smith-Whitley K, Thompson AA. Indications and Complications of Transfusions in Sickle Cell Disease. *Pediatr Blood Cancer*. 2008;59(2):358-364.
129. Adams RJ, Mckie VC, Hsu L, et al. Prevention of a first stroke by transfusions in children with sickle cell anemia and abnormal results on transcranial Doppler ultrasonography. *N Engl J Med*. 1998;339(1):5-11.
130. Emre U, Miller ST, Gutierrez M, Steiner P, Rao SP, Rao M. Effect of transfusion in acute chest syndrome of sickle cell disease. *J Pediatr*. 1995;127(6):901-904.
131. Styles LA, Vichinsky E. Effects of a long-term transfusion regimen on sickle cell-related illnesses. *J Pediatr*. 1994;125(6):909-911.
132. Vichinsky EP. Current issues with blood transfusions in sickle cell disease. *Semin Hematol*. 2001;38:14-22.
133. Storry JR, Clausen FB, Castilho L, et al. International Society of Blood Transfusion Working Party on Red Cell Immunogenetics and Blood Group Terminology: Report of the Dubai, Copenhagen and Toronto meetings. *Vox Sang*. 2019;114(1):95-102.
134. Hamilton PB, Farr LE, Hiller A, Van Slyke DD. Preparation of hemoglobin solutions for intravenous infusion. *J Exp Med*. 1947;86(6):455-464.
135. Schwoch G, Passow H. Preparation and properties of human erythrocyte ghosts. *Mol Cell Biochem*. 1973;2(2):197-218.

136. Dodge JT, Mitchell C, Hanahan DJ. The preparation and chemical characteristics of hemoglobin-free ghosts of human erythrocytes. *Arch Biochem Biophys*. 1963;100(1):119-130.
137. Nalbandian RM, Nichols BM, Camp FR, et al. Dithionite tube test--a rapid, inexpensive technique for the detection of hemoglobin S and non-S sickling hemoglobin. *Clin Chem*. 1971;17(10):1028-1032.
138. Thermo Fisher Scientific Diagnostics. *SickleScreen Sickling Hemoglobin Screening Kit: User Manual*.; 2020.
139. Greenburg AG, Kim HW. Hemoglobin-based oxygen carriers. *Crit Care*. 2004;8(2):61-64.
140. Buehler PW, D'Agnillo F, Schaer DJ. Hemoglobin-based oxygen carriers: From mechanisms of toxicity and clearance to rational drug design. *Trends Mol Med*. 2010;16(10):447-457.
141. Clark MR, Shohet SB. Hybrid erythrocytes for membrane studies in sickle cell disease. *Blood*. 1976;47(1):121-131.
142. Hebbel RP. Beyond hemoglobin polymerization: the red blood cell membrane and sickle disease pathophysiology. *Blood*. 1991;77:214-237.
143. Camus SM, De Moraes JA, Bonnin P, et al. Circulating cell membrane microparticles transfer heme to endothelial cells and trigger vasoocclusions in sickle cell disease. *Blood*. 2015;125(24):3805-3814.
144. Hebbel RP, Key NS. Microparticles in sickle cell anaemia: promise and pitfalls. *Br J Haematol*. 2016;174(1):16-29.
145. Muzykantov VR. Drug delivery by red blood cells: vascular carriers designed by Mother Nature. *Expert Opin Drug Deliv*. 2010;7(4):403-427.
146. Hidalgo A, Chang J, Jang JE, Peired AJ, Chiang EY, Frenette PS. Heterotypic interactions enabled by polarized neutrophil microdomains mediate thromboinflammatory injury. *Nat Med*. 2009;15(4):384-391.
147. Manwani D, Frenette PS. Vaso-Occlusion in sickle cell disease: Pathophysiology and novel targeted therapies. *Blood*. 2013;122(24):3892-3898.
148. Bennewitz MF, Jimenez MA, Vats R, et al. Lung vaso-occlusion in sickle cell disease mediated by arteriolar neutrophil-platelet microemboli. *JCI Insight*. 2017;2(1):1-19.
149. Crompton D, Orizondo RA, Kameneva MV. Drag Reducing Polymers Improve Oxygen Transfer Rate in Miniature Hollow Fiber Membrane Oxygenators. *ASAIO J*. 2019;65(Supplement 1):10.

150. Hall JE, Guyton AC. Respiratory Physiology. In: *Guyton and Hall Textbook of Medical Physiology*. 12th ed. Elsevier, Inc; 2010:310-385.
151. Fan E, Gattinoni L, Combes A, et al. Venovenous extracorporeal membrane oxygenation for acute respiratory failure: A clinical review from an international group of experts. *Intensive Care Med*. 2016;42(5):712-724.
152. Lubnow M, Philipp A, Foltan M, et al. Technical complications during veno-venous extracorporeal membrane oxygenation and their relevance predicting a system-exchange - Retrospective analysis of 265 cases. *PLoS One*. 2014;9(12):1-22.
153. Parlar AI, Sayar U, Cevirme D, Yuruk MA, Mataraci I. Successful use of fondaparinux in a patient with heparin-induced thrombocytopenia while on extracorporeal membrane oxygenation after mitral valve redo surgery. *Int J Artif Organs*. 2014;37(4):344-347.
154. Jayaraman G, Seshadri V, Kumar A. The effect of two-phase nature of blood on the gas exchange in capillary membrane oxygenators. *Chem Eng Sci*. 1989;44(10):2398-2402.